

**Nuclear modification of single electrons from
heavy flavor decays in Au-Au collisions at
 $\sqrt{s_{NN}} = 200$ GeV (RHIC Run-2)**

A Dissertation, Presented

by

Jamil Enis Egdemir

to

The Graduate School

in Partial Fulfillment of the

Requirements

for the Degree of

Doctor of Philosophy

in

Physics

Stony Brook University

December 2005

INFORMATION TO USERS

The quality of this reproduction is dependent upon the quality of the copy submitted. Broken or indistinct print, colored or poor quality illustrations and photographs, print bleed-through, substandard margins, and improper alignment can adversely affect reproduction.

In the unlikely event that the author did not send a complete manuscript and there are missing pages, these will be noted. Also, if unauthorized copyright material had to be removed, a note will indicate the deletion.



UMI Microform 3258875

Copyright 2007 by ProQuest Information and Learning Company.
All rights reserved. This microform edition is protected against
unauthorized copying under Title 17, United States Code.

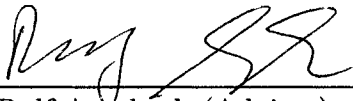
ProQuest Information and Learning Company
300 North Zeeb Road
P.O. Box 1346
Ann Arbor, MI 48106-1346

State University of New York
at Stony Brook

The Graduate School

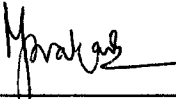
Jamil Enis Egdemir

We, the dissertation committee for the above candidate for the Doctor of Philosophy degree, hereby recommend acceptance of the dissertation.



Ralf Averbeck (Advisor)

Assistant Professor, Department of Physics and Astronomy

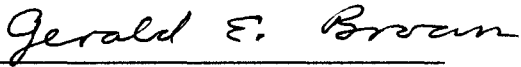


Madappa Prakash (Chair)

Professor, Department of Astronomy and Physics

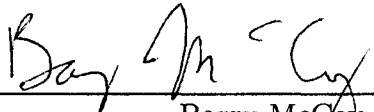


Axel Drees
Professor, Department of Astronomy and Physics



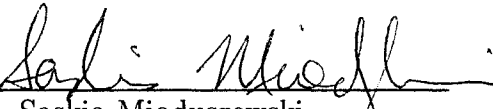
Gerald E. Brown

Professor, Department of Astronomy and Physics



Barry McCoy

Professor, Department of Astronomy and Physics



Saskia Mioduszewski

Scientist, Brookhaven National Laboratory

This dissertation is accepted by the Graduate School.



Graduate School

Abstract of the Dissertation

Nuclear modification of single electrons from heavy flavor decays in Au-Au collisions at $\sqrt{s_{NN}} = 200 \text{ GeV}$ (RHIC Run-2)

by

Jamil Enis Egdemir

Doctor of Philosophy

in

Physics

Stony Brook University

2005

This thesis summarizes the analysis of non-photonic single electrons from Au-Au collisions at $\sqrt{s_{NN}} = 200 \text{ GeV}$ (RHIC Run-2). From the fully corrected inclusive electron spectra in various Au-Au centrality classes, we subtract background cocktails of electrons, from photonic sources. The remaining non-photonic electrons originate from heavy flavor decays. With the corresponding measurement from p + p collisions at 200 GeV as reference, we calculate the nuclear modification factor R_{AA} as function of p_T in various Au + Au centrality classes. A significant suppression of non-photonic electrons is observed in central collisions at high p_T .

Very likely, this indicates energy loss to a nuclear medium.

Acknowledgements

To my friends Yusuf K., Mattt, Mattc, Evan, Lisa B., Christian, Poco, Fumi, Babak, Raffe, Torsten, Jason, Sean, Prakash, Gerry, Socoro, Laura, and finally Ralf,

Nothing lasts forever. I wish I could change that. The time we have all spent together has become a part of me that I hold dear, but it was too short. That makes me sad. And it is because of this that I write these acknowledgements. This is the only way that I know of that will keep us together for just a bit longer.

If nothing else, I want this thesis to be a memorial to who we were.

Contents

List of Figures	xxvi
Acknowledgements	xxvii
1 Preface	1
2 Leading up to RHIC	4
2.1 Developing the Framework of Relativistic Heavy-Ion Physics	4
2.1.1 Why We Need Machines	5
2.1.2 Recognizing the Quantities Of Interest	9
2.1.3 Big-Bang Nucleosynthesis	10
2.1.4 Two Categories of Heavy-Ion Research	12
2.2 Charm Quark Production in pQCD	12
2.2.1 Energy Loss Mechanisms	16
2.3 Known Experimental Results for Possible Medium Effects	20
2.3.1 p_T Spectra By Species	21
2.3.2 Current Status	23
2.3.3 Theoretical Models	24
2.4 Why do we care about charm?	25

2.4.1	Large Charm Mass	25
2.4.2	Yield As Baseline For J/Ψ Measurement	26
2.5	How RHIC and PHENIX fit in Heavy-Ion Physics	27
2.5.1	Summary	29
3	RHIC and the PHENIX Experiment	32
3.1	RHIC	36
3.2	PHENIX	39
3.2.1	Triggering With the BBC and ZDC	39
3.2.2	Tracking	49
3.2.3	Particle Identification (PID)	55
3.3	Track-Matching	59
4	The Nature of the Nuclear Modification Factor: R_{AA}	61
4.0.1	Glauber Model of Nuclear Collisions	62
5	The Measurement	66
5.1	Preliminaries	66
5.1.1	A Rough Outline of Procedure	66
5.1.2	Conventions	68
5.1.3	Location of Analysis Code	69
5.2	Data Set	69
5.2.1	Run Selection	71
5.2.2	Centrality	75
5.3	Electron Identification	75
5.3.1	Cut Variables	75

5.3.2	Specification of Identification Cuts	78
5.4	Raw Inclusive Spectra	79
5.5	Random hadronic background subtraction	81
5.5.1	Swapped Variables	82
5.6	Acceptance and Monte-Carlo/Data Comparison	87
5.6.1	Fiducial Cuts	87
5.6.2	Acceptance Distributions	88
5.6.3	Comparison of Electron ID Variables In Data And Simulation	92
5.7	Corrections	93
5.7.1	General Description	93
5.7.2	Normalization of the EE Rungroup	100
5.7.3	Embedding Correction	101
5.8	Systematic Uncertainties	101
5.8.1	Internal Systematics	103
5.8.2	Cocktail Systematics	107
5.8.3	$p + p$ Reference	108
5.8.4	T_{ab}	108
5.8.5	Summary	108
5.9	Fully-corrected Inclusive Electron p_T Spectra	109
5.10	Electron Cocktail Calculations	110
5.11	Details of the Cocktail	114
5.11.1	Overview	116
5.11.2	Neutral pions	117
5.11.3	Other light mesons	128

5.11.4	Electrons from photon conversions	130
5.11.5	Weak kaon decays: K_{e3}	134
5.11.6	Direct radiation	135
5.11.7	Electron cocktail	140
5.11.8	Systematic error estimate	145
5.11.9	Comparison with the converter measurement	148
5.12	p_T Spectra Of Electrons From Non-Photonic Sources	150
5.12.1	Bin Shift Correction	157
5.12.2	Binary Scaling Of Non-Photonic Electron Yields	158
5.13	Non-Photonic Electron R_{AA}	159
5.14	Integrated R_{AA}	163
5.14.1	Definition of Integrated R_{AA}	163
5.14.2	Treatment of Uncertainties	163
5.14.3	Results	165
6	Comparison to Theory and Conclusions	168
6.1	Central Collisions	168
6.2	Considerations	170
6.2.1	The Theoretical Point Of View	170
6.2.2	Combined Effects & Range of Validity	174
6.2.3	Choosing Heavy Over Light Quarks	177
6.3	General Approach – Arnesto et. al.	178
6.3.1	Method	178
6.3.2	Assumptions	178
6.3.3	Interpretation	180

6.4	General Approach – Djordjevic et. al.	182
6.4.1	Method	182
6.4.2	Interpretations	183
7	Outlook	185
7.1	Preliminary Data for the Cocktail	185
7.2	Final Assesment	187
	Bibliography	194
A	Data Tables for Graphs	195
B	Parametrizations	212
B.1	depemc	212
C	Index	214

List of Figures

2.1	The coupled BEVATRON and SuperHILAC acceleration complex known together as BEVALAC. Located at Berkeley (1984) where the first notions of heavy ion physics were laid down. . .	5
2.2	Possible interior structure of a neutron star showing the different layers in the different phases. Theoretical considerations of the stars structure drove physicists towards the idea of quark-matter setting the stage for quark-gluon plasmas. Taken from the Neutron Star Theory Group at UNAM [46].	7
2.3	An early QCD phase diagram in the temperature (T) - baryon chemical potential (μ) plane. The two points labeled E and M, are the critical endpoints of two . One of the points is labeled M, representing multi-fragmentation, and corresponds to the liquid-gas transition in nuclear matter. CSC stands for color super-conducting in both CSC2 and CSC3 [55].	8
2.4	Sequence of images showing the collision of two heavy-ions, the creation of a fireball, and the resulting hadrons formed in the freezeout. Taken from the RHIC homepage [44].	10

2.5	A timeline of how the universe is thought to have evolved as it cooled following the Big Bang. Taken from the RHIC website [45].	11
2.6	Multiplicity of electrons as a function of N_{coll} from Au + Au collisions together with the p + p result. The data exhibits the binary scaling of charm production.	13
2.7	Feynman diagrams of first, second, and third order charm production. a) and b) are the largest leading order contributions. The rest of the diagrams amount to [13].	14
2.8	Ratio of gluon emission spectra off charm and light quarks for quark momenta $p_T = 10$ GeV (solid line) and $p_T = 100$ GeV (dashed) in hot QCD matter ($\hat{q} = .2$ GeV ³ , L=5 fm); $x = \frac{\omega}{p_T}$ taken from [19].	18
2.9	Statistical models are used to predict ratios of particle yields. [58]	25
2.10	Charged particle yields per unit pseudo-rapidity as function of center-of-mass energy per nucleon in heavy-ion collisions. This plot is useful for understanding where RHIC fits in to the field as an accelerator. It is also worth noting how surprising it is that the production mechanisms seem to be similar over so many orders of magnitude [57].	28
2.11	QCD phase diagram showing the hadronic phase (H), the quark-gluon plasma (QCP), the color super-conducting phase (CSC), the end-point of the first-order line (E), and the end of the nuclear liquid-gas line [multi-fragmentation] (M) [54].	30

3.1	Schematic of RHIC and the supporting machines located at Brookhaven National Laboratory in Upton, NY. [47]	37
3.2	Technical parameters and specifications of RHIC [48].	38
3.3	Schematic of the PHENIX detector and status of each subsystem as of Run II (2001). Upper panel: all subsystems active. Lower panel: Muon identification subsystem was the only subsystem not active. (Electronic version: active detector subsystems are shown in red.)	40
3.4	Schematic of the PHENIX detector showing the location of the Beam-Beam Counter (BBC) and the Zero-Degree Calorimeter (ZDC). This is taken from a PHENIX Focus presentation given by Dave Morrison of the PHENIX collaboration given during Run V.	41
3.5	Using the Beam-Beam Counter to determine the starting time and the z-vertex of an interaction. Taken from Tomoaki Nakamura's PHENIX Focus presentation given during Run IV to the new students of the collaboration.	42
3.6	The trajectories of various particles (charged and neutral) that enter and leave the IR. [50]	44
3.7	Mechanical design of the RHIC ZDCs [50].	46
3.8	The anatomy of a collision in the participant-spectator model. (shown at "PHENIX Focus 2005 - How to Measure Centrality." by David Morrison, PHENIX collaboration, 2005-07-01)	47

3.9 ZDC response vs. BBC response. Along the vertical axis is the energy deposition of neutrons normalized to the maximum value. The horizontal axis show the same for charge deposition in the BBC. This illustrates the “centbyclock” method of centrality determination. Each slice determines a range in percentages of centrality. (shown at “QM 2002.” by Tatsuya Chujo, PHENIX collaboration, 2005-07-01)”	48
3.10 Number of participants, spectators, and binary collisions as a function of impact parameter. (shown at “CTEQ 2002” by Jamie Nagle, PHENIX collaboration, 2005-07-01) Au + Au at 200 GeV per nucleon.	50
3.11 The PHENIX Drift Chamber frame construction [49].	52
3.12 The PHENIX Drift Chamber wire layers and configuration [49].	54
3.13 The PHENIX pad chambers. Taken from Sasha Milov’s PHENIX Focus talk given on 01/04/05 “How to Measure Multiplicity and Transverse Energy?”	55
3.14 The RICH subsystem from [51].	56
3.15 photo of two sectors of the EMC during the early stages of installation taken by Yuji Goto on 9/17/98.	58
3.16 Diagram of the track-matching procedure used in this analysis for particle identification. Reconstructed tracks point to a location on the EMC. This location is then compared to the location of a shower and the small deviations are used as the basis for an analysis cut [52].	60

4.1	Definitions of the thickness functions and nuclear overlap used as a basis for the Glauber model. (shown at “PHENIX Focus 2005 - How to Measure Centrality.” by David Morrison, PHENIX collaboration, 2005-07-01)	63
5.1	Tracks per event for Minimum Bias collisions. The points within the ellipse are the Quark Matter (QM) rungroup. Everything outside the ellipse is the Everything Else (EE) rungroup.	73
5.2	Gaussian fit to projection of tracks per event for minimum bias in the EE rungroup.	74
5.3	Distributions of centrality(centclock) for the two chosen rungroups (see below).	76
5.4	Overlay of uncorrected inclusive electrons for Minimum bias. .	79
5.5	Ratio of uncorrected inclusive electron p_T spectra from the QM and EE rungroup for Minimum bias. The thick black line shows the fit to a constant function.	81
5.6	E/p distributions for Run II p+p collisions plotted to show the relationship between the hadronic background and swapped distributions used eliminate random associations of tracks with rings in the RICH [13].	84
5.7	Overlays of energy over momentum as function of $\frac{E}{p}$ shown in two p_T -classes for minimum bias. The two panels correspond to different windows of p_T of 0.5 GeV width. The upper right panel is .5 - 1.0 GeV and the lower left is 1.5 - 2.0 GeV	86
5.8	α vs. ϕ distributions for data (left) and MC (right).	89

5.9	Ratio of α vs. ϕ distributions shown in 5.8.	90
5.10	α vs. ϕ distributions for data (left) and MC (right) in the north detector.	90
5.11	Ratio of α vs. ϕ distributions shown in 5.10.	91
5.12	α vs. ϕ distributions for data (left) and MC (right) in the south detector.	91
5.13	Ratio of α vs. ϕ distributions shown in 5.12.	92
5.14	Overlays of sigmalized energy over momentum variable as function of p_T for data and simulation in p_T classes.	93
5.15	Overlays of sigmalized phi variable as function of p_T for data and simulation in p_T classes.	94
5.16	Overlays of sigmalized dz variable as function of p_T for data and simulation in p_T classes.	94
5.17	mean of gaussian fits to sigmalized energy over momentum variable as function of p_T	95
5.18	mean of gaussian fits to sigmalized phi variable as function of p_T	95
5.19	mean of gaussian fits to sigmalized dz variable as function of p_T .	96
5.20	sigma of gaussian fits to sigmalized energy over momentum variable as function of p_T	96
5.21	sigma of gaussian fits to sigmalized phi variable as function of p_T	97
5.22	sigma of gaussian fits to sigmalized dz variable as function of p_T .	97

5.23 Corrections for acceptance and reconstruction efficiency are shown as function of p_T . Both the first and the second iterations are shown. The latter is applied track-by-track in the analysis.	99
5.24 Systematic error associated with the track matching.	104
5.25 Systematic error associated with the n0 cut.	105
5.26 Systematic error associated with the n3 cut.	105
5.27 Relative error obtained by a variation of the chi2 track variable from which a systematic error is obtained.	106
5.28 Systematic error associated with the disp cut.	106
5.29 Systematic error associated with the signalized e/p cut.	107
5.30 Overlay of inclusive electrons and coctail for 0 - 10 % centrality class. Error bars (brackets) are statistical (systematic) errors.	110
5.31 Overlay of inclusive electrons and coctail for 10 - 20 % centrality class. Error bars (brackets) are statistical (systematic) errors.	111
5.32 Overlay of inclusive electrons and coctail for 20 - 40 % centrality class. Error bars (brackets) are statistical (systematic) errors.	111
5.33 Overlay of inclusive electrons and coctail for 40 - 60 % centrality class. Error bars (brackets) are statistical (systematic) errors.	112
5.34 Overlay of inclusive electrons and coctail for 60 - 80 % centrality class. Error bars (brackets) are statistical (systematic) errors.	112
5.35 Overlay of inclusive electrons and coctail for 60 - 92 % centrality class. Error bars (brackets) are statistical (systematic) errors.	113
5.36 Overlay of inclusive electrons and coctail for Minimum Bias. Error bars (brackets) are statistical (systematic) errors.	113

5.37 The upper panel shows the minimum bias cocktail overlayed with the minimum bias inclusive electron spectrum. Each component is shown as well. The breakdown by contribution is laid out in the legend. The lower panel shows the relative contribution of each component in the cocktail.	115
5.38 Fit of the combined charged (blue symbols at low p_T) and neutral pion spectra (red symbols at high p_T) according to Eq. 5.6 in minimum bias collisions (left panel) and ratio of data and fit (right panel). Error bars are statistical uncertainties only. . . .	118
5.39 Fits of the combined charged (blue symbols at low p_T) and neutral pion spectra (red symbols at high p_T) according to Eq. 5.6 in 0-10 % (upper panels), 10-20 % (middle panels), and 20-40 % (lower panels) central collisions are shown on the left. The corresponding ratio of data and fits are shown on the right. Error bars are statistical uncertainties only.	119
5.40 Fits of the combined charged (blue symbols at low p_T) and neutral pion spectra (red symbols at high p_T) according to Eq. 5.6 in 40-60 % (upper panels), 60-80 % (middle panels), and 60-92 % (lower panels) central collisions are shown on the left. The corresponding ratio of data and fits are shown on the right. Error bars are statistical uncertainties only.	120

- 5.41 Fit of the combined charged (blue symbols at low p_T) and neutral pion spectra (red symbols at high p_T) according to Eq. 5.6 in minimum bias collisions (left panel) and ratio of data and fit (right panel). All data points have been moved up by their individual systematic uncertainty to estimate a 1σ upper limit for the pion input. Error bars are statistical uncertainties only. 122
- 5.42 Fits of the combined charged (blue symbols at low p_T) and neutral pion spectra (red symbols at high p_T) according to Eq. 5.6 in 0-10 % (upper panels), 10-20 % (middle panels), and 20-40 % (lower panels) central collisions are shown on the left. All data points have been moved up by their individual systematic uncertainty to estimate a 1σ upper limit for the pion input. The corresponding ratio of data and fits are shown on the right. Error bars are statistical uncertainties only. 123
- 5.43 Fits of the combined charged (blue symbols at low p_T) and neutral pion spectra (red symbols at high p_T) according to Eq. 5.6 in 40-60 % (upper panels), 60-80 % (middle panels), and 60-92 % (lower panels) central collisions are shown on the left. All data points have been moved up by their individual systematic uncertainty to estimate a 1σ upper limit for the pion input. The corresponding ratio of data and fits are shown on the right. Error bars are statistical uncertainties only. 124

5.44 Fit of the combined charged (blue symbols at low p_T) and neutral pion spectra (red symbols at high p_T) according to Eq. 5.6 in minimum bias collisions (left panel) and ratio of data and fit (right panel). All data points have been moved down by their individual systematic uncertainty to estimate a 1σ lower limit for the pion input. Error bars are statistical uncertainties only.	125
5.45 Fits of the combined charged (blue symbols at low p_T) and neutral pion spectra (red symbols at high p_T) according to Eq. 5.6 in 0-10 % (upper panels), 10-20 % (middle panels), and 20-40 % (lower panels) central collisions are shown on the left. All data points have been moved down by their individual systematic uncertainty to estimate a 1σ lower limit for the pion input. The corresponding ratio of data and fits are shown on the right. Error bars are statistical uncertainties only.	126
5.46 Fits of the combined charged (blue symbols at low p_T) and neutral pion spectra (red symbols at high p_T) according to Eq. 5.6 in 40-60 % (upper panels), 60-80 % (middle panels), and 60-92 % (lower panels) central collisions are shown on the left. All data points have been moved down by their individual systematic uncertainty to estimate a 1σ lower limit for the pion input. The corresponding ratio of data and fits are shown on the right. Error bars are statistical uncertainties only.	127
5.47 Ratio of π^0 and the average of π^+ and π^- from a minimum bias PYTHIA calculation of 200 GeV p+p collisions [65].	128

5.48 η meson invariant cross section (data points) compared with an m_T scaled modified Hagedorn parameterization of the corresponding pion spectra for $p + p$ collisions at 200 GeV (left panel, from [69]). The error bars are statistical only. In the ratio of data to parameterization (right panel), the error bars are the quadratic sum of statistical and systematic uncertainties.	130
5.49 Ratio of reconstructed electrons from photon conversions and from Dalitz decays as function of electron p_T for five π^0 simulations using various lower limits on the $\pi^0 p_T$. The lines indicate the ratio that is finally adopted for the current cocktail, <i>i.e.</i> 1.25 ± 0.10 .	132
5.50 Invariant multiplicity distributions of electrons and positrons from K_{e3} decays in various Run-2 Au + Au centrality classes (taken from [62]). The error bars are purely statistical. The lines correspond to fits according to Eq. 5.9.	136
5.51 Fit to a NLO direct photon calculation [75] with the modified Hagedorn parameterization from Eq. 5.10 (left panel) and ratio of NLO <i>i.e. data to the fit</i> (right panel).	138
5.52 Invariant direct photon spectrum from the current $p + p$ cocktail together with the fit (red line) to the NLO input (left panel) and ratio of data to fit (right panel).	139
5.53 Invariant yield of electrons from all implemented sources for minimum bias Au + Au collisions at 200 GeV (Run-2).	141

5.54 Invariant yield of electrons from all implemented sources for 0-10 % central (upper panel) and 10-20 % central (lower panel) Au + Au collisions at 200 GeV (Run-2).	142
5.55 Invariant yield of electrons from all implemented sources for 20-40 % central (upper panel) and 40-60 % central (lower panel) Au + Au collisions at 200 GeV (Run-2).	143
5.56 Invariant yield of electrons from all implemented sources for 60-80 % central (upper panel) and 60-92 % central (lower panel) Au + Au collisions at 200 GeV (Run-2).	144
5.57 Systematic error of the full cocktail due to the uncertainty in the pion input for minimum bias Au + Au collisions at 200 GeV (Run-2). Statistical fluctuation will be smoothed by a fit in the end.	145
5.58 Systematic error of the full cocktail due to the uncertainty associated with the decays of other light mesons for minimum bias Au + Au collisions at 200 GeV (Run-2). From top to bottom, the curves correspond to contributions from decays os η (red), ω (blue), ϕ (magenta), and ρ mesons (green).	146
5.59 Systematic error of the full cocktail due to the uncertainty associated with the contributions from photon conversions (light blue curve at $\approx 4\%$), from K_{e3} decays (green curve approaching zero towards high p_T), and from direct radiation (dark blue curve diverging towards high p_T) for minimum bias Au + Au collisions at 200 GeV (Run-2).	146

5.60 Total systematic error of the full cocktail for minimum bias Au + Au collisions at 200 GeV (Run-2) together with a parabola fit.	147
5.61 Ratios of measured electron spectra from photonic sources (from Ref. [62]) and the photonic part of the current cocktail as function of p_T for all available centrality classes. All ratios are fit with a constant for $p_T < 2$ GeV/c.	149
5.62 Overlay of Non-Photonic spectra from converter and the cocktail analysis for 00 - 10 % in centrality. Also shown is a fit resulting from fitting to the combination of both spectra according to Eq. 5.13.	151
5.63 Overlay of Non-Photonic spectra from converter and the cocktail analysis for 10 - 20 % in centrality. Also shown is a fit resulting from fitting to the combination of both spectra according to Eq. 5.13.	152
5.64 Overlay of Non-Photonic spectra from converter and the cocktail analysis for 20 - 40 % in centrality. Also shown is a fit resulting from fitting to the combination of both spectra according to Eq. 5.13.	152
5.65 Overlay of Non-Photonic spectra from converter and the cocktail analysis for 40 - 60 % in centrality. Also shown is a fit resulting from fitting to the combination of both spectra according to Eq. 5.13.	153

5.66 Overlay of Non-Photonic spectra from converter and the cocktail analysis for 60 - 80 % in centrality. Also shown is a fit resulting from fitting to the combination of both spectra according to Eq. 5.13.	153
5.67 Overlay of Non-Photonic spectra from converter and the cocktail analysis for minimum bias. Also shown is a fit resulting from fitting to the combination of both spectra.	154
5.68 Ratio of Non-Photonic spectra to the merged fit P_T spectra for 0-10% centrality overlayed with the same spectrum from converter. The fit results from fitting to the combination of both spectra according to Eq. 5.13.	154
5.69 Ratio of Non-Photonic spectra to the merged fit P_T spectra for 10-20% centrality overlayed with the same spectrum from converter. The fit results from fitting to the combination of both spectra according to Eq. 5.13.	155
5.70 Ratio of Non-Photonic spectra to the merged fit P_T spectra for 20-40% centrality overlayed with the same spectrum from converter. The fit results from fitting to the combination of both spectra according to Eq. 5.13.	155
5.71 Ratio of Non-Photonic spectra to the merged fit P_T spectra for 40-60% centrality overlayed with the same spectrum from converter. The fit results from fitting to the combination of both spectra according to Eq. 5.13.	156

5.72 Ratio of Non-Photonic spectra to the merged fit P_T spectra for 60-80% centrality overlayed with the same spectrum from converter. The fit results from fitting to the combination of both spectra according to Eq. 5.13.	156
5.73 Ratio of Non-Photonic spectra to the merged fit P_T spectra for Minimum Bias overlayed with the same spectrum from converter. The fit results from fitting to the combination of both spectra according to Eq. 5.13.	157
5.74 Integrals of the p_T spectra from each centrality, divided by N_{bin} as a function of N_{bin} from the present analysis and from [68]. . .	159
5.75 Reference spectrum of electrons from p + p collisions taken from [14]. Also shown are the predicted contributions from charm and beauty.	160
5.76 R_{AA} by Centrality for non-photonic electrons. Supression is clearly seen at high p_T where the data falls below unity, indicating the presence of a medium. Systematic errors are large at low p_T so we can not make any statement there about a possible nuclear modification.	162
5.77 Integrated R_{AA} as function of N_{part} for three values of p_T^{low} : 2.0 GeV/c (upper panel), 2.5 GeV/c (middle panel), and 3.0 GeV/c (lower panel). Error bars are statistical only, brackets are point-by-point systematics, and boxes are centrality independent systematics. For (unfair) comparison (see text), we overlay $R_{AA}^{2.5-5.0}$ of neutral pions (from [17]).	167

6.1	Theoretical predictions for R_{AA} overlaid with the data of this thesis for the 10% most central collisions.	169
7.1	Non-photonic electron R_{AA} , by centrality class created using the Run IV Au + Au spectrum and a scaled Run III p + p spectrum.	186
7.2	Non-photonic electron R_{AA} , by centrality class released by the STAR collaboration shown at Quark Matter '05 in Budapest.	188

Chapter 1

Preface

Measurements in physics are almost always built up on the principles that have been established previously. Experiments and results inspire more experiments and results. This is natural and the results contained here are no exception. I feel that I need to stress this because this thesis is not self-contained by any means.

With that said, I hope to address three different groups of people who I believe will eventually read this work:

The first group are those of you who know me, are non-scientific, and are looking here out of curiosity. Or perhaps because I tricked you somehow into reading this. If you are in this group, you don't have a 4 year degree in a hard science. Or at least, you don't have a physics background in the usual sense. Perhaps you are a family member or a friend who is just interested in what I did for my doctorate and why physicists think it's worth it to spend US tax dollars on it. If this is you, read Chapter 1 and call it a day. And remember that this thing is important because physics research at its center, is an attempt to understand the fundamentals of reality. It's not about the

applications or devices that may come from what is learned. It's about the understanding itself.

And if you insist on asking what it's good for – I'm not sure. No one is. You must keep in mind that when the electron was discovered a hundred years ago, we didn't have lights, stereos, refrigerators, cars, computers, planes, and everything else that ever was or ever will be plugged into a wall socket. The convenience of our modern age is a direct result of our knowledge of how electrons talk to each other and the resulting electricity. Electrons are particles. They talk and influence each other in a certain way that we understand very well now. The quarks and gluons inside protons and neutrons talk to each other too in a very similar way. This thesis is an attempt to add a little bit to the understanding of how they talk, just like the electrons... If the electrons and electricity are any indication of what's to come, there are going to be some exciting changes in the world that are just ahead. That's what this thesis is good for.

The second group of readers are those who are students starting off in High-Energy Nuclear Physics, RHIC style. If this is you, I have tried to give pointers and references to places where the best explanations have been given (that I know of...) for any particular topic that has come up here. You will find, as you are trying to find direction in your own work, it's really helpful if you can get your hands on a document that can steer you in the right direction. The biggest trouble I had as a grad student when I started was trying to put together the bigger picture. It's too easy to get lost in the details and the day to day set of tasks that make up the larger efforts of an experimental group. Faced with your present work, I hope that I can help fit this and other single-

electron analyses into the conceptual framework that you are no doubt trying to build up right now... For you, Ch 1 is good to know but will seem fluffy at first, Ch 2 is more for you. If you are actually starting up a single-electron analysis and you need more, then you will find what you need in Ch 3.

The last group is made up of you who are professional physicists. You are an established RHIC physicist, probably on PHENIX, STAR, or perhaps you are a theorist. If this is you, turn to the back, get your data (everything has been put into tables for you), and think kindly of me. Also, this thesis is a small part of a larger collection of work that it is constantly changing. That being the case, I have tried to maximize my use of references and minimize the repetition of work that is easily found elsewhere in the published PHENIX papers.

As it turns out, RHIC and I started off at the same time in the early 70's. Somehow it seems fitting that we got together in the end.

Chapter 2

Leading up to RHIC

¹

In this chapter, I will attempt to give a short outline of what lead up to this measurement. You may consider this my best effort to help provide an understanding of how this thesis fits in with the rest of the Heavy-Ion world.

2.1 Developing the Framework of Relativistic Heavy-Ion Physics

Nuclear physics has been around for quite a while now. I will avoid going into a long history or timeline of the subject. That has been done many times before. Instead, I will just jump in where the foundations of Heavy-Ions were laid down.

¹For more information on the RHIC accelerator complex, the RHIC website, located at <http://www.bnl.gov/RHIC/> is a good place to start.

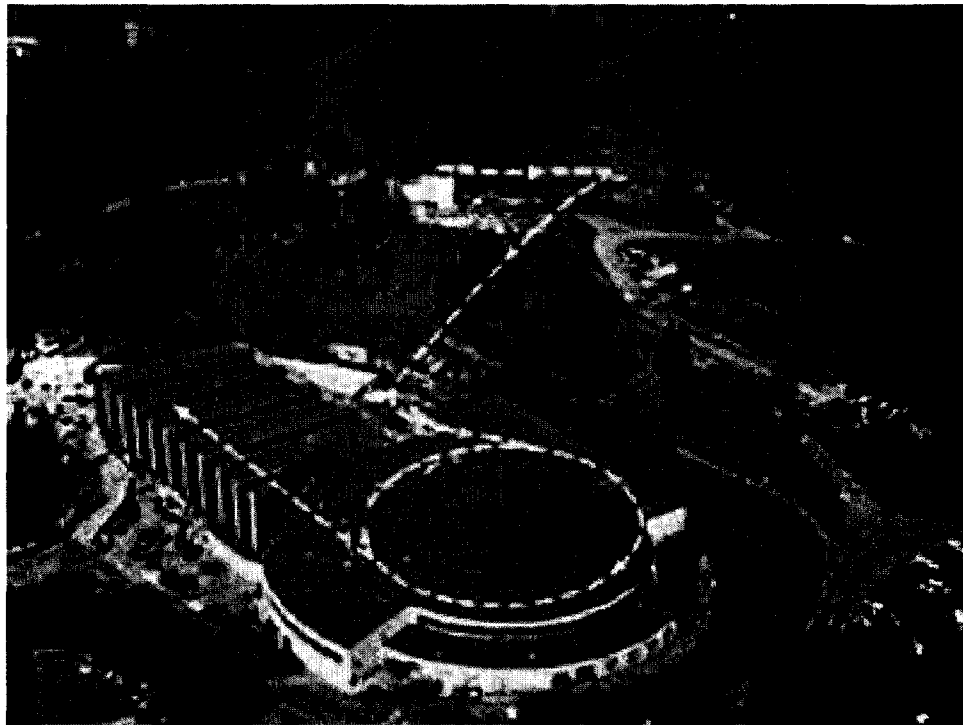


Figure 2.1: The coupled BEVATRON and SuperHILAC acceleration complex known together as BEVALAC. Located at Berkeley (1984) where the first notions of heavy ion physics were laid down.

2.1.1 Why We Need Machines

The BEVALAC BEVALAC (Fig. 2.1) was really the first place where the heavy-ion program was laid out. This first group of physicists working with the BEVELAC had the following goals:

1. Understand the QCD Equation of State
2. Understand the QCD phase diagram
3. Understand the nature of the QCD vacuum

At the time, ideas such as quark-gluon plasma hadn't taken hold yet. The big ticket item in QCD physics was renormalization. There weren't all that many measurements yet and things were mostly on paper. In the midst of everything, astrophysics was providing the driving force. Various questions about the structure of neutron stars led the astrophysicists to postulate a core made of quark matter. It seems that the concept of quark-gluon plasma (QGP) was conceived where nuclear and astrophysics meet.

Drawings like the one shown in Fig. 2.2 were put forward by the astrophysicists of the time. While the original diagrams were a little more simplistic, the central idea hasn't changed much since then even though the fine points have. There is evidence which suggests that the core within a neutron star consists of quark-matter [56].

In quark-matter, the baryon-density has increased so much that a occurred resulting in the liberation of the quarks within the baryons. We don't know yet if this really happens but measurements are improving and sooner or later we will be able to tell the difference between a neutron star and one of these "“, so stay tuned.

Fig. 2.3 shows an early from [55]. You can consider this the state of theoretical affairs as of 1999.

There are four main regions labeled Hadronic, QGP, CSC2, and CSC3. The region labeled hadronic matter is most familiar to us. The realm of normal nuclear matter is contained within. Here we are safe in treating the basic degrees of freedom as hadrons when analyzing the system. The regions labeled CSC are thought to be color super-conducting phases. It has not been experimentally possible to probe these regions yet, but we believe this area of

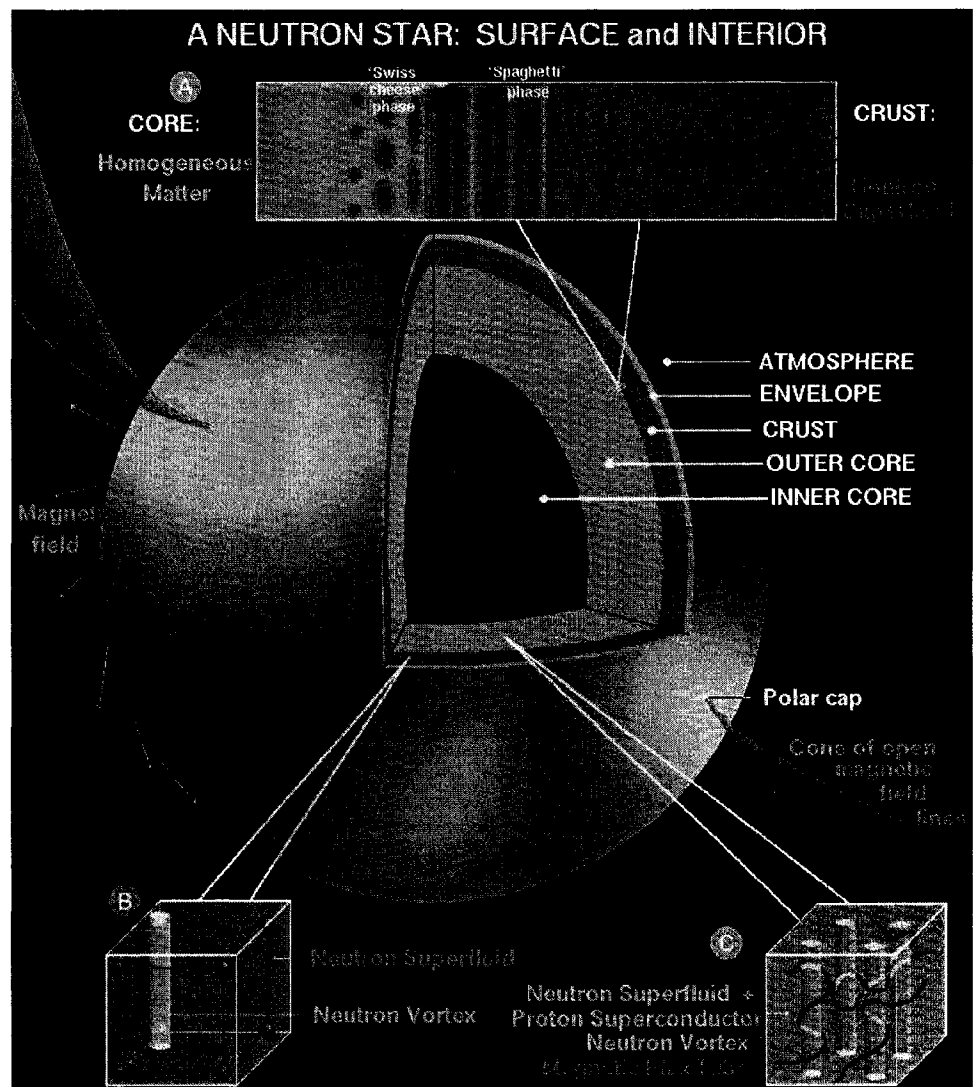


Figure 2.2: Possible interior structure of a neutron star showing the different layers in the different phases. Theoretical considerations of the stars structure drove physicists towards the idea of quark-matter setting the stage for quark-gluon plasmas. Taken from the Neutron Star Theory Group at UNAM [46].

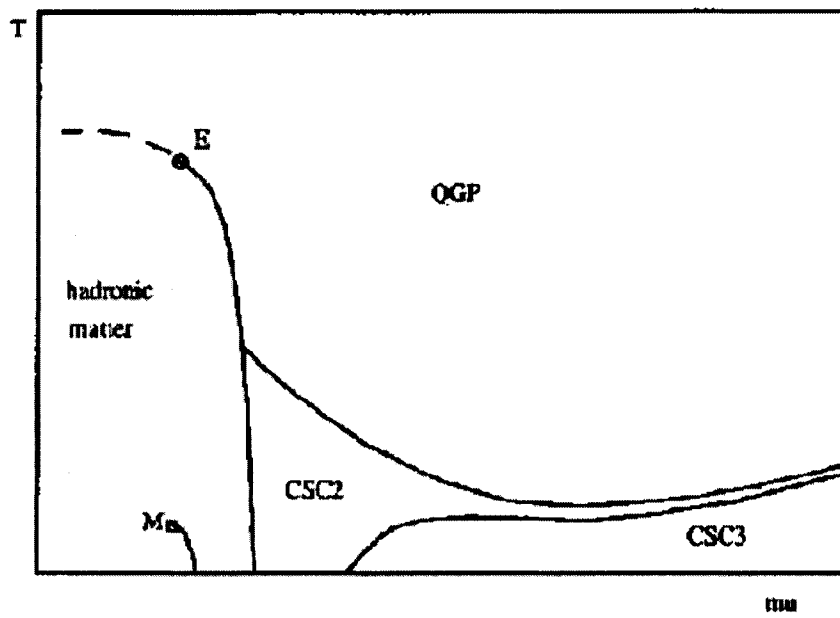


Figure 2.3: An early QCD phase diagram in the temperature (T) - baryon chemical potential (μ) plane. The two points labeled E and M , are the critical endpoints of two . One of the points is labeled M , representing multi-fragmentation, and corresponds to the liquid-gas transition in nuclear matter. CSC stands for color super-conducting in both CSC2 and CSC3 [55].

the diagram is describing matter that may be found in . Of course, the region labeled QGP is our .

It was, and still is the main theoretical goal of all Heavy-Ion programs to reproduce and map out the bulk properties of hot and energy-dense matter. Diagrams such as 2.3 constitute such maps and so we commonly use them as our guides to understanding the phase structure of QCD.

As experimental physicists, we construct colliders and detectors to investigate physical systems that will probe the different regions laid out on this diagram. We will need to know where the experimental systems we are studying fall, on diagrams of this type and so, I provide this early diagram as contrast to a later version of the same published in 2005 that follows at the end of this section. After these discussions (I hope!) we can get an idea of the progress that has been made in the years since the Heavy-Ion field started.

2.1.2 Recognizing the Quantities Of Interest

The concept of a QGP is clear but how to investigate such a thing is not at all so. It was not easy to see how to go about laying out a model or what the important parameters of that model would be. The first steps were to view the collisions of heavy nuclei as a fireball. The essence of the idea would be a modification of the model proposed by Hagedorn [2]. The nuclei would hit with large center of mass energies, melt into a phase where everything (or at least the quarks and gluons) was deconfined, and create the fireball. Hadronization² would follow and the resulting particles would be detected. The sequence is

²The process of forming hadrons from quarks and gluons.

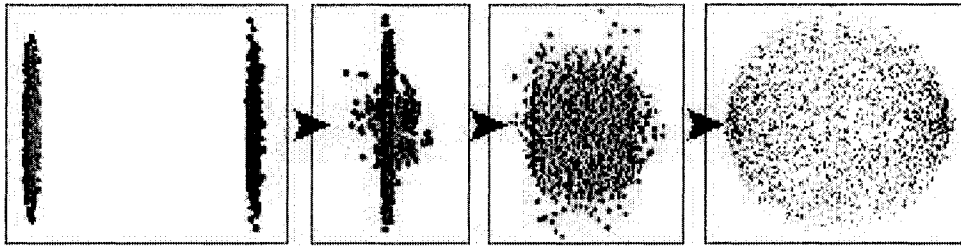


Figure 2.4: Sequence of images showing the collision of two heavy-ions, the creation of a fireball, and the resulting hadrons formed in the freezeout. Taken from the RHIC homepage [44].

shown in Fig. 2.4 from start to finish.³

Not every nucleon⁴ would participate in each collision giving rise to the spectator⁵ and participant⁶ terminology and the beginnings of our notions of centrality. At the time centrality was merely considered a generalization of impact parameter and in a vague sort of way it is – but today we know it to be a difficult thing to precisely define and measure. Centrality is not at all like the impact parameter.⁷

2.1.3 Big-Bang Nucleosynthesis

Today we hear all the time about how the collisions at RHIC are recreating a state of matter that previously only existed in the very first moments of the universe. Fig. 2.5 shows a timeline of how we think the universe cooled. Starting from the top we proceed from left to right and top to bottom cooling all

³There are also some very nice movies and animations of collisions available for downloading on the RHIC website at http://www.bnl.gov/RHIC/heavy_ion.htm. They are in an mpeg format and can be viewed in any of the usual players available for Linux or Windows.

⁴Here we treat protons and neutrons as the same particle but with different isospin.

⁵nucleons that are not actively involved in the collisions.

⁶those nucleons that are.

⁷Though you will not do so badly if you ignore the distinction.

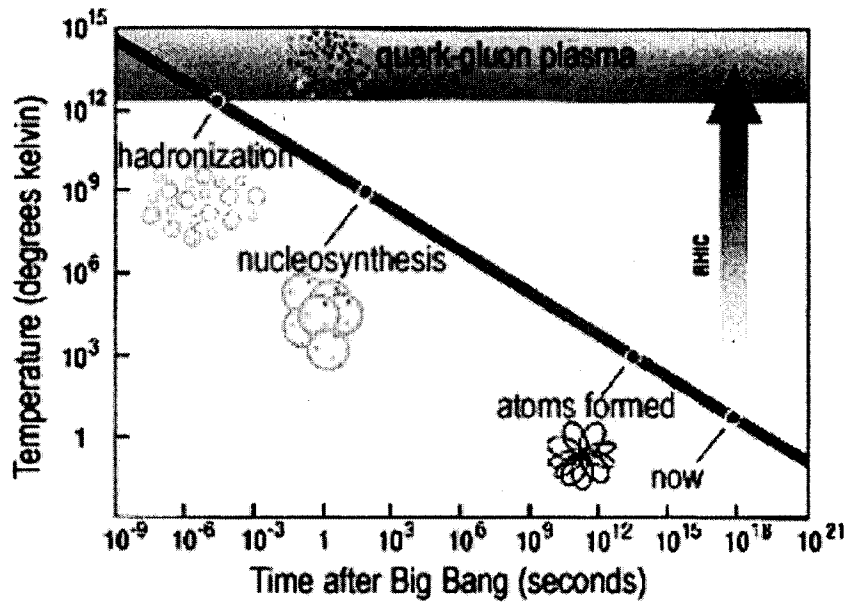


Figure 2.5: A timeline of how the universe is thought to have evolved as it cooled following the Big Bang. Taken from the RHIC website [45].

the way.

Big-Bang Nucleosynthesis is an analogy, inspired by the expansion and cooling that leads to a freeze-out [1]. It is a good analogy that connects the very large scale to the very small. It also leads to interesting lines of thought. For a freeze-out, what would be the where the transition occurs? There are many different types of hadrons to consider and each may have its own critical temperature.

The great power of the analogy to the big bang is the realization that a thermodynamic canonical or statistical analysis is appropriate. This was the first successful attempt at a theoretical analysis of the at the beginning of the hadron phase. We hope that the freeze-out preserves that piece of information.

2.1.4 Two Categories of Heavy-Ion Research

The research in the field can be roughly separated into two categories of probes; hard and soft. Each gives us different types of information corresponding to different times in the collisions of heavy nuclei. The hard probes are those that give us information about initial state effects taking place, early on in the collision, while the soft ones are for understanding the later stage, or of the collision.

Experiments in the soft category are measurements of quantities that have information reflecting the evolution of the fireball from start to finish. A good example would be the measurement of any elliptical flow present in the nuclear medium. Presently we call this a measurement of V_2 [6]. Soft probes are not the subject of this thesis so I won't discuss them in any depth.

This thesis deals with the hard probes. Examples of hard probes are jet correlations, analysis of , and measurements of heavy-flavor decays. High momentum jets, direct photons, and all start with a hard scattering early in the collision. Jets and direct photons are subjects in their own right and are not discussed further in this thesis. We will focus on heavy-flavor as a hard probe from here on.

2.2 Charm Quark Production in pQCD

It has been concluded from measurements performed by PHENIX [68] that charm production obeys . Simply stated, whenever we have a process that scales with N_{coll} as called for in perturbative quantum chromo-dynamic predictions, we say that process obeys . Plotted in Fig. 2.6 is the multiplicity of

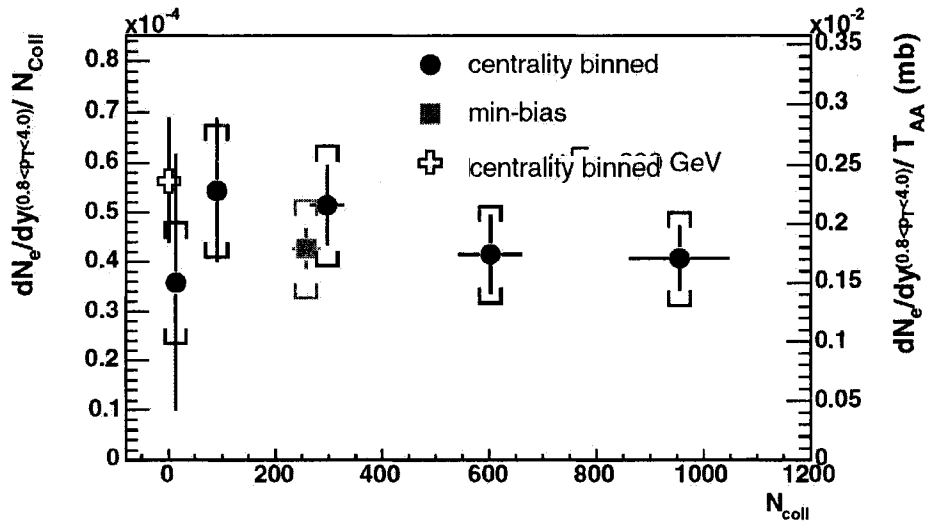


Figure 2.6: Multiplicity of electrons as a function of N_{coll} from Au + Au collisions together with the p + p result. The data exhibits the binary scaling of charm production.

electrons in Au + Au collisions as a function of the number of binary nucleon-nucleon collisions, N_{coll} . The data are consistent with a flat line. This shows charm production obeys binary scaling.

Shown in Fig. 2.7 are the lowest order diagrams that contribute to the production of charm quark-anti-quark pairs. The first diagrams, a and b, are usually referred to as and quark-antiquark annihilation. The others have names as well but the diagram says as much as the names do so I won't bother with them except to say that it pays to think of them mostly as radiation.

Later on we will see more about the production mechanism when we examine the p_T spectrum of single-electrons from p+p collisions. Theoretical predictions which include next-to-leading order diagrams, do not provide an accurate description of the data just yet – but more on this later. For now it is

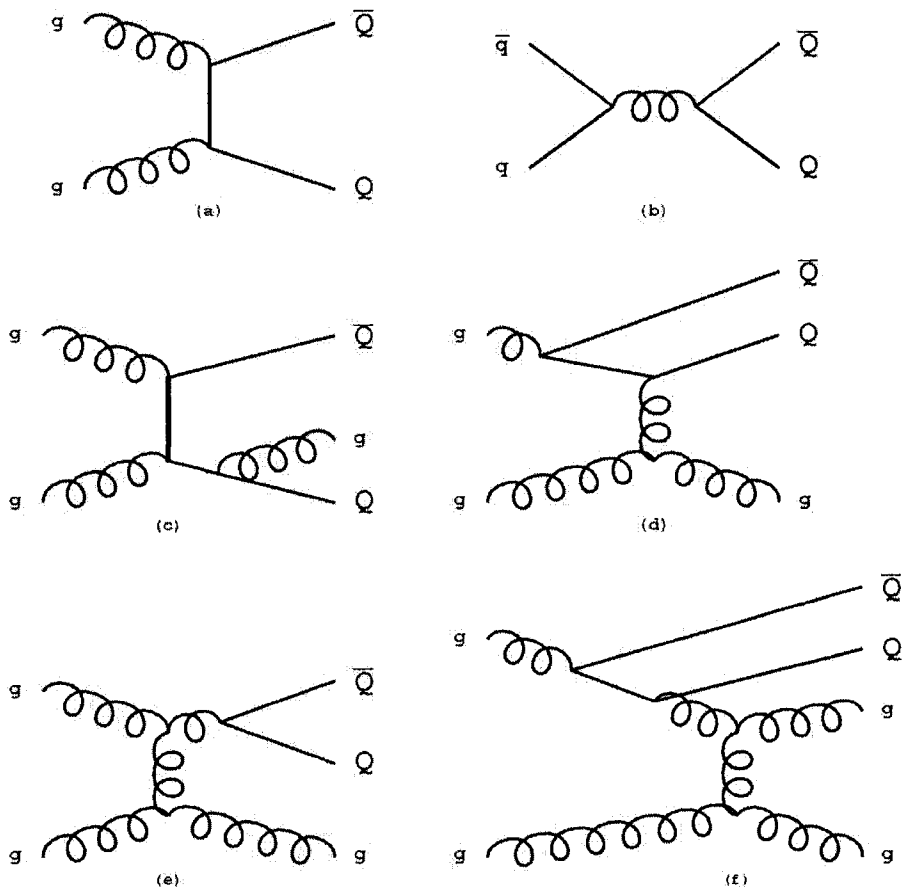


Figure 2.7: Feynman diagrams of first, second, and third order charm production. a) and b) are the largest leading order contributions. The rest of the diagrams amount to [13].

enough to know that the diagrams of Fig. 2.7 are the ones used in the current predictions and reflect the extent of our understanding at this time.

It is believed that gluon fusion ($gg \rightarrow c\bar{c}$) is the primary production mechanism. This is a consequence of the gluon distribution functions that are usually employed and the large mass of the charm quark⁸. However, to say that we know all of this for certain would be misleading. QCD calculations indicate these statements are correct but there are large uncertainties in the calculations. Leading order and next-to-leading order calculations have been done perturbatively from first principles, but we just don't really know yet.

Each of the calculations are stongly dependent on the values used for parameters of the theory. The mass of the charm quark is not precisely known and our current measurements indicate it lies somewhere between 1.15 - 1.35 GeV. The renormalization scale and factorizations scales are unknown⁹. There are many possible parton distribution functions that can (and are) used as inputs to these calulations. There are many more comprehensive discussions on the production of charm [14].

It is a goal of this thesis to examine modifications of Au + Au single-electron spectra with respect to a binary-scaled p + p single-electron spectrum.

⁸The are often what makes the calculation difficult or easy, or perhaps even just possible.

⁹Be aware of the difference between parameters that are model dependent and those that are not. The current masses of the quarks are constant values that have nothing to do with a model. They are what they are. Their physical values remain the same regardless of what the model being used to describe the particles says. Renormalization scales and factorization scales are NOT constants of nature. They are merely part of the model being used.

2.2.1 Energy Loss Mechanisms

Most of the intense discussion revolves around the manner in which a hot, dense, medium influences the particles. The natural question to ask about particles passing through matter is how they lose energy as they pass through the medium. Energy loss of particles passing through matter is well understood from the electromagnetic perspective and forms the basis for most of the principles of particle detection in our field [18]. This is not so for the and our medium is dominated by the strong interaction. If within the collisions at RHIC, we have created a medium dominated by strong interactions, any successful theoretical description that can explain all it's aspects and will be the first of its kind.

As a medium whose properties are determined by the strong force, energy loss will be dominated by strong interactions and not electromagnetic (although the electromagnetic force is still present). Our method is to take the electromagnetic case as our guide and try to proceed from there, but things will of course be different since we are talking about two different forces of nature.

The charm quark is important for a number of reasons. The dead cone prediction is one of them [19]. We know that charged particles electromagnetically radiate photons as they accelerate or decelerate passing through a field. It is reasonable to think that the same type of energy loss mechanism exists for the strong interaction. There will be differences though, since the kinematics of the strong interactions affect the heavy particles differently than the light

ones.¹⁰ When writing down the expression for the resulting gluon radiation,¹¹ it is seen that the radiation is suppressed at small angles. Small angle in this case refers to angles such that,

$$\theta < \frac{M_{charm}}{E}. \quad (2.1)$$

We are of course very interested in the idea and we want to test the prediction. Shown in Fig. 2.8 is a plot of the predicted ratio of angular intensity for gluon radiation from charm quarks and light up and down quarks. The two curves represent two different values of transverse momentum that are taken as reference values; the dashed is for 100 GeV and the solid is for 10 GeV. Note that the variable along the x-axis is a dimensionless quantity representing the fraction of the reference value. Most plots shown later on in this work will stop at a p_T of 5 GeV so we are interested in the first half of the solid curve.

¹²

Just as there are many ways to lose energy electromagnetically, there are many ways for charm to lose energy strongly. Again looking to our electromagnetic guide, we believe there is another energy-loss mechanism with a strong force analogue. When electrons are accelerated, the electromagnetic fields are squeezed down in the direction of motion. This is true of many radiation fields.

When fields are strengthened in the direction of motion and the motion takes

¹⁰In our case heavy means a charm quark and a light one means up or down.

¹¹Bremsstrahlung

¹²Built into this prediction are some assumptions about the characteristics of the medium. \hat{q} , the and L , the length of the medium were given reasonable values for the purposes of generating the plot in 2.8. The value of \hat{q} taken here is a little low based on the comparisons of our measured nuclear modification factors to the theoretical predictions shown in Sec. 6.1.

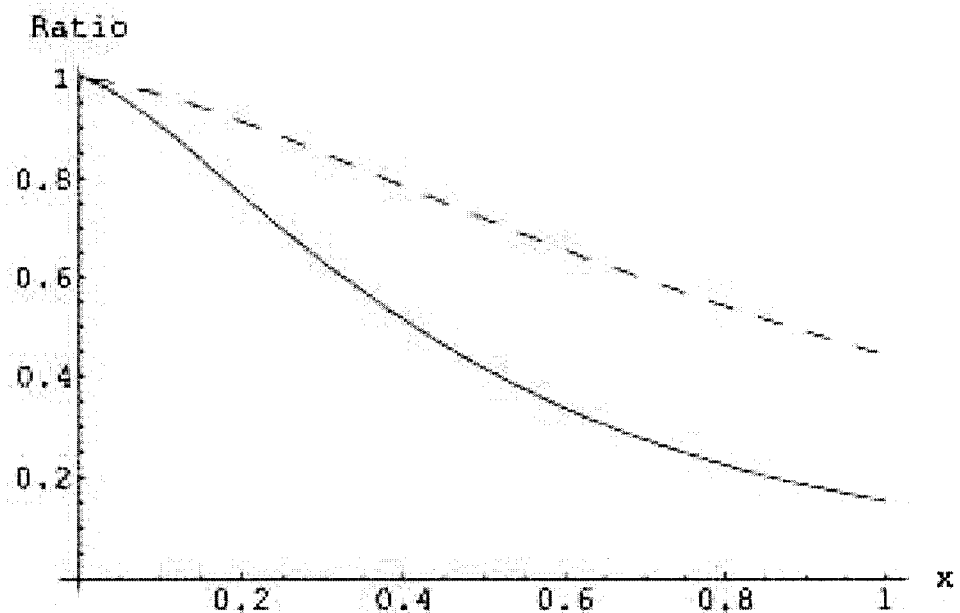


Figure 2.8: Ratio of gluon emission spectra off charm and light quarks for quark momenta $p_T = 10$ GeV (solid line) and $p_T = 100$ GeV (dashed) in hot QCD matter ($\hat{q} = .2$ GeV 3 , L=5 fm); $x = \frac{\omega}{p_T}$ taken from [19].

the particle through a medium that can be polarized, the polarization of the medium will affect the original field – and so on and so forth...

This is the Ter-Mikayelian effect [21] and has been thoroughly studied for electromagnetic interactions. It is believed that the strong interaction version exists as well and will result in energy loss of strongly-interacting particles, most notably, the charm [20]. The prediction is that energies less than the plasma frequency will be suppressed ($E < \omega_{plasma}$).

Other considerations enter as well. We assume the fireball has a finite size even though the true dimensions are not known. Since the region is finite, there must be a transition between plasma and non-plasma. At any such electromagnetic transition, there must be electromagnetic radiation [22]. We use this transition radiation to create particle detectors¹³ and is considered a common technique. It must also be true that for a strong transition interface there must be strong radiation. We expect this to be in operation for the collisions at RHIC. Calculations have been carried out and predictions made [23].

The question of energy loss is a complicated one and there are many approaches. Which energy loss mechanism or mechanisms you take is dependent on the models you choose to utilize and believe in¹⁴. The various models are all very much related. Each one is an attempt to characterize the bulk properties of the medium. Bulk properties are those parameters that define the medium. This is a good example. In diffusion models, the transport coefficient, \hat{q} is an average measure of how well energy is exchanged on the microscopic

¹³Cleverly known as Transition Radiation Detectors (TRD's).

¹⁴See the comparisons of the measurements of this analysis to the theoretical predictions in Sec. 6.1 for some specific references to the literature.

scale. A simple way of thinking of this is as a coefficient of a term in a written down to describe the system. Higher transport coefficients mean energy can be transferred easily resulting in larger energy losses for quarks, most notably the charm. Larger energy loss translates into suppression when looking at ratios of spectra from Au + Au and p + p. A carefull study of the charm present that is not contained in bound states, called , will give us the means to pin down these properties so I point to this as one of the goals of the thesis.

2.3 Known Experimental Results for Possible Medium Effects

From the preceeding discussions, one can see there are many motivations for a study of open charm. To that end, we have listed the major ones. Now we should look and see how much we really know about the collisions from a bird's eye view. RHIC is a tool that has done many things and has many capabilities. It's design allows for the collisions of all sorts of particles and ions. Each type of collision can tell us different things about what happened before, during, and after the interaction has taken place.

With that in mind, let's make a breakdown of the collisions by species that have already been setup in past and current runs and examine the uses of each with an eye towards their experimental value as probes of a possible strongly-interacting quark-gluon plasma.

2.3.1 p_T Spectra By Species

p + p

The first and arguably most important of the collisions are the proton-proton collisions. We think of the single-electron proton-proton spectrum as a reference. More precisely, these collisions are thought of as cold ones (relatively speaking) with a low energy density and are not expected to create a medium. The resulting spectra should be exactly like those created from the normal scattering of two protons.¹⁵ Accelerators around the world have done this already.

Typically we compare spectra from a p + p collision to the spectra from collisions with other species and look for differences. Ratios are made and if the resulting shape deviates from a flat one we know the collision was different than the p+p.

d+Au

A natural thing to do is look for a dependence of anything interesting we see on atomic numbers. The deuteron is a natural step on the way to Au+Au. For the experiments we perform using PHENIX, we look at d + Au as an intermediate step somewhere between with medium and without, but the reasons go beyond that and they will be discussed shortly.

¹⁵If you believe that there is such a thing as “normal” scattering, you can take this to mean a scattering of protons on protons at an accelerator like the Tevatron at Fermilab.

Au+Au

Au+Au is considered RHIC's hot energy-dense collision in which (we believe) a strongly interacting quark-gluon plasma is created. Estimates suggest the energy-density within the collision should be high enough and so the creation of the medium would be consistent with our current understanding of the strong interaction. To put the energy density that is achieved at RHIC in perspective, consider the energy density in normal matter,

$$\frac{m_N}{V_N} = 0.17 m_N fm^{-3} = 0.16 GeV fm^{-3} \quad (2.2)$$

The collisions at RHIC between gold nuclei have a center of mass energy of 200 GeV resulting in an energy density of

$$\epsilon = 1 GeV fm^{-3} \quad (2.3)$$

for a length of time

$$\tau = \frac{2R}{c} \quad (2.4)$$

with R representing the dimension of the system.

There is already a wealth of data suggesting that the medium exists. It is clear from PHENIX measurements that jets passing through the medium disappear. Jet suppression is seen and documented in a number of results [24], and while it is compelling evidence taken by itself, there is other evidence that supports the conclusion. PHENIX measurements of the neutral pions and charged hadron spectra show a suppression dependent on centrality and

transverse momentum [25]. The presence of a medium is predicted to have this effect. Since the pions are up and down quarks in bound states, when we look at their spectra we should be looking at medium effects associated with light quarks. The main result of this thesis is a similar statement, concerning the heavier charm quarks.

2.3.2 Current Status

As physicists, it is our job to try and draw conclusions from all of this information. The obvious conclusion already stated is: RHIC has created a deconfined state of matter. There is a large body of results that support the statement but there are uncertainties and questions to address. Strictly speaking, the current experimental results from RHIC show the following:

- There is a modification of hadronic particle spectra in central Au + Au collisions as compared to binary-scaled p + p spectra,
- The spectral modifications are final state effects (e.g. parton energy loss in a dense medium is a possible explanation), and
- Jet quenching is present.

Is that enough to claim the QGP is there? Some physicists say yes, but for me, these items alone are not enough. For confirmation, we may be tempted to look to the theoretical models. The unfortunate truth is that experiment is far ahead of the theory in our field. There is no theoretical model that can explain the existing data in a satisfactory manner. There are many efforts to

do so and each can explain some aspects – just not all of them simultaneously.

Examples follow in the next section.

2.3.3 Theoretical Models

Historically, the thermal (statistical models) were the first to really make any headway as comprehensive theories that described most aspects of the collisions. Fermi and Pomeranchuk were the first to propose their use in predicting ratios of particle yields [27] [28]. The models have evolved considerably and the most popular are now known as Hagedorn Resonance Gases that use a Statistical Bootstrap Model [2].

As of Quark Matter 2003, the current status of statistical models was summarized by A. Bialas [26] as follows:

- Statistical models of non-strange and string hadron resonance gases are a reasonable description of the final state of very central collisions at SPS and RHIC,
- Chemical and kinetic equilibrium seem to have been reached in the collisions, and
- The thermodynamic parameters are consistent with the expectations from theory.

In general, we can say the basic statistical models using the grand-canonical ensemble can predict most reliably and agree fairly well with the heavy-ion experiments. You may also be surprised to find out that the statistical methods are good at prediction in electron-positron collisions too! [30]

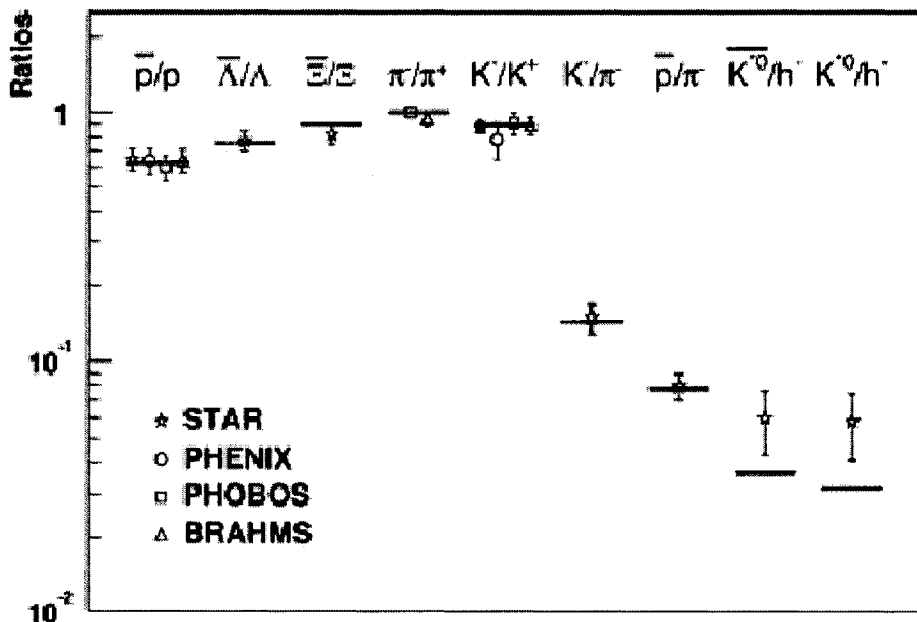


Figure 2.9: Statistical models are used to predict ratios of particle yields. [58]

2.4 Why do we care about charm?

Theoretically, the charm quarks provide us with a probe of any medium that is created in the collisions for reasons listed below. Each justification below is a separate area of study in which work is on-going.

2.4.1 Large Charm Mass

When performing calculations, things are greatly simplified due to the large mass. In general the cross sections for the processes we study become perturbative as a result. For the lighter quarks, this is not so, and non-perturbative methods are employed. This holds for other infrared-safe quantities too. In most cases, the large mass is what allows us to calculate and make predic-

tions. Our understanding of the lighter quarks is hampered by the difficult calculations themselves. As an example; we can calculate wave functions of J/Ψ (bound states of heavy flavors and their anti-particles). We just know more about the charm since we can actually calculate the relevant details.

Calculations of cross-sections involving charm quarks are possible because of the charm's large mass. In general, the cross-sections for the processes we are studying become non-relativistic and are non-perturbative, leading to simplifications. For the lighter quarks, this is not the case, and calculations are difficult or just not possible. In most cases, this large mass is what allows us to carry out calculations and make the relevant predictions. Sadly, our understanding of the lighter quarks is hampered because the simplifications are not present and the calculations are hard. As an example, we can calculate wave functions of J/Ψ (bound states of heavy flavors and their anti-particles). We just know more about the charm, since we can actually calculate the relevant details.

2.4.2 Yield As Baseline For J/Ψ Measurement

In the past, heavy-ion experiments were performed with the SIS, SPS, and AGS (among others). Energies were low per nucleon and the Drell-Yan process was the appropriate spectrum to compare to when making measurements of the J/Ψ . For RHIC this is not so. Drell-Yan here is small. In fact, it's tiny – or tiny when compared to open charm.¹⁶ Therefore the reference has changed. Almost all the charm that is created winds up as open charm in mesons such as the D. A very small fraction of the charm goes into bound states like the

¹⁶The Drell-Yan is three orders of magnitude smaller at these energies.

J/Ψ . If we wish to understand the J/Ψ , first we need to account for all the charm. The vast majority of it is open charm contained in mesons so that's what we measure.

2.5 How RHIC and PHENIX fit in Heavy-Ion Physics

We can now attempt to look at RHIC and PHENIX¹⁷ with a little perspective. RHIC offers the heavy-ion field a high $\sqrt{s_{NN}}$ as compared to earlier machines. Fig. 2.10 shows a plot of charged particle multiplicity as a function of center-of-mass energy per nucleon for the major experiments on the major machines in our field.

Whereas the older measurements offered tens of MeV per nucleon, the modern day RHIC smashes ions together at 200 GeV. This should be more than enough to create a medium in which hard QCD physics is taking place.

PHENIX (the Pioneering High Energy Nuclear Interaction eXperiment) is an experiment located on the RHIC ring. It is optimized for the detection of leptons and for the purposes of this thesis – it is used to measure the spectra of from the decay of open charm. (A.) The goal is to quantify the effects of any deconfined medium that may have been produced in the collision of Au on Au using ratios of single-electron p_T spectra.

Information about the medium is encoded in the spectra of those electrons and we aim to recover it.

¹⁷The PHENIX web page is located at <http://www.phenix.bnl.gov/> and is a good place to find more comprehensive information, papers, and people associated with the experiment.

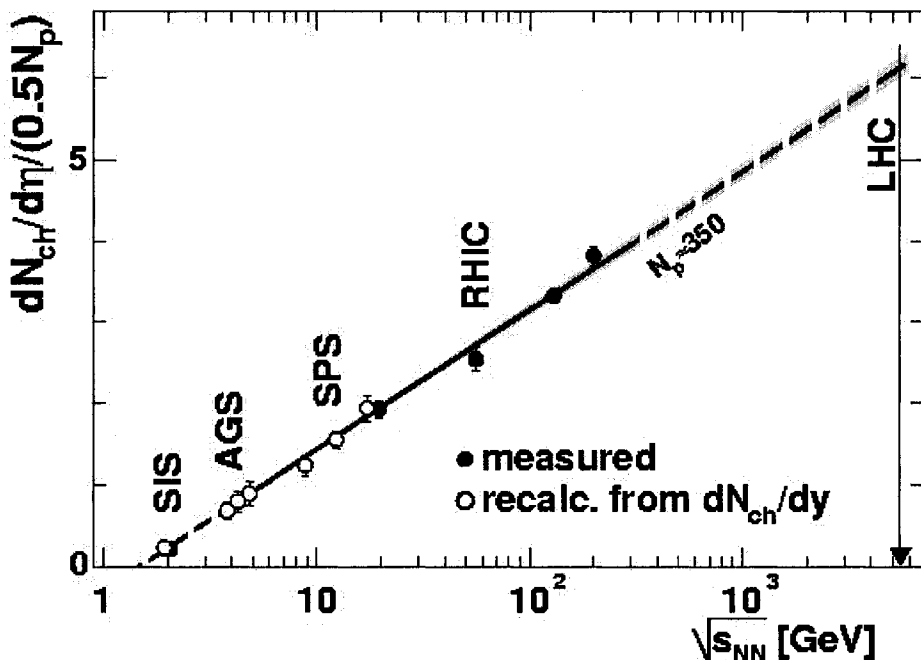


Figure 2.10: Charged particle yields per unit pseudo-rapidity as function of center-of-mass energy per nucleon in heavy-ion collisions. This plot is useful for understanding where RHIC fits in to the field as an accelerator. It is also worth noting how surprising it is that the production mechanisms seem to be similar over so many orders of magnitude [57].

2.5.1 Summary

This thesis is an accounting of single-electrons that result from the semi-leptonic decays of open charm mesons (D-mesons). This accounting will help to test the theories of charm production, energy loss of partons, recombination and coalescence, thermal modeling, radial flow, and thermalization. This list is not comprehensive, but it shows that the measurement is a hot topic that generates lots of interest. Consider yourself motivated. :)

This is also a good time to consider the progress we've made since the days of the BEVALAC. Recall the three goals stated in the beginning of the thesis; understand the QCD , understand the QCD phase diagram, and understand the nature of the QCD vacuum. While some might say we understand everything about a quark-gluon plasma and paint a rosy picture – I will not. Sadly, there are many areas in which we don't know much more now than we did in the early 70's. However I am happy to report that we have made substantial progress on the QCD phase diagram.

The diagram shown in Fig. 2.11 contains the phase diagram for QCD as we know it today. Various experiments probe the different parts of the diagram and some points are plotted for them. It is believed that RHIC collisions follow along the left-most vertical (electronic version: green) line, working our way from the top where the initial collision takes place, down to the bottom at freeze-out.

We may have found something much more interesting than a QGP. Perhaps, we have created a *strongly-interacting* QGP. The distinction may well turn out to be important.

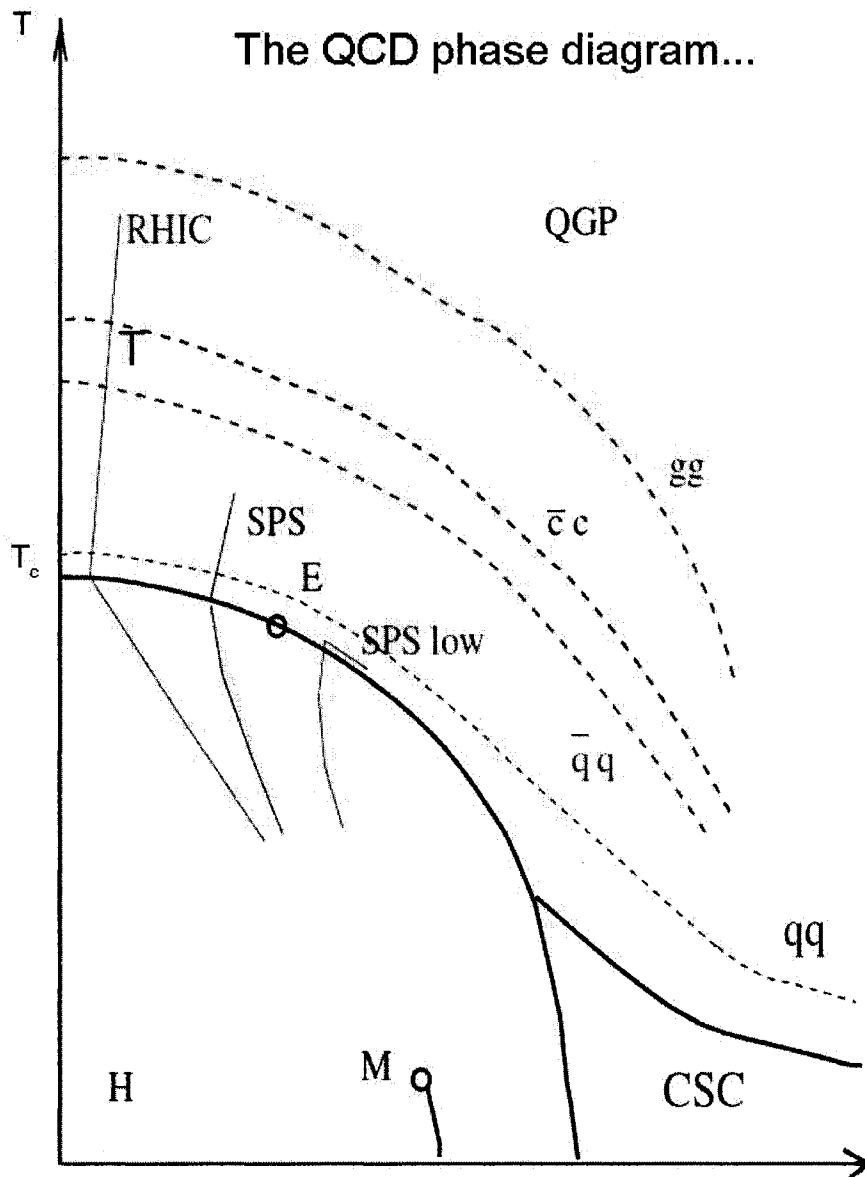


Figure 2.11: QCD phase diagram showing the hadronic phase (H), the quark-gluon plasma (QCP), the color super-conducting phase (CSC), the end-point of the first-order line (E), and the end of the nuclear liquid-gas line [multi-fragmentation] (M) [54].

In normal electromagnetic plasmas we know that bound states can persist within the plasma and the phenomenon is well documented. The particles within the plasma still feel an interaction strong enough to allow for a mixed phase and so we call the plasma strongly interacting. Recently, Shuryak and Zahed [54] have proposed that this same mechanism is present in RHIC collisions, within our QGP, but the interaction is that of the strong nuclear force rather than the electromagnetic.

The dashed lines in 2.11 correspond to the breakup of the bound states indicated. RHIC seems to operate above the charm line but below that of the gluons so there seem to be bound colored states present in the collisions as well.

All of this is very new and exciting, but currently has no experimental confirmation. We will see in the near future. Nevertheless, our point is made. Our understanding of the plasma is more sophisticated these days so significant progress has and is being made today.

Chapter 3

RHIC and the PHENIX Experiment

Rather than present a detailed description of RHIC, I will just mention some of the highlights in terms of design goals and constraints. More comprehensive information is available ¹.

With RHIC, the designers wanted to be able to:

- collide heavy-ions (e.g Au) at 100 GeV/u per beam;
- collide lighter species and protons on heavy nuclei as well;

The heaviest system RHIC works with is Au + Au. On the way to 200 GeV Au + Au collisions however, there are many other ions and energies ². Experiments before PHENIX, located at SPS, AGS, and SIS, have results that we need to compare to and expand upon. For this reason, RHIC can accelerate many species of varying masses and positive charge, all the way down to deuterons and protons. These lighter

¹The most up to date and detailed information can be found on the Collider-Accelerator Department webpage located at <http://www.bnl.gov/cad/> where links to the original and current papers can be found.

²For example, RHIC has worked with Cu + Cu.

collisions are necessary, because they give us something to compare with when interpreting the heavies.

- Collision of different species at equal energies per nucleon

Not only do we use symmetric collisions, we use asymmetric ones as well. d + Au is our shining example. One can imagine the collisions in this case as the smaller deuteron puncturing the gold during the collisions. We can use the deuteron to help examine, among other things, cold nuclear matter effects. [32].

- Use of polarized beams for a spin physics program

We are now entering the next phase of physics at RHIC where we examine how the proton gets it's spin. The spin program is extensive and well documented [33] [34]³.

- Achieving beam luminosities of $10^{26} - 10^{27} \text{ cm}^{-2} \text{s}^{-1}$ for Au + Au collisions

Expectations for luminosity have been surpassed. In general, the performance of the accelerator has been excellent and we expect the same to continue for a long time to come.

Such a top-notch accelerator pushed the limits of technology. Naturally there were a list of constraints that had to be dealt with:

- the small ring size and bending power of the magnets were known constraints forcing the use of super-conducting technology

On the other hand, they require more technical know-how; and

³For an overview of the PHENIX spin program, visit <http://www.phenix.bnl.gov/www/physics/spin/> where there are plenty of links to get pointed in the right direction.

- collisions of different species lead to different magnetic rigidities so two rings with independent magnetic optics were necessary

One may ask why we haven't had p+A collisions yet at RHIC. The RHIC design in a sense forced us to choose d + A over p + A.

In accelerator physics, the magnetic rigidity is defined in the following way; for a particle in a dipole field with charge, e, and moving in a circle with radius of curvature, ρ , the non-relativistic force is

$$F = evB = \frac{mv^2}{\rho}. \quad (3.1)$$

We can rewrite this and take the definition of magnetic rigidity to be

$$B\rho = \frac{mv}{e} = \frac{p}{e} = 3.3356p[Tm] \quad (3.2)$$

for p in [GeV/c]. At RHIC, this becomes

$$B\rho = 3.3356 \frac{A}{Z} M \beta \gamma \quad (3.3)$$

where M is the mass per nucleon and $\beta = \frac{v}{c}$ and $\gamma = \sqrt{\frac{1}{1-\beta^2}}$ are the usual relativistic variables.⁴

⁴Here are some example rigidities for three of the species (gold, deuteron, and proton) we work with at RHIC:

$$B\rho_{Au} = 7.7450 \beta \gamma, \quad (3.4)$$

$$B\rho_d = 6.2564 \beta \gamma, \quad (3.5)$$

$$B\rho_p = 3.1297 \beta \gamma. \quad (3.6)$$

The angular deflections are different for different species, but it's really the A/Z that controls things. When the rigidities are different, the accelerator folks have to fuss with the dipoles to line things up properly in the interaction regions. So we go with the $d + A$ instead, since they line up easier and tell us mostly the same things.

- Slow ramping super-conducting magnets require passing through the transition energy

A common difficulty with accelerators is associated with the transition energy. Each time a particle passes around the ring, it receives a kick from the RF cavities. Kicks increase speed, and hence the momentum. The velocity decreases the time it takes to pass around the ring. The momentum increases it because the momentum kick increases the arc length of the path the particle follows. The energy where these two effects cancel is called the transition energy. It is considered an unstable point in the ramping process and we do everything possible to avoid it in an effort to maintain the beam luminosity.

Since the magnets are super-conducting, they ramp slowly, forcing us to design a ring that passes through the transition energy. Skilled RF acrobatics are performed and the particles effectively jump over the transition energy.

3.1 RHIC

The RHIC complex is shown in Fig. 3.1. The two rings of the collider are horizontally separated by 90 cm in a tunnel with a circumference of 3.834 km. Stripped Au ions and other species, circulate in opposite directions as in most colliders. There are six insertion regions that provide us with collisions and these are connected by six arcs. Bending is provided by a bevy of magnets used in both rings. The magnetic breakdown is as follows: 288 arc dipoles, 276 arc quadrupoles, 108 insertion dipoles, and 216 insertion quadrupoles, 72 trim quadrupoles, 288 sextupoles, and 492 correctors. Each magnet uses superconducting technology to achieve it's bending power. The technical specifications of RHIC are summarized in Fig 3.2 [48].

Presently there are five experiments on the ring at RHIC. They are PHENIX⁵, BRAHMS⁶, PHOBOS⁷, STAR⁸, and pp2pp⁹. Each is described in detail in various places. I will mention only that PHENIX and STAR are the larger dominating detectors and their measurements very often complement each other. Essentially they are large general purpose experiments but we can say something about their emphasis. PHENIX is especially good when working with leptons and STAR excells with measurements benefitting from a larger acceptance.

⁵<http://www.phenix.bnl.gov>

⁶<http://www.bnl.gov/RHIC/bhrams.htm>

⁷<http://www.bnl.gov/RHIC/phobos.htm> Note: PHOBOS has just shut down and stopped taking data.

⁸<http://www.bnl.gov/RHIC/star.htm>

⁹<http://www.rhic.bnl.gov/pp2pp/>

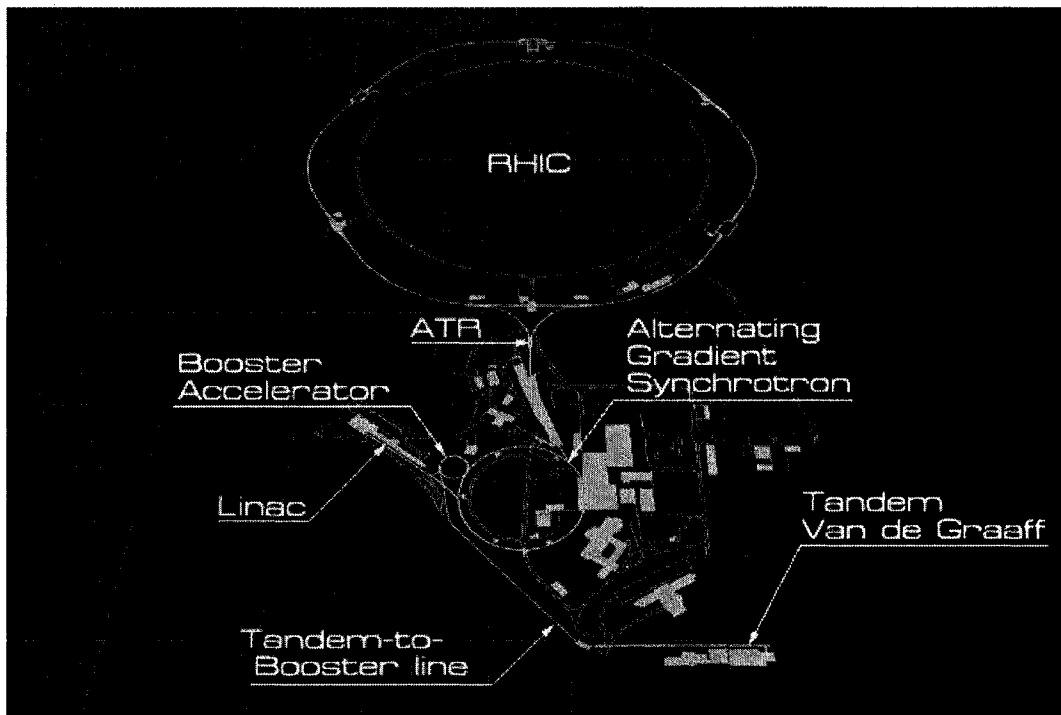


Figure 3.1: Schematic of RHIC and the supporting machines located at Brookhaven National Laboratory in Upton, NY. [47]

Parameter	Value
Kinetic Energy, Injection-Top (each beam)	Gold: 10.8 – 100 GeV/u Protons: 28.3 – 250 GeV
Luminosity, Au-Au at 100 GeV/u	$2 \cdot 10^{28} \text{ cm}^{-2} \text{ s}^{-2}$
Operational lifetime, Gold	10 hours
No. of bunches/ring	60
No. of particles/bunch	Gold: 10^9 (at times, a few 10^7) Protons: 10^{11} (upgrade, $3 \cdot 10^{11}$)
Bunch length	from 20 ns down to 1 ns
Normalized Emittance, gold	Injection: $10\pi \text{ mm mrad}$ After 10 hr: $40\pi \text{ mm mrad}$
Filling mode	Bunch to bucket, 30 Hz peak rate
Filling time	1 min, each ring
Acceleration time	75 s
Revolution frequency	About 78 kHz
rf harmonic number	Acceleration system: $h = 360$ Storage system: $h = 2520$
Beta at crossing, H,V	During injection: 10 m Low beta insertion: 2 m
Transition energy	$\gamma_T = 22.89$
Circumference	3833.845 m
Beam tube i.d. in arcs	69 mm
Vacuum, warm beam tube sections	$7 \cdot 10^{-10} \text{ mbar}$
Operating temp., helium refrigerant	< 4.6 K

Figure 3.2: Technical parameters and specifications of RHIC [48].

3.2 PHENIX

PHENIX is a union of many separate subdetectors, each with a different focus and purpose. Fig. 3.3 shows a schematic of the detector and all of the active subsystems as of Run II (2001).

Not all of them are used for this measurement of open charm and so I will only quickly describe those that are involved. As a framework for that discussion, I break them into three categories of detector; those for triggering, those for track reconstruction, and those for particle identification.¹⁰

3.2.1 Triggering With the BBC and ZDC

To capture the sample of events used in this analysis, we employ a triggering system. Two subsystems form the backbone of the event triggering system. They are the Zero-Degree Calorimeter and the Beam-Beam Counter, referred to as the ZDC and the BBC. A schematic in Fig. 3.4 shows the location of these two subsystems.

The BBC detects charged particles at angles very close to the beam between 2.4 deg and 5.7 deg. The collision time and vertex position can be calculated from the average and difference between the times measured in the North and the South BBCs as shown in Fig. 3.5. Vertex position then becomes the basis for our first layer of triggering.

Mechanically, the BBCs are constructed as 2 arrays of 64 smaller components arranged in a ring-like pattern around the beam. Each of the smaller

¹⁰For a full and detailed discussion about the PHENIX detector please consult the special issue of NIM devoted to RHIC [35] which contains reasonably up-to-date information for each subsystem of the detector.

PHENIX Detector - Second Year Physics Run

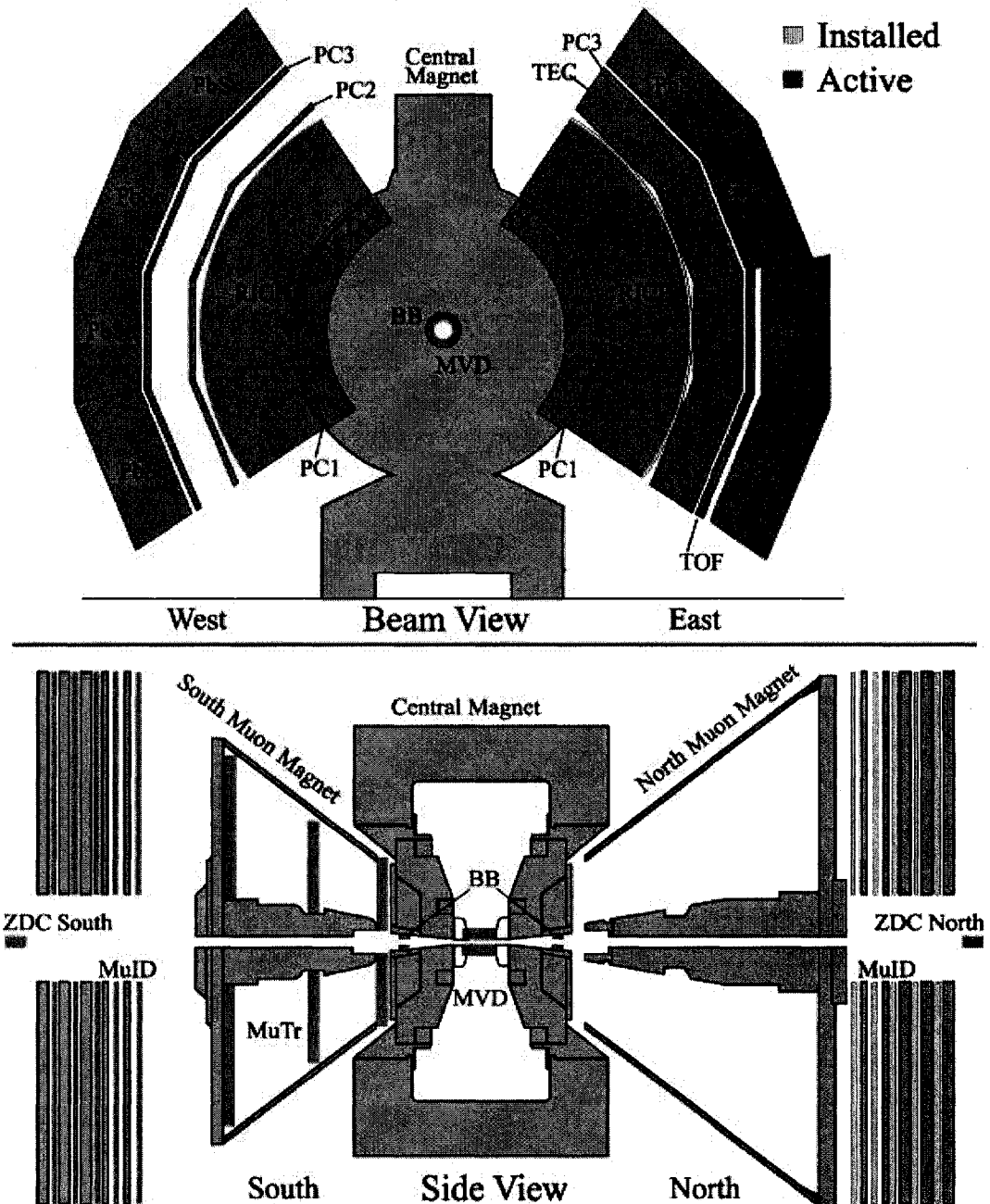


Figure 3.3: Schematic of the PHENIX detector and status of each subsystem as of Run II (2001). Upper panel: all subsystems active. Lower panel: Muon identification subsystem was the only subsystem not active. (Electronic version: active detector subsystems are shown in red.)

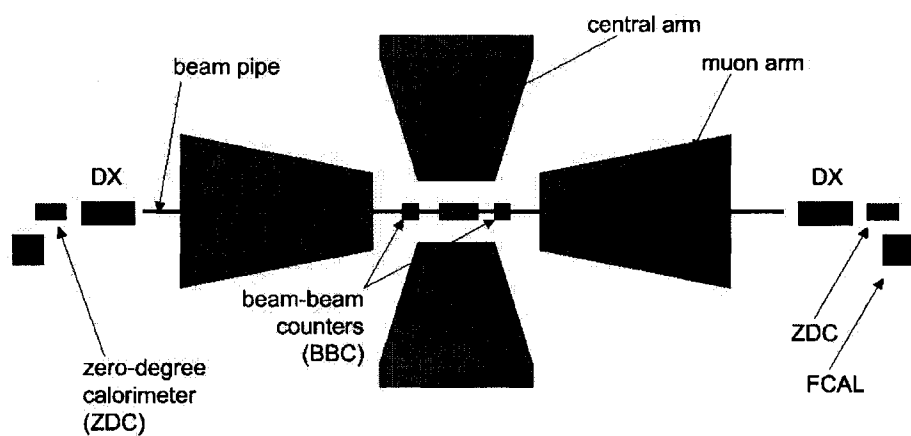


Figure 3.4: Schematic of the PHENIX detector showing the location of the Beam-Beam Counter (BBC) and the Zero-Degree Calorimeter (ZDC). This is taken from a PHENIX Focus presentation given by Dave Morrison of the PHENIX collaboration given during Run V.

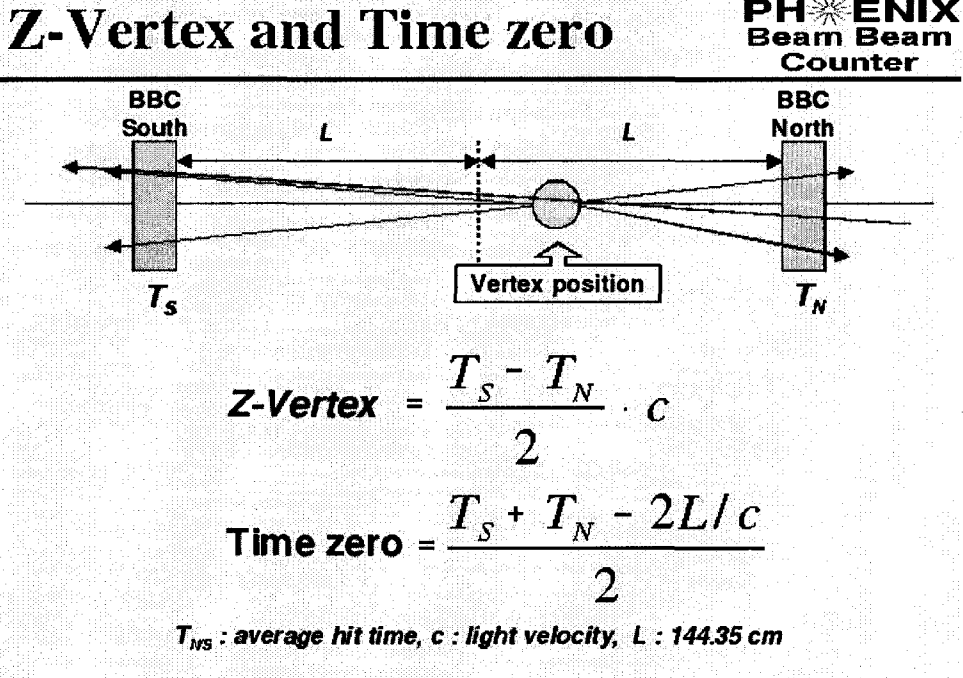


Figure 3.5: Using the Beam-Beam Counter to determine the starting time and the z-vertex of an interaction. Taken from Tomoaki Nakamura's PHENIX Focus presentation given during Run IV to the new students of the collaboration.

components is really a hybrid Cherenkov detector and photomultiplier tube combined into one piece. High-voltage and readouts are wired up to the back-end to retrieve the signal. The full description is found in [42]

If the BBC's focus is on the charged particles, the ZDC focuses on the neutrals. Collisions between the nuclei in the interaction region always result in the creation of neutral particles. These are fragments of the beam remnants. In both cases, neutrons end up shooting off in both directions, very close to the beam. The charged secondary particles are sifted out when they reach the DX dipoles located on both sides of the IR. This makes the region 17 meters down-stream behind the DX magnets, a nice place to place our Zero-Degree Calorimeter. Fig. 3.6 diagrams the trajectories of the various particles (charged and neutral) that enter and leave the IR through the beam pipe.

The main purpose of the ZDC is to measure the total energy deposited by the small angle neutrons that emerge from the IR. The energy deposited can be converted into a multiplicity which is then combined with information from the BBC's output to form a centrality. Since the charge in the BBC and the energy in the ZDC are both correlated with the event geometry, they are correlated to each other. This is the heart of our determination of centrality in the PHENIX experiment and more details will be given below. The energy deposition can also be used as a luminosity monitor and coincidences between the two ZDC contribute to the minimum bias trigger.

The ZDCs are hadronic calorimeters that are meant to measure neutrons. Schematics are shown in Fig. 3.7. The biggest constraint on the project was the limited space available. The spacial distribution of the neutrons doesn't have any information that PHENIX needs so the detector was designed with

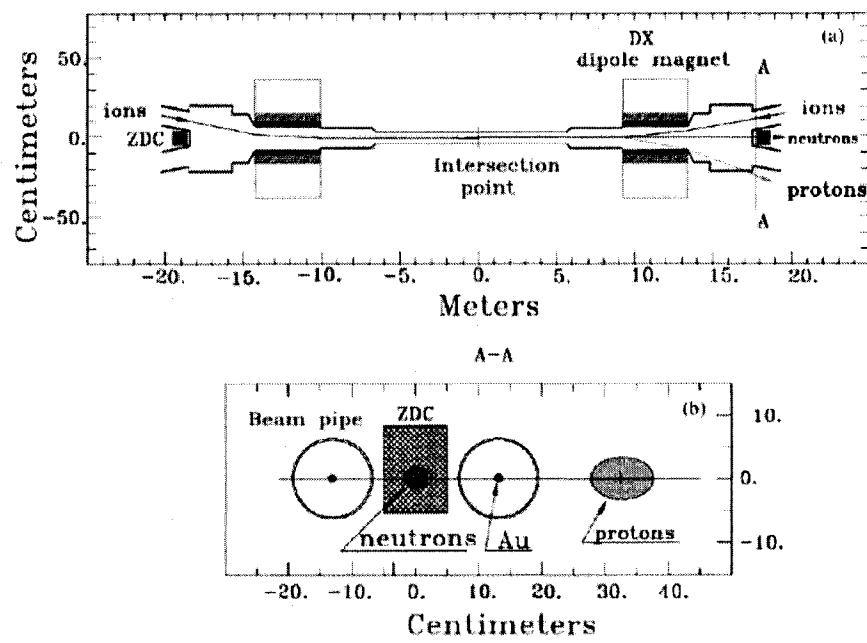


Figure 3.6: The trajectories of various particles (charged and neutral) that enter and leave the IR. [50]

out any segmentation transverse to the beam. As with all calorimeters, the energy resolution must be specified up front. In this case, the resolution was driven by the need to resolve the neutron peak.

There are three aspects of the triggering based on these detectors that we are concerned with; centrality, participants and spectators, and the position of the vertex.

Centrality is a generalization of impact parameter. You may take it as a measure of how head-on the collision of two particles is. The range of centrality takes on values between 0 and 100, with 0 being a direct head-on collision and 100 is a peripheral or grazing collision where the ions just barely interact. Fig. 3.8 shows the anatomy of a collision at RHIC with intermediate centrality. We use the correlation between the ZDC and BBC to map an event to our generalized impact parameter called centrality. The entire data set is split up into centrality classes and we can examine the dependencies of spectra on this centrality. Centrality classes, commonly used in this analysis are 0-10, 10-20, 20-40, 40-60, 60-80, and 60-92%. Centrality is one of those terms that lies at the core of our experiment so it must be carefully defined.

The end result is a plot that makes us think of the face of a clock as shown in Fig. 3.9. The plot shows that the BBC loses resolution for the very peripherial events. Such events are located below 0.1 in fractional charge along the horizontal axis. The ZDC is also seen to have a multiple valued response. As a function, the response is not invertible. These two pieces of information taken together tell us to use both signals to determine centrality.

¹¹The reason the calibration can change from run to run is that the response of the BBC

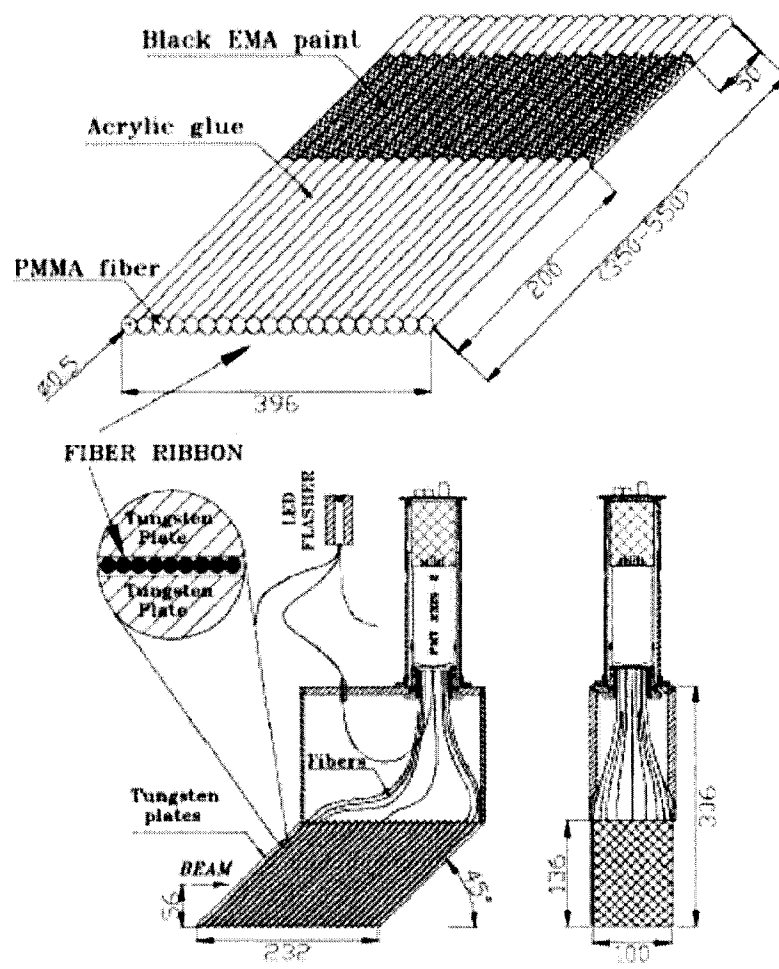


Figure 3.7: Mechanical deisgn of the RHIC ZDCs [50].

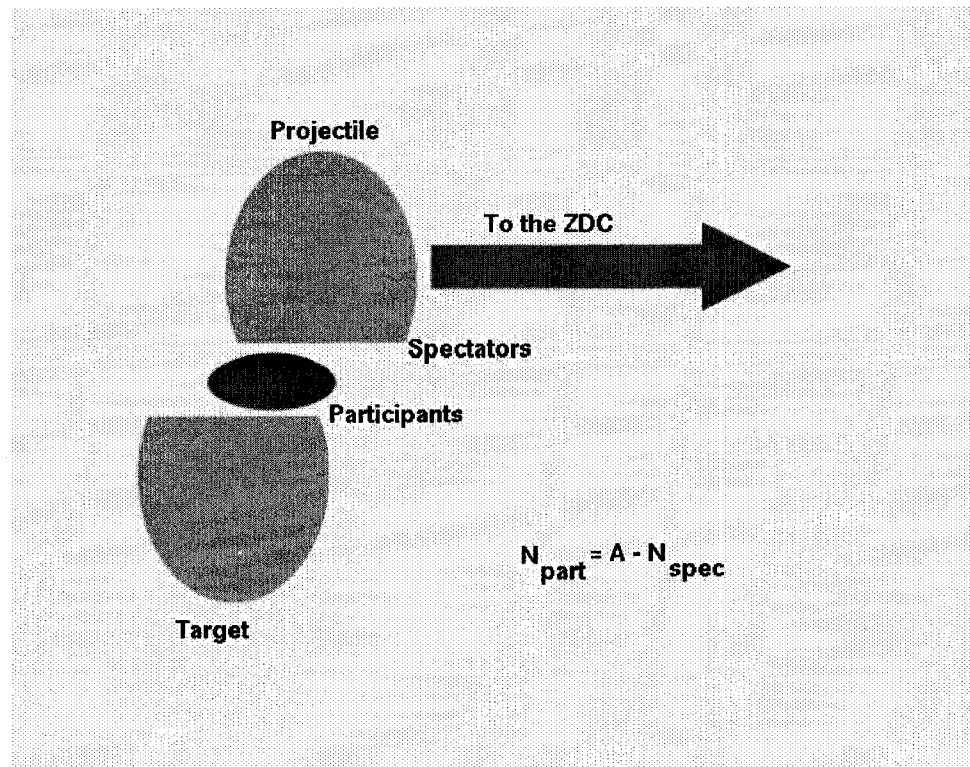


Figure 3.8: The anatomy of a collision in the participant-spectator model.
(shown at “PHENIX Focus 2005 - How to Measure Centrality.” by David Morrison, PHENIX collaboration, 2005-07-01)

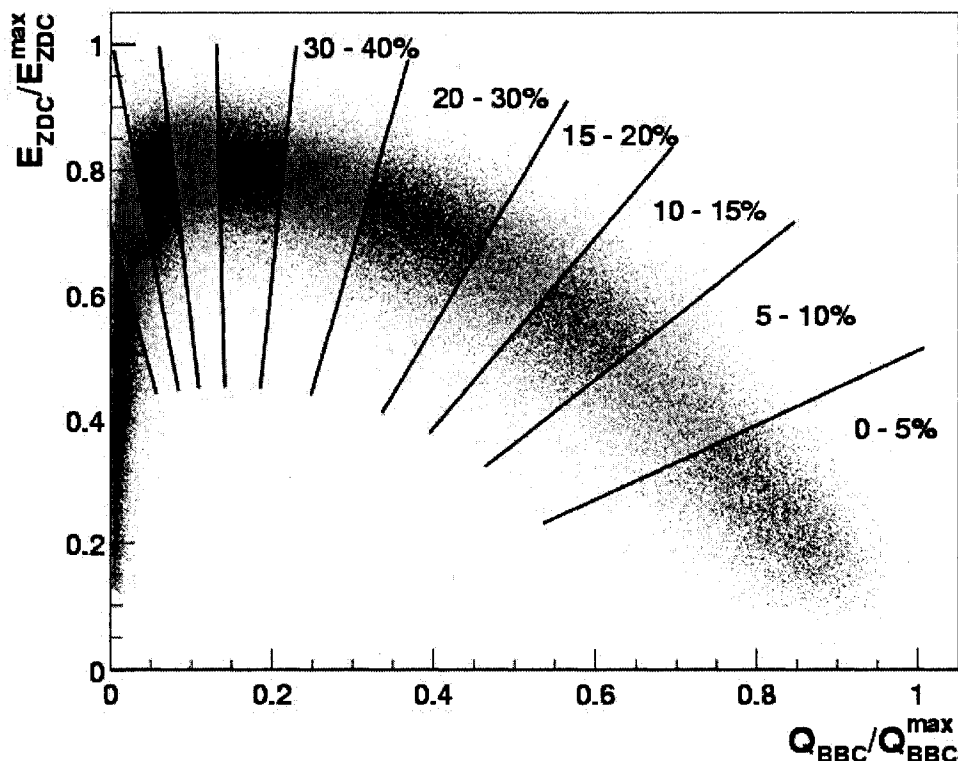


Figure 3.9: ZDC response vs. BBC response. Along the vertical axis is the energy deposition of neutrons normalized to the maximum value. The horizontal axis show the same for charge deposition in the BBC. This illustrates the “centbyclock” method of centrality determination. Each slice determines a range in percentages of centrality. (shown at “QM 2002.” by Tatsuya Chujo, PHENIX collaboration, 2005-07-01)”

When colliding the various heavy-ions, we need to know how many of the nucleons actually took part in the collisions. Some will scatter and are labeled participants, whereas the remainder, known as spectators, will just pass through the interaction region without taking part. The location of the BBCs (participants) and the ZDCs (spectators) far down stream was chosen so we'd pick up any spectators that pass through. Once you know how many spectators there were, you know how many participants there were.

The number of participants, spectators, and binary collisions are plotted as a function of impact parameter in Fig. 3.10.

A precise determination of the vertex position is critical for proper reconstruction of the tracks. The method used to determine the vertex position has already been described above (see Fig. 3.5).

3.2.2 Tracking

Tracking is the reconstruction of the paths of charged particles as they pass through the detector. Lots of effort has gone into designing a system that is adequate for our needs. The main subsystems involved in the reconstruction of tracks are the drift chamber (DC) and the first pad chamber (PC).

Drift Chamber

The drift chambers are multi-wire proportional counters of the sort used in most tracking. All the information contained in this section is from [49].¹²

and ZDC can be different. If we maintain the same calibration from run period to run period, we will end up labeling and thinking of many events as having a particular centrality when in fact, they will have VERY different "impact parameters".

¹²For a nice introduction to the principles of drift chamber operations, take a look at http://www.phenix.bnl.gov/WWW/tracking/dc/experts/Drift_Chamber_

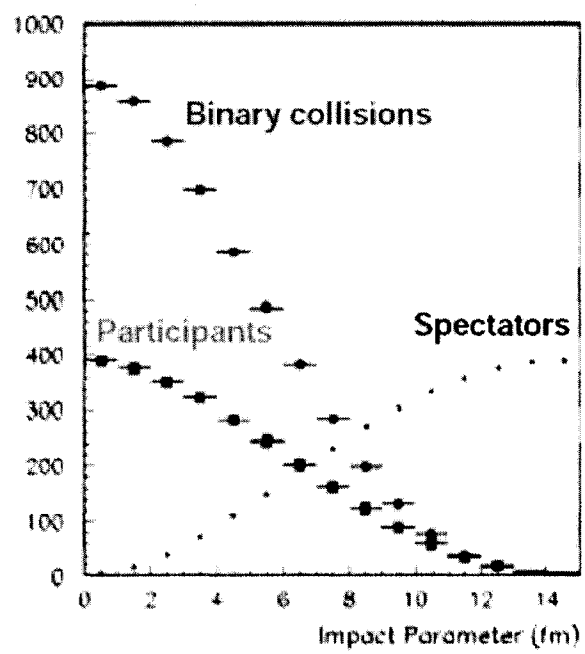


Figure 3.10: Number of participants, spectators, and binary collisions as a function of impact parameter. (shown at “CTEQ 2002” by Jamie Nagle, PHENIX collaboration, 2005-07-01) Au + Au at 200 GeV per nucleon.

The drift chambers (DC) are cylindrically shaped and located in the region from 2 to 2.4 m radially out from the z axis and 2 m along the beam direction. Each DC measures charged particle trajectories in the radial direction and determines their p_T of each. Simulations of ion-ion collisions at RHIC were used to determine the requirements on p_T resolution.

The goal was to measure the $\phi \rightarrow e + e$ mass with a resolution better than its natural width of 4.4 MeV and have good tracking efficiency for the highest particle multiplicities at RHIC. These considerations forced adherence to the following requirements: a single-wire resolution better than 150 μm in the $r - \phi$ directions, a single-wire two-track separation better than 1.5 mm, a single wire efficiency better than 99%, and spatial resolution in the z direction better than 2 mm.

The East and West arms are separate and independent volumes of gas. They are symmetric and each is the mirror image of the other. A cylindrical titanium frame establishes the gas volume and also gives the azimuthal and beam-axis limits. A diagram is rendered in Fig. 3.11. There are Al-mylar windows in the radial direction that measure five mil. Each frame is filled with drift chamber modules (or keystones) and is divided in 20 equivalent sectors covering 4.5 degrees in ϕ . There are six types of wire modules stacked radially in each sector: X1, U1, V1, X2, U2 and V2. Each module contains four anode planes and four cathode planes. These then form cells with a 2-2.5 cm drift space in ϕ .

The wires of the X1 and X2 layers run parallel to the beam and are shown in Fig. 3.12. These layers are used for precise track measurements in $r-\phi$. There

[_Principle_of_operation.html](#) This page was put together by Vlad Pantuev.

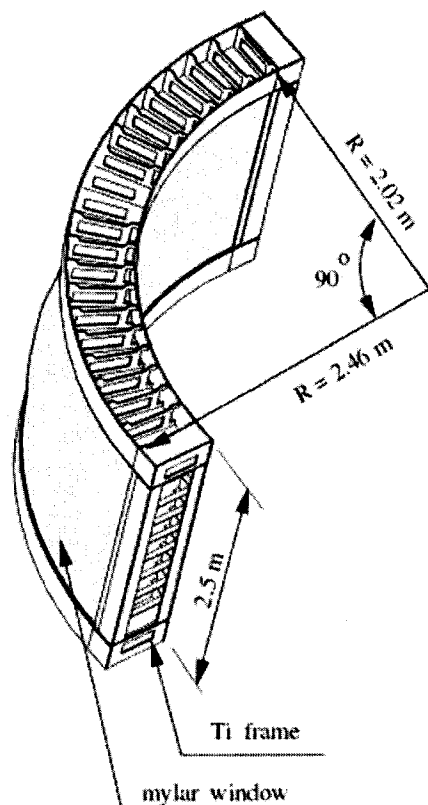


Figure 3.11: The PHENIX Drift Chamber frame construction [49].

are also two more sets of small angle U,V wire planes used only for pattern recognition. The U1, V1, U2, and V2 layers of wires have an orientation in stereo angle of six degrees relative to the X wires. The stereo angles allow us to measure the z coordinate of the track.

The wire configuration of the DC is unique (see Fig. 3.12). Its geometry eliminates any left-right ambiguity and reduces the number of potential tracks seen by each wire. At the same time it narrows the sampling length of primary electrons and improves two-track separation by decreasing the pulse width. The anode wires are separated by Potential (P) wires and surrounded by Gate (G) and Back (B) wires. P wires form a strong electric field and separate sensitive regions of individual anode wires. G wires limit the track sample length to roughly 3 mm and terminate unwanted drift lines. The time spread of drifting electrons from a single track is minimized and therefore decreases the pulse width. The B wire has a lower potential.

As charged particles pass through the gas it becomes ionized. The cascade of liberated charge drifts to the wires and the analog signal is read out. Signals of charge are translated into “hits” in the front-end electronics and those hits are used in the reconstruction of charged particle tracks.

Pad Chambers

The pad chambers (PC1, 2, and 3) are a subset of the tracking system used in PHENIX. They are multi-wire proportional counters with a segmented cathode read-out, radially layered at 2.5, 4.2, and 5.0 meters. Each layer is divided into 8 sectors. Fig. 3.13 shows their layout and orientation within PHENIX.

Each layer has evolved somewhat in function and they have taken on dif-

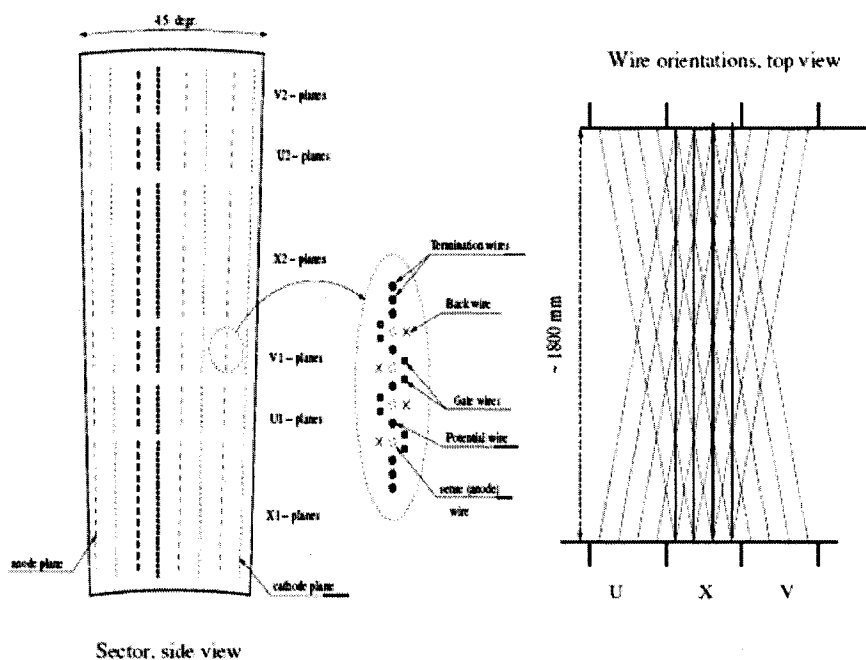


Figure 3.12: The PHENIX Drift Chamber wire layers and configuration [49].

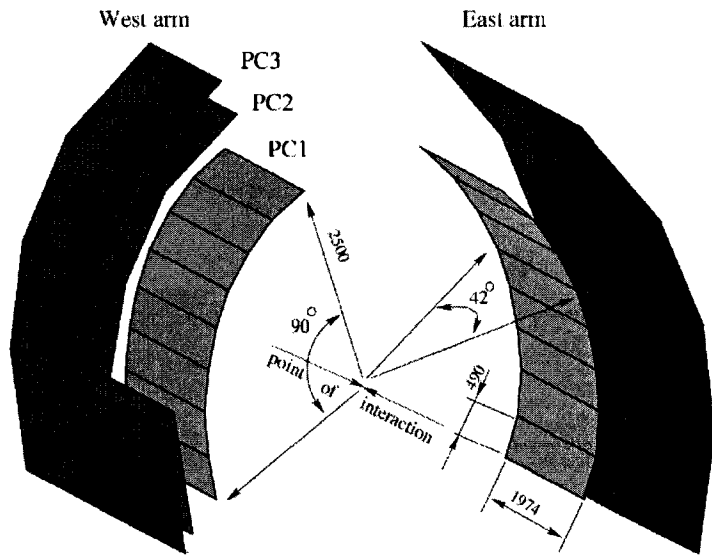


Figure 3.13: The PHENIX pad chambers. Taken from Sasha Milov's PHENIX Focus talk given on 01/04/05 "How to Measure Multiplicity and Transverse Energy?"

ferent roles. PC1 provides tracks with a zed coordinate, PC2 is used for track matching, and PC3 performs matching and is used as a veto for the EMC subsystem. Since the role of the pad chambers in tracking is outshined by the drift chambers, I will merely point you to the first PHENIX paper [36] that was published where the analysis was focused on their use.

3.2.3 Particle Identification (PID)

Ring Imaging Cherenkov Detector (RICH)

Particle identification for electrons is mostly done with the Ring Imaging Cherenkov Detector (RICH). Particles travel through the gas of the detector and when their velocity exceeds the speed of light in the gas, they emit

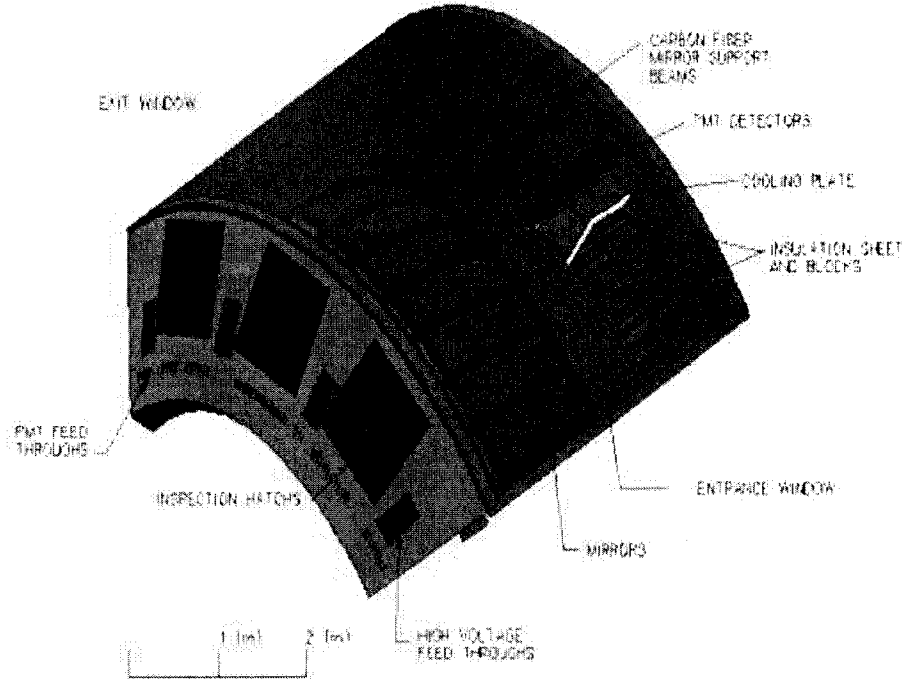


Figure 3.14: The RICH subsystem from [51].

Cherenkov radiation in a cone with a characteristic shape. That light is reflected with focusing mirrors into photo-multiplier tubes and the signal is read out. Fig. 3.14 shows a schematic.

We primarily use the RICH as a threshold counter. Pions below 4.8 GeV do not emit light. If the RICH fires below that energy, we can be almost certain, the particle was an electron. This is the basis for our electron identification.

We also attempt to differentiate hadrons from electrons based on the ring of photons that we catch using the RICH. As an example, the ring of photons that is emitted from a pion is diffuse in comparison to those emitted from an electron. We quantify this diffuseness in a number and during the production

phase, that number gets included in the final data file. It then gets used later during the analysis for electron ID as a variable that we can make cuts on.

Electro-magnetic Calorimetry (EMC)

The electromagnetic calorimeter (EMC) follows a design, commonly used in particle physics detectors. Electrons and photons pass into and interact electro-magnetically with the detector. Primarily they undergo bremsstrahlung and pair production that result in electro-magnetic showers within the calorimeter. Hadrons usually act as minimum ionizing particles known as MIPS. MIPS deposit only a small fraction of their total energy passing in one side and then out the other. Electrons and photons on the other hand, usually never make it all the way through the EMC.

Eight sectors are arranged at mid-rapidity around the interaction region at a distance of approximately 5 meters. Six sectors are based on lead scintillation (PbSc) and the last two are based upon lead glass (PbGl). This subsystem is divided into many hundreds of towers which are further subdivided into cells. Fig. 3.15 is a photo of two sectors of the EMC during the early stages of installation ¹³

The EMC delivers position, energy loss, and time-of-flight information on incoming particles for analysis. For the analysis at hand, the EMC is used for particle identification that takes two forms; energy over momentum ($\frac{E}{p}$) and track matching cuts.

The $\frac{E}{p}$ cuts are very intuitive and simple. For massless particles, $E^2 - p^2 = 0$ and see that $\frac{E}{p} = 1$. This is a requirement that we can lay down on

¹³taken by Yuji Goto taken on 9/17/98.

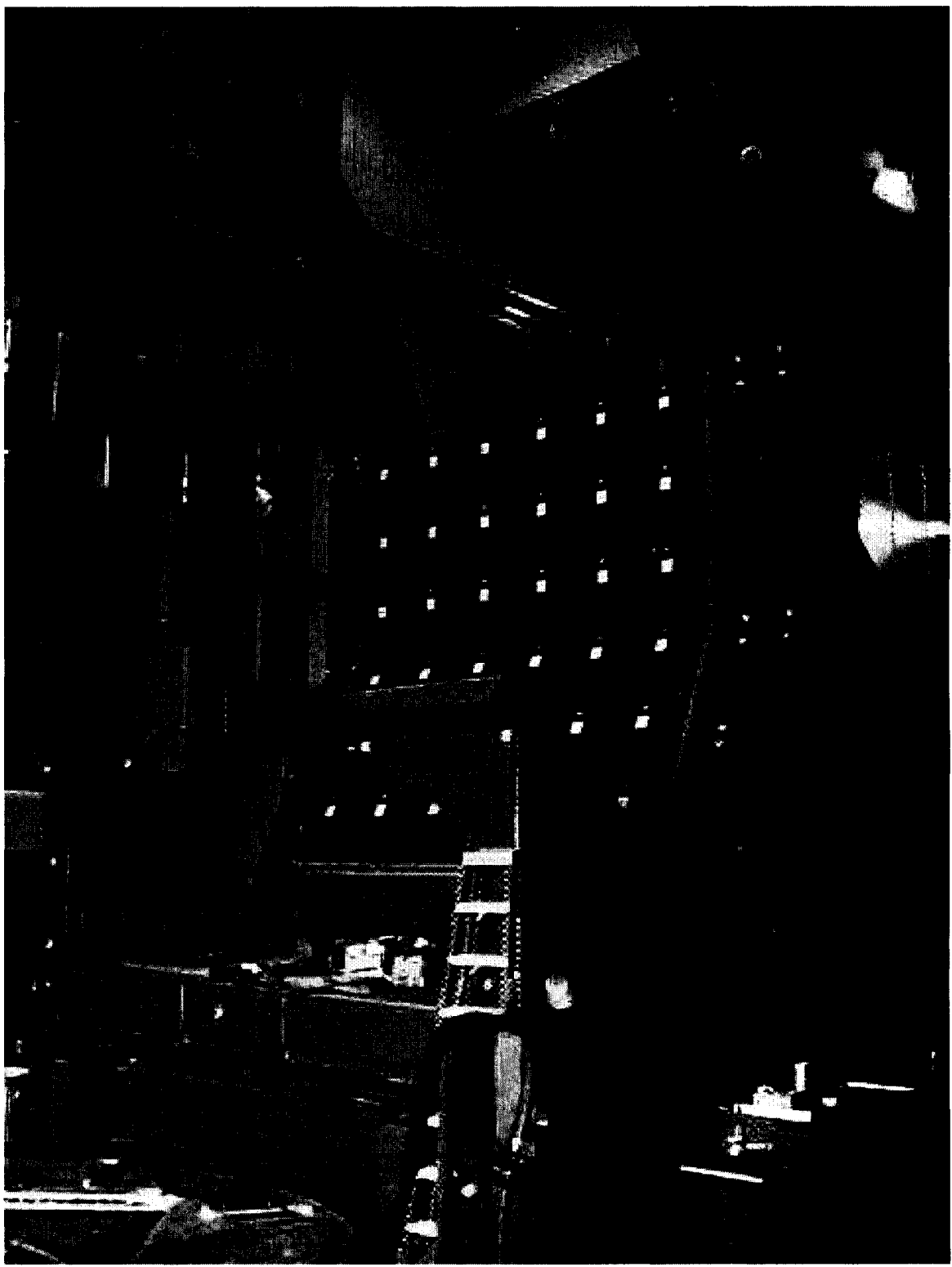


Figure 3.15: photo of two sectors of the EMC during the early stages of installation taken by Yuji Goto on 9/17/98.

our candidate electrons since they are highly relativistic and can be taken as massless for our analysis.

3.3 Track-Matching

Track matching is carried out as follows: After the tracks have been reconstructed, they are extended out onto the calorimetry. Track matching here means that the location pointed to by the tracks must correspond to a shower position in the calorimeter. See Fig. 3.16 for an illustration. By cutting on the resulting $\Delta\phi$ and Δz distributions, we can eliminate falsely reconstructed tracks. For this analysis, the requirement for track matching will be discussed again in Sec. 5.3.2.

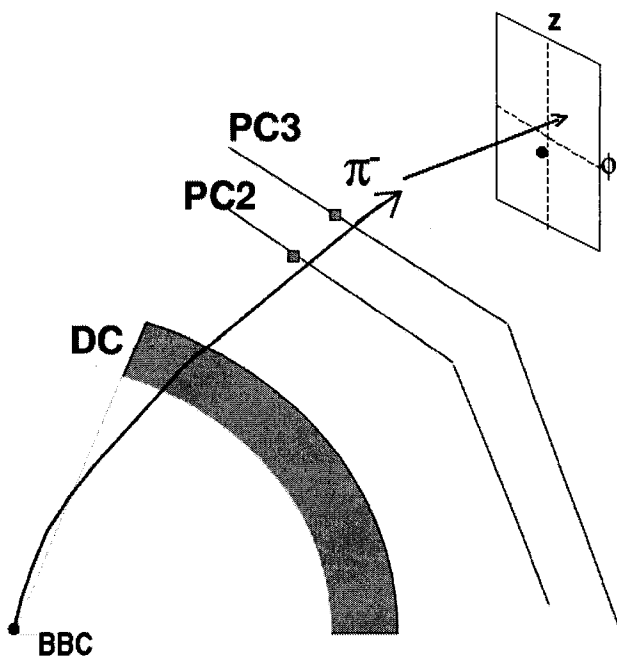


Figure 3.16: Diagram of the track-matching procedure used in this analysis for particle identification. Reconstructed tracks point to a location on the EMC. This location is then compared to the location of a shower and the small deviations are used as the basis for an analysis cut [52].

Chapter 4

The Nature of the Nuclear Modification

Factor: R_{AA}

It is the goal of this analysis to measure what is known as a Nuclear Modification Factor. If a medium was created during the collision, then we should be able to compare the Au + Au spectra to the analogue in a collision where we think no medium was created (p + p) and see the difference. Usually we do this through ratios of various spectra. As we see suppression and enhancements in the gluon and parton distribution functions, we expect to see these types of features in the spectra of the measured particles themselves.

By taking ratios of p_T spectra from Au+Au and p+p collisions, we can see suppressions or enhancements. The resulting ratio is known as the Nuclear Modification Factor, or R_{AA} defined as,

$$R_{AA} = \frac{\left(\frac{1}{2\pi p_T} \frac{d^2 N}{dp_T dy}\right)_{Au+Au}}{T_{ab} \left(\frac{1}{2\pi p_T} \frac{d^2 \sigma}{dp_T dy}\right)_{p+p}} \quad (4.1)$$

If there was no medium, then we can expect all the same stuff to be happening in the gold on gold collisions that was in the proton-proton colisions;

there's just more of it. That would indicate the normalizations of the spectra would be different, but the shapes would be the same. Any ratio in this case would result in a constant function. That's not very exciting by most standards. The T_{ab} factor in the denominator is a scale factor needed to account for the different collision geometries. This constant is called the thickness function and is discussed below.

4.0.1 Glauber Model of Nuclear Collisions

On some level, we hope to understand the interactions between two nuclei starting from the interactions of the particles that make it up. If we could do so at the level of quarks or gluons, we'd be done already. This is not so. However, we do understand the interactions of nucleons at a basic level. The nucleon-nucleon inelastic cross section is known fairly well so it is reasonable to start there.

The Glauber Model of nucleus-nucleus interactions [53] does just that. Using the measured inelastic cross section as an input, it calculates the probability, based on geometry only, of an interaction between nucleons as the collision takes place. Every nucleon is assumed to follow a straight line path and the nuclei are given the standard Woods-Saxon density distribution. The calculation is based on integrals of nucleon densities called thickness functions which depend on impact parameters. The basic thickness function is defined as

$$T_A(b) = \int \rho(z, b) dz, \quad (4.2)$$

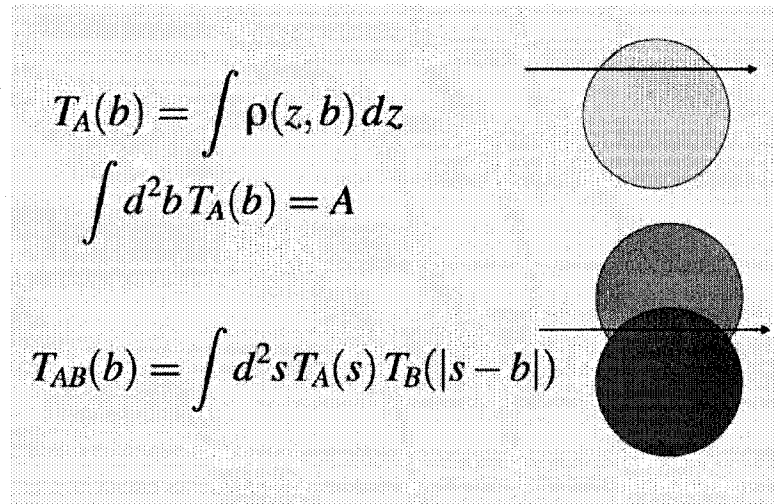


Figure 4.1: Definitions of the thickness functions and nuclear overlap used as a basis for the Glauber model. (shown at “PHENIX Focus 2005 - How to Measure Centrality.” by David Morrison, PHENIX collaboration, 2005-07-01)

where ρ is a probability density dependant on a z-coordinate and an impact parameter b . The normalization of ρ is given by,

$$A = \int T_A(b) d^2 b. \quad (4.3)$$

The nuclear overlap integral is given by

$$T_{AB}(b) = \int T_A(s) T_B(s - b) d^2 s. \quad (4.4)$$

Fig. 4.1 illustrates the integrals that are used in these definitions. Geometrically, the notion of nuclear overlap is pretty intuitive.

Once we've got the thickness functions we can start to calculate other physics observables. Examples are the total cross-section,

$$\sigma_{AB} = \int 1 - (1 - \sigma_{NN} T_{AB}(b))^{AB} d^2 b \quad (4.5)$$

the number of participants,

$$N_{part} = A \int (1 - (1 - \sigma_{NN} T_B(r_s - r_b))^B) T_A(r_s) d^2 s \quad (4.6)$$

and the number of binary collisions,

$$\sigma_{AB} = AB \int \sigma_{NN} T_A(r_s) T_B(r_s - r_b) d^2 b. \quad (4.7)$$

The cross-section and number of binary collisions are related by

$$T_{AB} = \frac{N_{bin}}{\sigma_{pp}^{incl.}} \quad (4.8)$$

Each of the expressions above is true only for the Eikonal or Optical approximation where it is assumed that all scatterings are independent from each other. That is to say, the potential describing the system does not vary over length scales comparable to the wavelength of the nucleons.

We assume the baryons interact with each other in the same way for the entire process. That means the input cross-section stays the same even though we know excited states of nucleons are created and both diffractive and elastic effects are taking place. All in all, the Glauber model is an approximation. Perhaps it's not the best, but it allows the calculation of quantities we can measure. Once we have the probabilities calculated, we can find any average quantity we need. The most important for us will be N_{coll} , the average number of binary collisions that took place. Many of our results will be stated in terms

of N_{coll} later. We also talk about N_{part} , the number of participants when considering the Nuclear Modification Factors for hadrons.

Chapter 5

The Measurement

5.1 Preliminaries

5.1.1 A Rough Outline of Procedure

The analysis procedure is as follows:

1. Fully corrected inclusive single-electron spectra are determined for minimum bias Au + Au collisions and for a variety of centrality classes. The fiducial cuts, electron ID cuts, and the corrections for acceptance and efficiency are performed.
2. The photonic background is subtracted via electron cocktails that are calculated individually for all centrality classes. These cocktails are discussed in detail below.
3. The resulting electron spectra from non-photonic sources are presented and compared with the published results from a complementary analysis [68].

4. The nuclear modification factors R_{AA} , are calculated as function of p_T for all centrality classes using the p + p result from [14] as a reference.

This analysis complements a previous one [68] that used what is now known as the Converter method for background subtraction.

The strengths of the cocktail method are listed here:

- The systematic errors at high p_T (> 2 GeV) are much smaller than those of the converter by roughly an order of magnitude. (The ratio of background to signal is about $\frac{1}{10}$ at high p_T).
- The statistical sample is larger by a factor of 4.5.

The strengths of the converter method are

- The systematic errors at low p_T are much smaller than those of the cocktail method.¹

It is good to think about the electron spectrum's normalization and shape separately when comparing the merits of each method. These two observables can be brought into rough correspondence with our two physics concerns; binary scaling of the total charm yield and energy loss of heavy quarks in a nuclear medium (the main result of this analysis).

The converter method is a very good counting measurement because it has small systematic errors at low p_T . About 70% of the electrons in the inclusive spectrum are located below 1 GeV. Thus the accurate measurement

¹The converter actually *measures* the background where the signal to background ratio is small.

of the converter analysis at low p_T will translate into an accurate count of the electrons or electron yield. This is crucial for establishing the binary scaling of charm production.

The current cocktail analysis provides a good measurement of the spectral shape out into the high p_T region and so we think of it as an accurate shape measurement. If the shape is determined accurately, we can then compare that shape to the spectral shape in the p + p and see if there are changes.

5.1.2 Conventions

Throughout this thesis there are a few terms that come up repeatedly. They are defined here to avoid confusion.

- Electron

Electrons and positrons are considered together, unless we explicitly say so, *i.e.* when we refer to a spectrum of electrons, this refers a spectrum that was created using a sample that contained both electrons and positrons together *i.e.* $(e^+ + e^-)/2$. As a consistency check, we carried out this entire analysis treating each charge separately and the results are the same up to small changes in the low p_T region below 0.4 GeV.

- Tracks

A track refers to a particle which is currently considered a candidate electron. This specifies a reconstructed track that has passed all the electron cuts used in the analysis.

- Signalized

The matching cuts in azimuth and *zed* as well as the energy-momentum matching cut are *calibrated* in terms of standard deviations in order to avoid the problem that the corresponding resolutions are functions of p_T . This is a standard technique for PHENIX and we use the term *sigmalized* for these variables.

- Rungroup

The entire data set is broken down into subgroups for this analysis and those subsets are referred to as rungroups.

5.1.3 Location of Analysis Code

All the code for the present analysis has been checked into the PHENIX CVS repository under /offline/analysis/Electron_RAA. The file named *documentation* describes all associated files, functions, building, compilation, and operations.

5.2 Data Set

PHENIX data is located on the RHIC Computing Facility (RCF) and is stored in the collaborations nano-DST (nDST) format. Measurements made by the detector are broken down into data runs. Each run spans many files on disk, known as file segments, and each file segment contains a nano-DST. Nano-DSTs are essentially wrappers for C++ structures that can be manipulated by writing macros and compiled code for use in the ROOT data analysis framework.

All lists of data file segments and Monte-Carlo files used in the analysis are contained in /offline/analysis/Electron_RAA/lists and are detailed in the documentation (see above) as well.

The starting list of file segments used in this analysis is checked into CVS under, /offline/analysis/Electron_RAA/lists/ELECTRON_ANALYSIS_FILE-LIST.TXT. This was the approved list of Electron Working Group nanoDSTs (EWGnDST) which are used as a starting point for all electron analyses using the Au-Au Run-2 data set. There are 30 million events available to this analysis in the EWGnDSTs.

These nDSTs are a just subset of the total data available to PHENIX stored in the Central nDSTs. Every EWGnDST in that list has already had the following cuts applied (when the EWGnDST was created);

- Event – zed coordinate of the event vertex: $|vtx| < 30.0$ cm,
- Track – transverse momentum: $0.150 < p_T < 20.0$ GeV,
- Track – number of hits in the primary layers (X1 and X2 – see Sec. 3.2.2) of the drift chamber: $nx1 \geq 2$ AND $nx2 \geq 2$ for the drift chamber,
- Number of hits in the photomultiplier (PMT) tubes in the projected ring area within the RICH : $n0 \geq 2$ OR $sn0 \geq 2$ for the number of PMT's, and
- Track – signalized track-matching: ($emcsdze < 5\sigma$ AND $emcsdphie < 5\sigma$) OR ($pc3dz < 5\sigma$ AND $pc3d\phi < 5\sigma$). (see Sec. 3.2.3.)

Each of the quantities used in the cuts above is described in detail in Sec.

5.3. Only minimum bias events were analyzed. To implement this we required the *isminbias* field in the nanoDST to be true for that event.

5.2.1 Run Selection

The full list of all runs was subdivided into two groups referred to as rungroups in the following. The runs from 28623 to 29136 make up the set used in [68]. The set of non-converter runs (those runs used in [68] that did not have the brass converter installed) span the range 29136 to 30000. We take our first smaller group of runs to be the original set of previously analyzed non-converter runs [68]. We call this rungroup the Quark Matter (QM) rungroup from now on.² It was checked very carefully for [68] that the run-by-run variations in the QM rungroup are minimal, and the Monte-Carlo simulation was tuned to the detector performance in this rungroup. Consequently, the analysis of this rungroup is the anchor of the current analysis. Everything left over (excluding the set of converter runs) forms the second rungroup, called the everything else (EE) rungroup. A summary is contained in Table 5.1.

The selection of data runs that were used for the analysis is based on an examination of the number of tracks or electron candidates, per event in a given run. As a cross check, we examine the same quantity for the various centrality classes.

We consider the number of tracks per event in order to estimate the stability of the apparatus. The basic idea is to plot the average number of tracks per event as a function of run number. Deviations from the mean values should

²This naming convention is arbitrary and started because the converter analysis was shown initially at Quark Matter 2002.

Table 5.1: Definitions of Rungroups

Run Group	Range
Full Data Set	$28163 < Run < 33694$
PPG035 Converter	$28623 < Run < 29136$
PPG035 Non-Converter	$29136 < Run < 30000$
QM	$29136 < Run < 30000$
EE	$28163 < Run < 28623$ $30000 < Run < 33694$

indicate problematic runs, which have to be removed from the run list. For example, a hot tower in the calorimeter can cause the number of tracks per event to rise to an unacceptable level and the run must be removed from the sample. Dead areas may lead to reductions.

Technically, the number of tracks per event for each run axis and is binned into a histogram and that histogram is fitted with a Gaussian. The mean and standard deviation for the tracks per event is then determined. Any run which deviates by more than 2 sigmas from the mean of its run group was discarded. The total number of events thrown out by doing this is negligible (less than 2%).

Corresponding distributions were generated in the various centrality classes as a cross check.

Tracks per event are plotted in Figs 5.1. The corresponding projections for the EE rungroup are in Fig. 5.2. The projections for the QM rungroup are similar in nature and provide no extra information. The list of accepted runs is stored in CVS at the location specified in Sec. 5.2.

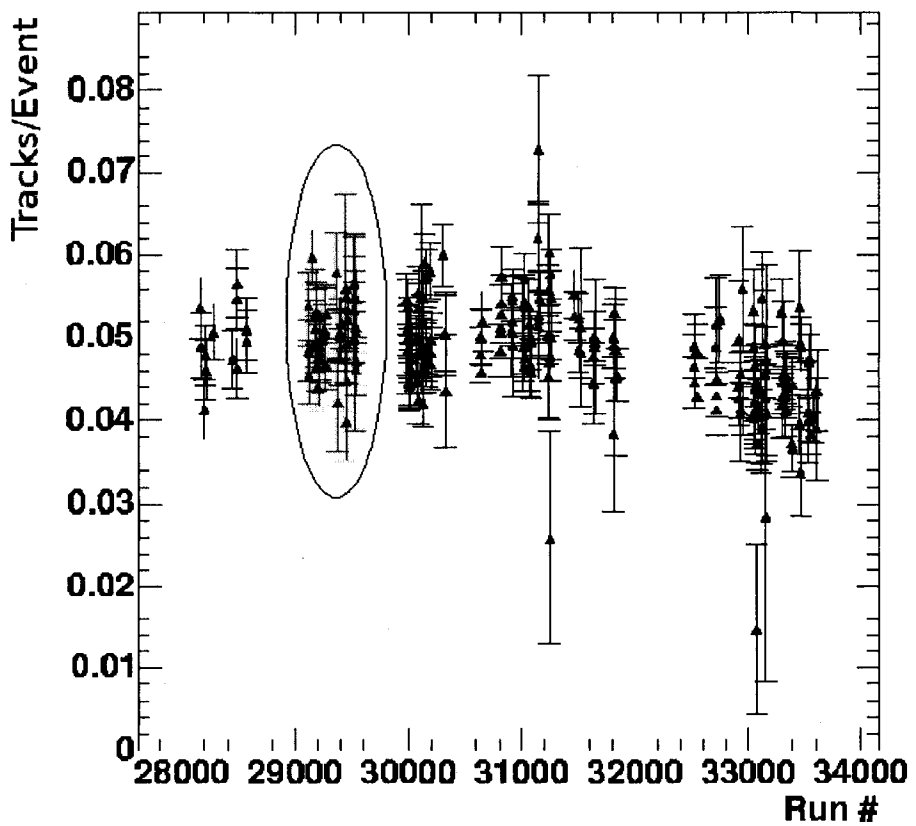


Figure 5.1: Tracks per event for Minimum Bias collisions. The points within the ellipse are the Quark Matter (QM) rungroup. Everything outside the ellipse is the Everything Else (EE) rungroup.

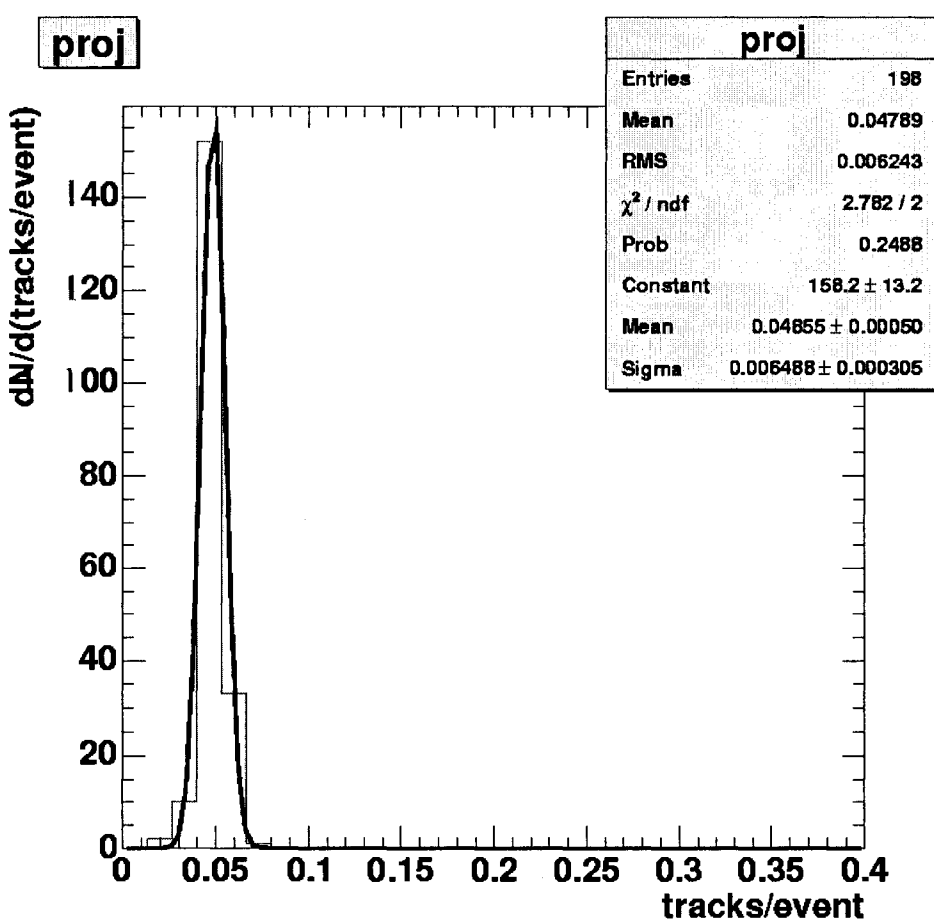


Figure 5.2: Gaussian fit to projection of tracks per event for minimum bias in the EE rungroup.

5.2.2 Centrality

Shown in Fig. 5.3 are the two centrality distributions created from the data, *i.e.* plots of $dN/d(\text{centclock})$ for the two rungroups chosen for this analysis (see below).

The two outstanding features of Fig. 5.3 are the fluctuations about a constant value for $\text{centbyclock} < 85$ and the clear dropoff in the counts at $\text{centbyclock} > 85$. The fluctuations are caused by the small binning used in the definition of centbyclock . They are a form of sampling error. The large binning of the centrality classes used here protect the measurement from these fluctuations. The nature of the dropoff in the distributions above 85 is unclear, but points to a problem in the centrality determination for peripheral collisions. To avoid this problem, we use 60 - 80 % as the most peripheral centrality class in this analysis. For completeness and to allow for comparisons, we perform the analysis in the commonly used 60 - 92 % centrality class as well.

5.3 Electron Identification

5.3.1 Cut Variables

Cuts were made on the following quantities stored as fields in the EWGnDSTs or derivable from them, in which case the functional dependence of the quantity is shown: (descriptions were taken from PHENIX nanoDST documentation from the internal page).

ecore Energy deposited in the calorimeter cluster associated with the track.

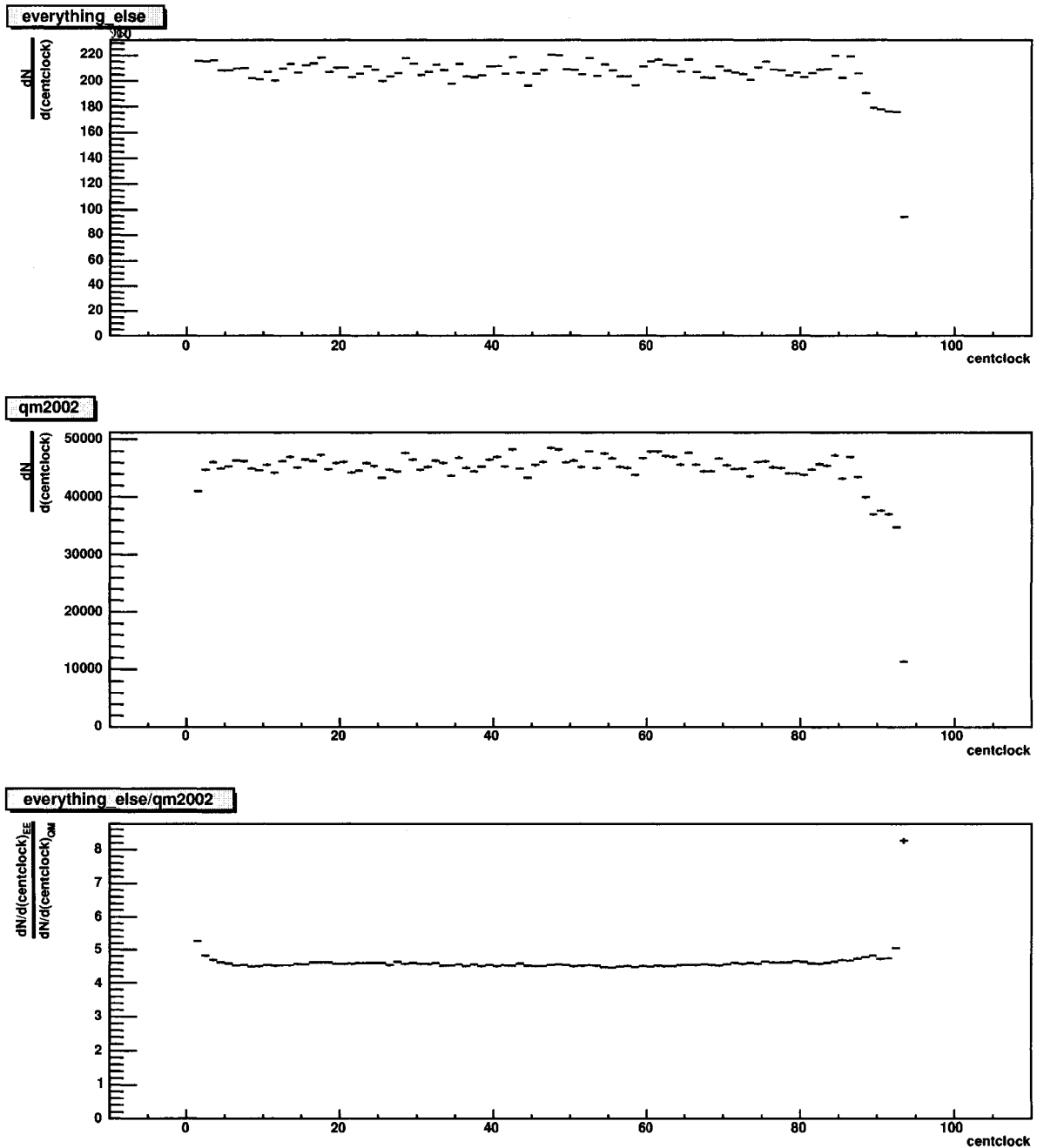


Figure 5.3: Distributions of centrality(centclock) for the two chosen rungroups (see below).

mom Momentum of the track.

n0 A count of the number of PhotoMultiplier (PMT) hits in the projected RICH ring area.

n3 Also a count of the number of PMT hits that arrived within a specific range of time relative to the collision time determined by pathlength and the assumption that electrons are moving with the speed of light.

disp This variable measures the displacement of the ring center with respect to the track projection positon in the RICH PMT array.

npe0 This is the number of photo-electrons (i.e. summed pulse height) summed over the normally sized ring area.

chi2 This is a “unitful” chi squared associated with the fit to the ring performed during reconstruction in units of cm^2 . It is not calcluated per degree of freedom. Typically cuts are placed on $\text{chi2}/\text{npe0}$ as a semi-normalized $\text{chi2}/\text{dof}$. A commonly used cut is $\text{chi2}/\text{npe0} < 10$.

depemc(ecore, mom, sector) The sigmalized distribution of $(e-p)/p$. This is a derived quantity that is used as a parameterization. For a given track momentum, energy, and EMC sector, *depemc* quantifies how many standard deviations the energy and momentum differ from each other. The parameterization is given explicitly in B.1.

emcsdze Used in track-matching. Each track is projected onto the EMC. *emcdze* is defined as a sigmalized deviation between the projection of

the track onto the inside of the EMC and the location of the EMC cluster associated with that track.

emcsd ϕ The same as emcdze, but in the azimuthial, ϕ , direction.

5.3.2 Specification of Identification Cuts

This analysis uses tracks reconstructed in the East-Arm spectrometer only! There are significant differences between the active area of the East and West arms of the detector. Most importantly, the active area of the West arm was *changing* as a function of run number. This makes it very difficult to use since the corrections would need to be known as a function of time. For this reason, we decided to restrict our attention to the East arm.

In addition to the implicit cuts applied in the creation of the EWGnDSTs, the following requirements were made for selecting candidate tracks:

- $n0 \geq 3$,
- $n3 \geq 1$,
- $disp < 5$,
- $chi2/n0pe < 10$,
- $depemc(ecore, mom, sector) > -2$, and
- $\sqrt{dze^2 + dphie^2} < 2\sigma$.

The first four cuts are associated with the RICH. These cuts are commonly employed for electron identification. The n0 cut has the largest impact. The

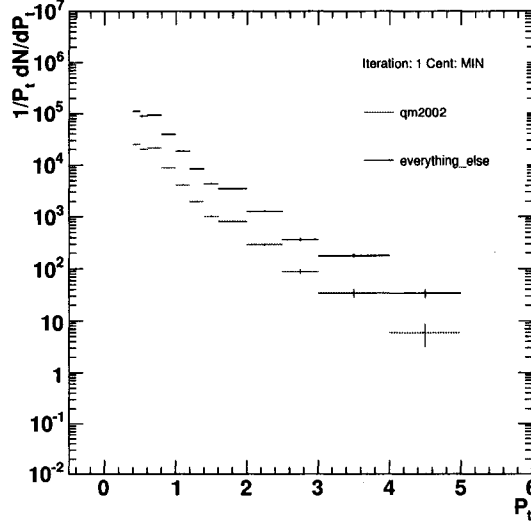


Figure 5.4: Overlay of uncorrected inclusive electrons for Minimum bias.

fifth cut is essentially a cut on the ratio, $\frac{E}{p}$ that is characteristic for relativistic electrons. Finally, we require a geometrical matching of the track projection and the associated cluster in the EMC. This $\frac{E}{p}$ cut gets us an extra factor of 10 to 100 in hadronic rejection power depending on the p_T of the particles under consideration (See Sec. 5.5 for more information.).

In addition, we apply fiducial cuts in order to ensure that the active area in the experiment is compatible with the simulation. The cuts chosen are presented later in Sec. 5.6.

5.4 Raw Inclusive Spectra

The resulting uncorrected inclusive electron $\frac{1}{p_T} \frac{dN}{dp_T}$ spectra for both run-groups are shown in Fig. 5.4.

It is of paramount importance for this analysis to investigate the ratios of the raw p_T spectra obtained from both rungroups as shown in Figs. 5.5. Since the Monte Carlo was tuned for the QM rungroup, we need to find a strategy for the acceptance and efficiency correction of the EE rungroup. Our approach is to show that the raw spectra measured in both rungroups exhibit the same shape, which would indicate the following; any variation in active area in the EE rungroup (compared to the QM rungroup) will only affect the absolute normalization of the spectra, but will not modify the spectral shape. We can then apply the same acceptance and efficiency correction (obtained for the QM rungroup) also for the EE rungroup and rescale it with an additional p_T independent correction factor to accomodate for a potential difference in active area between the two rungroups.

The ratio of raw spectra from the two rungroups are shown in Fig. 5.5 together with a fit to a constant. Since the active area does not depend on the centrality of the collision, it is sufficient to examine minimum bias collisions only. Within the statistical uncertainties, the ratios in the centrality classes are consistent with the minimum bias ratio, and, most importantly, the ratios do not show any significant p_T dependence. In particular, at low p_T , where tracks are curved and a difference in the active area could lead to a p_T dependent difference in the acceptance, the spectra measured in the two rungroups exhibit the same shape with very high precision. (We estimate the associated sys. uncertainty conservatively as 3 %.) At high p_T (above about 2 GeV/c), the tracks are essentially straight and a p_T dependence can be excluded for the acceptance.

We conclude that the p_T spectra exhibit the same shape in both rungroups.

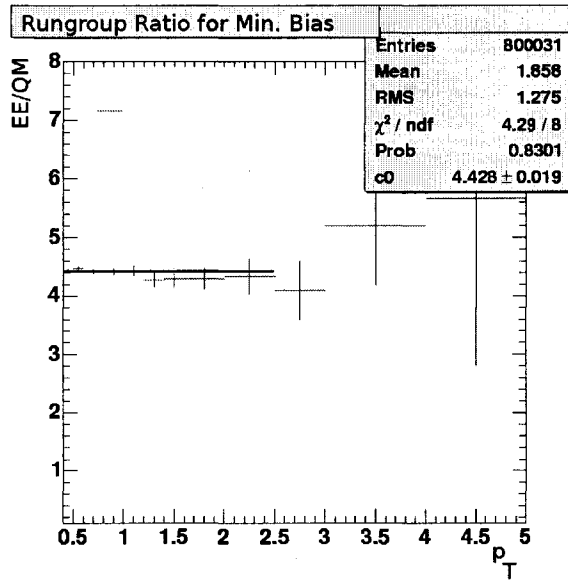


Figure 5.5: Ratio of uncorrected inclusive electron p_T spectra from the QM and EE rungroup for Minimum bias. The thick black line shows the fit to a constant function.

This is a very important statement to make. The method used to create the corrections will rely on this fact because we will bootstrap ourselves from the Monte-Carlo that was tuned to the QM rungroup, to the larger EE rungroup.

5.5 Random hadronic background subtraction

Occasionally, random associations of particles in the different subsystems of the detector are improperly reconstructed as tracks. Specifically, we are concerned with charged hadron tracks that are randomly associated with an additional electron that leaves a signal in the RICH. This is caused by the presence of an electron and pion moving parallel to each other. The spherical mirrors focus the rings of photons on the same set of PMTs. The reconstruction sees this

and mis-identifies the pion resulting in our hadronic background. These tracks form a random background for this measurement and must be removed. They are referred to here as random hadronic background (HB). To determine the spectrum of the HB, we use the flip-and-slide method (see below).

5.5.1 Swapped Variables

Each variable that is used to make cuts has a swapped version that was created using a technique called flip-and-slide.

We take the RICH subsystem and think about it in two sections along the z, the first (outer RICH) portion is that part of the RICH positioned at large magnitudes of z. The outer portion is flipped within the reconstruction software (replaced with its mirror image).

With the RICH in this “swapped” state, we pass over the data and fill fields in the nDSTs again just as before in the normal state. We now apply our cuts to the data but instead used the swapped versions of the variables associated with the RICH. All other cuts remain the same since the random associations are happening with information coming from the RICH. Anything that passes the cuts in this situation is now by definition, a false track that resulted from a random association.

While this works well for the outer RICH, if the same procedure was followed for the inner portion of the RICH, the displacement in the software wouldn’t be enough to eliminate the possibility of these associations. As a solution, we slide the positive zed area of the inner RICH to the negative side and slide the negative zed area to the positive side. The displacements carried

out within the reconstruction are then large enough and the HB can then be identified as before.

The name of the swapped versions are prefixed with the letter s (e.g n0 becomes sn0). To find the HB, we pass over the same sample and apply the same cuts, but now use the swapped versions for the variables associated with the RICH.

The following requirements were made for determination of the HB:

- $sn0 \geq 3$,
- $sn3 \geq 1$,
- $sdisp < 5$,
- $schiz/sn0pe < 10$,
- $depemc(ecore, mom, sector) > -2$, and
- $\sqrt{emcZmatch^2 + emcPhimatch^2} < 2\sigma$.

Applying these cuts, we generate raw HB spectra which are subtracted from the electron candidate spectra presented in the preceding section.

The E/p distributions for Run II p+p collisions are shown in Fig. 5.6. The topmost distribution with the peak at 1.0 represented by the solid line (electronic version: black) represents the minimum bias inclusive spectrum of identified electron candidates. Now we can assume that the main source of unphysical background in the sample is that of the hadrons. Random associations of tracks and rings in the RICH are reconstructed as tracks and these will form our HB.

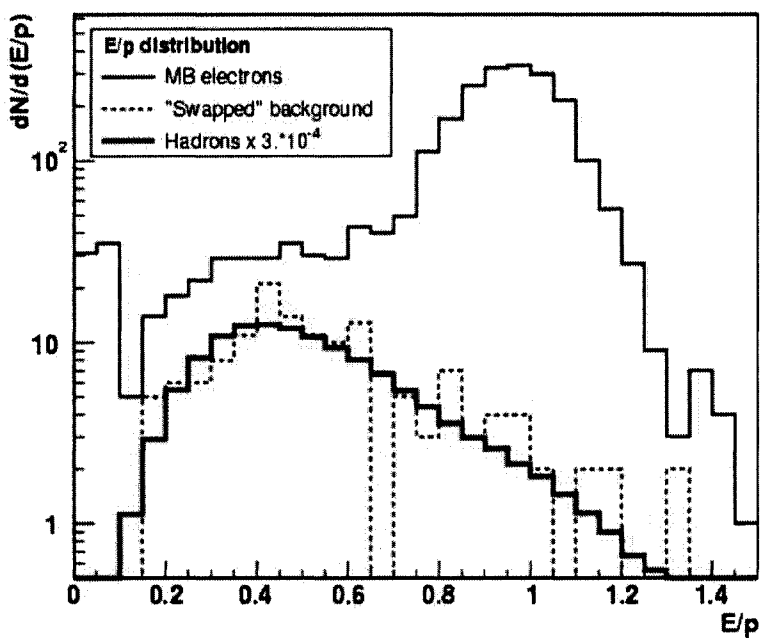


Figure 5.6: E/p distributions for Run II $p+p$ collisions plotted to show the relationship between the hadronic background and swapped distributions used eliminate random associations of tracks with rings in the RICH [13].

By applying the swapped versions of the cuts to the sample the dotted (electronic: blue) distribution is filled. This is known as the swapped distribution. The thick solid lower (electronic: red) distribution is that of the measured PHENIX hadrons scaled down by a factor of 3×10^{-4} . It should be clear that the two histograms have the same shape. This is the argument that says the hadrons are causing this background.

From the overlay, we see the statement above is independent of p_T and the scale factor becomes the probability for the mis-identification of a hadron as an electron, $P(h|e) = 3 \times 10^{-4}$. After this background is subtracted out from the inclusive spectrum, an E/p cut will be applied on top of that to give an extra factor of x100-x1000. The total rejection power results in our ability to reject approximately one mis-identified hadron in 10^6 tracks. Note that these numbers are only to represent the probabilities in the case of collisions of protons on protons and are given only to provide an example of the method. The same statements are known to hold true for collisions of Au + Au from other internal work in PHENIX.

It is important to compare the $\frac{E}{p}$ distributions of electron candidates with that of the HB. Two examples are shown in Fig. 5.7 for Minimum Bias events in different p_T bins. The background level is in general larger for central collisions and tends to drop with increasing p_T . In the worst case of low p_T electrons in central collisions, the background level is on the order of 10-15 %.

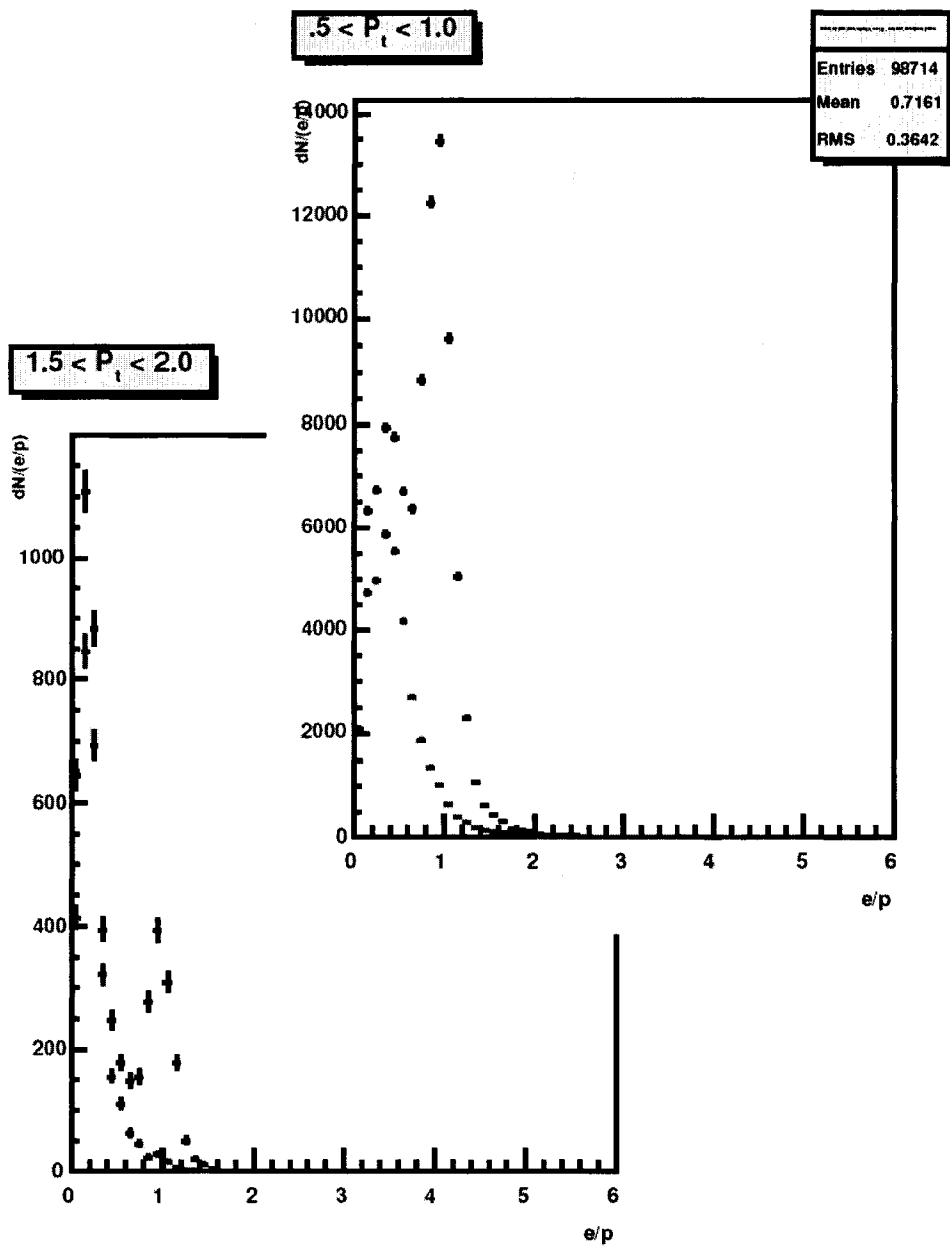


Figure 5.7: Overlays of energy over momentum as function of $\frac{E}{p}$ shown in two p_T -classes for minimum bias. The two panels correspond to different windows of p_T of 0.5 GeV width. The upper right panel is .5 - 1.0 GeV and the lower left is 1.5 - 2.0 GeV .

5.6 Acceptance and Monte-Carlo/Data Comparison

The Monte-Carlo needs to first be compared to the data and checked for reasonable agreement before we can use it for creating correction functions that account for geometric acceptance and the efficiencies associated with the reconstruction. Fiducial cuts are employed to ensure that the active area implemented in the simulation agrees as closely as possible with the actual experiment. Here, we simply use exactly the same fiducial cuts as were defined and justified for [68].

5.6.1 Fiducial Cuts

The list of fiducial cuts is taken from [68]. In the present analysis, there is no need to go back and perform an entirely new study of the detector acceptance. Both the converter and cocktail analyses, are using data taken during the same time period and they are looking at particles that we claim come from the same source. This means the acceptance must be the same for both.

For our purposes, the important point to remember is that the cuts account for differences between the data and the simulation. All fiducial cuts used here are defined separately for north and south subdetectors. In effect, this treats them as separate detectors.

The fiducial cuts in the north are defined by (p_T in GeV/c and ϕ in radians)

$$\frac{\text{charge}}{p_T} > 36.175 - 11.81\phi \quad (5.1)$$

$$\frac{charge}{p_T} < 33.26 - 11.86\phi \quad (5.2)$$

and for the south by

$$\frac{charge}{p_T} > 36.9 - 11.85\phi \quad (5.3)$$

$$\frac{charge}{p_T} < 33.357 - 11.809\phi \quad (5.4)$$

In addition, we exclude tracks in the first sector of the EMC (lead glass) with $p_T < 0.5$ GeV because the simulation doesn't agree well with the data there.

5.6.2 Acceptance Distributions

The standard α vs. Φ distributions both from the data (left panel) and from simulation (right panel) are shown in Fig. 5.8 where α represents the inclination of the track with respect to an infinite momentum track. Hence, p_T is roughly proportional to $1/\alpha$. The fiducial cuts listed above are applied. Fig. 5.9 shows the ratio of the two distributions. The same is shown for the north and south subdetector separately in Figs. 5.10 - 5.13. With the fiducial cuts applied the acceptance for data and the simulation are in agreement.

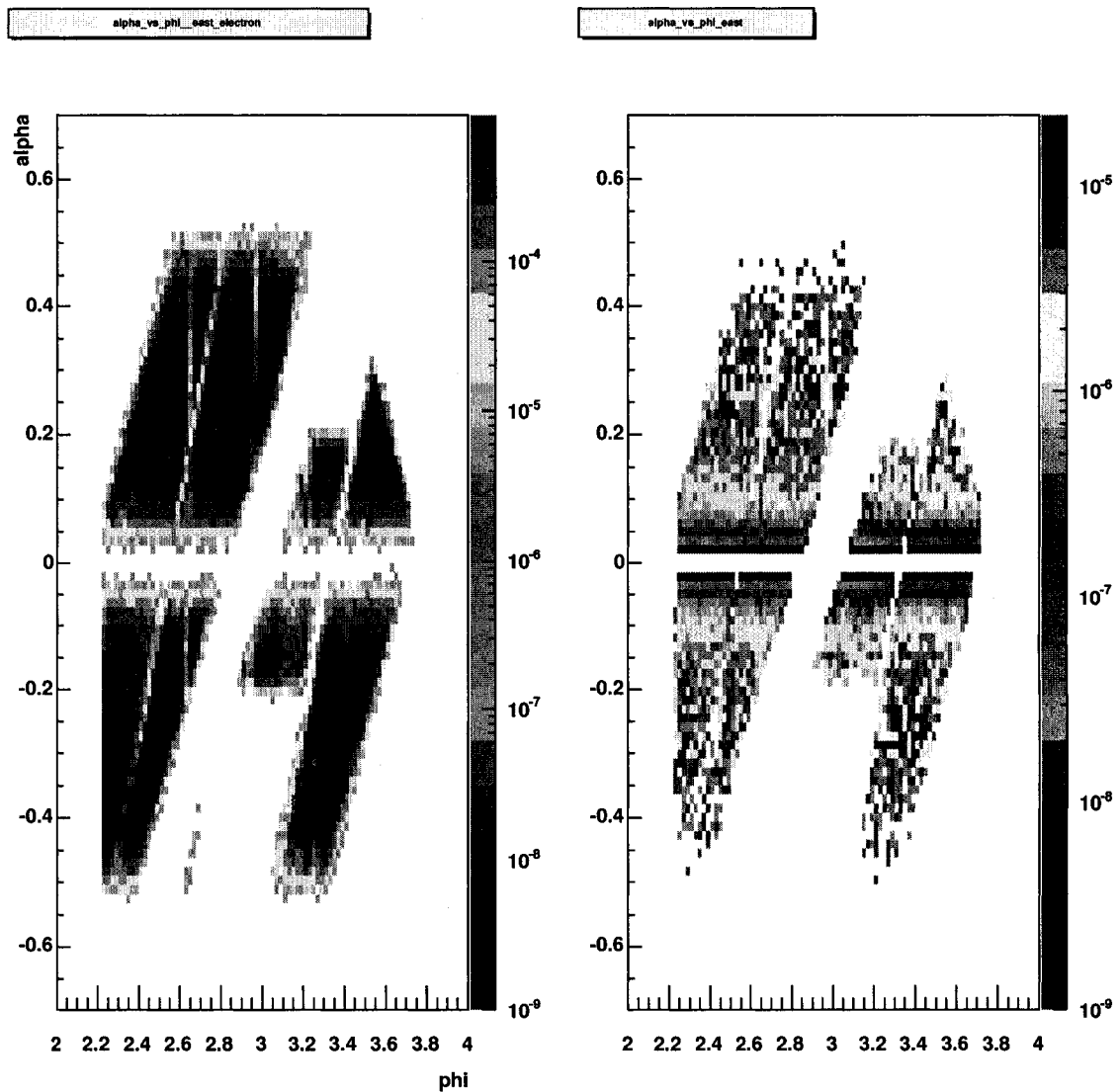


Figure 5.8: α vs. ϕ distributions for data (left) and MC (right).

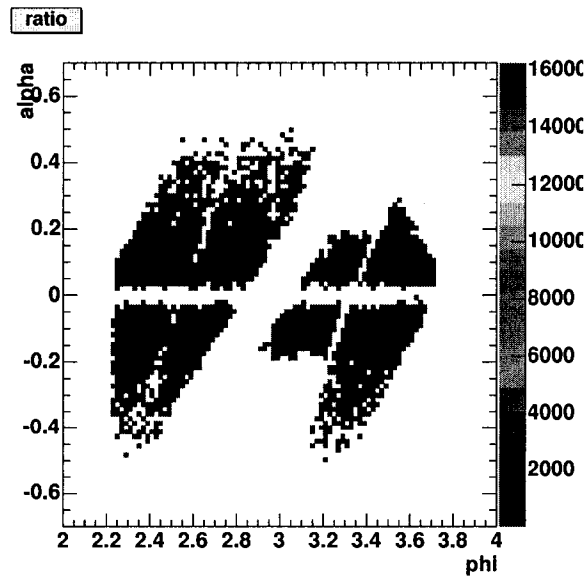


Figure 5.9: Ratio of α vs. ϕ distributions shown in 5.8.

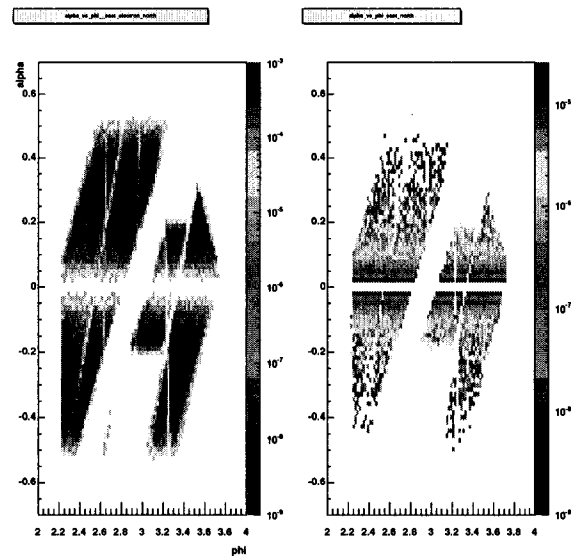


Figure 5.10: α vs. ϕ distributions for data (left) and MC (right) in the north detector.

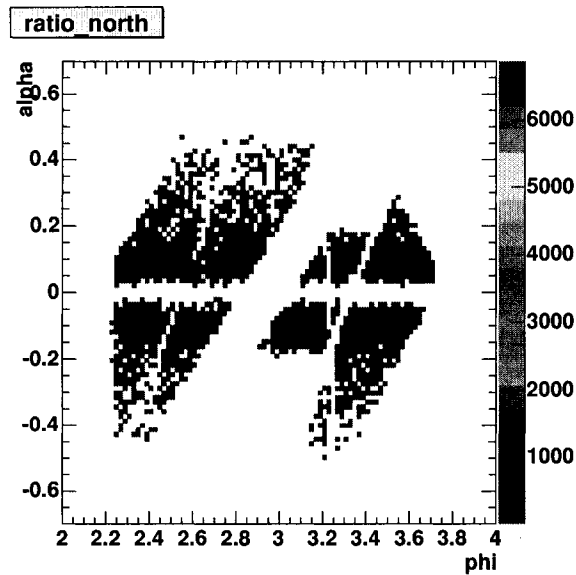


Figure 5.11: Ratio of α vs. ϕ distributions shown in 5.10.

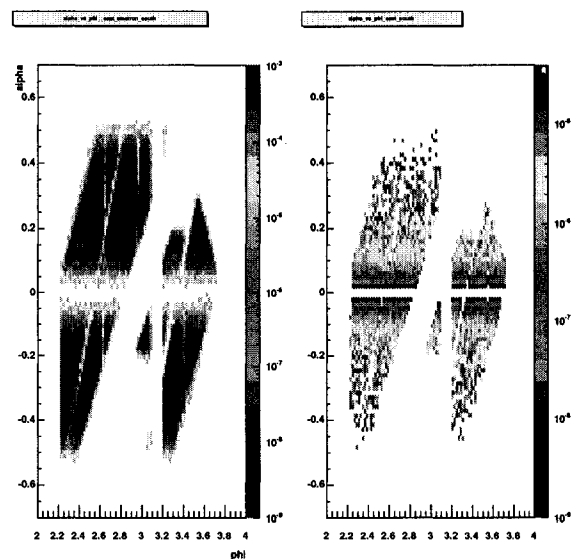


Figure 5.12: α vs. ϕ distributions for data (left) and MC (right) in the south detector.

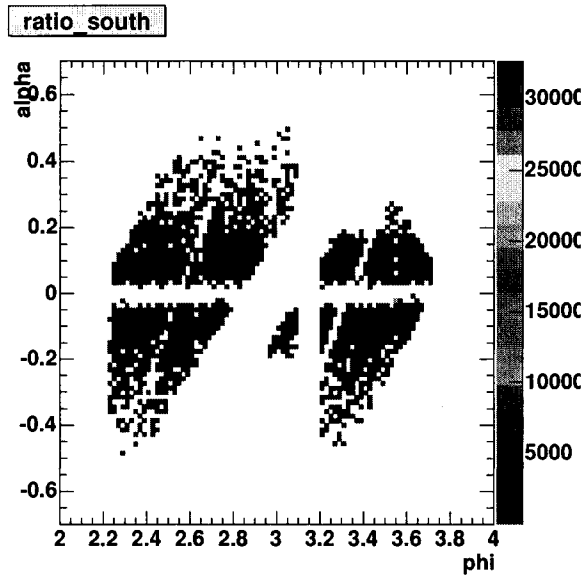


Figure 5.13: Ratio of α vs. ϕ distributions shown in 5.12.

5.6.3 Comparison of Electron ID Variables In Data And Simulation

The simulation must describe the data accurately in order to calculate the corrections for the detector acceptance and general reconstruction efficiencies. In particular, the signalized variables are parametrized as a function of p_T , and the parametrization must be accurate. To check this we overlay the distributions of data and simulation for $dphie$, dze , and dep contained in the simulation nDSTs and the corresponding distributions from the data in Figs. 5.14 - 5.16 in various p_T bins. Reasonable agreement is observed for each.

The distributions from data and simulation are fit with Gaussians and the extracted mean values and sigmas are shown in Figs. 5.17- 5.22. All points are plotted at the center of their p_T -class. As expected the mean values are consistent with zero and the standard deviations are about one for all cases.

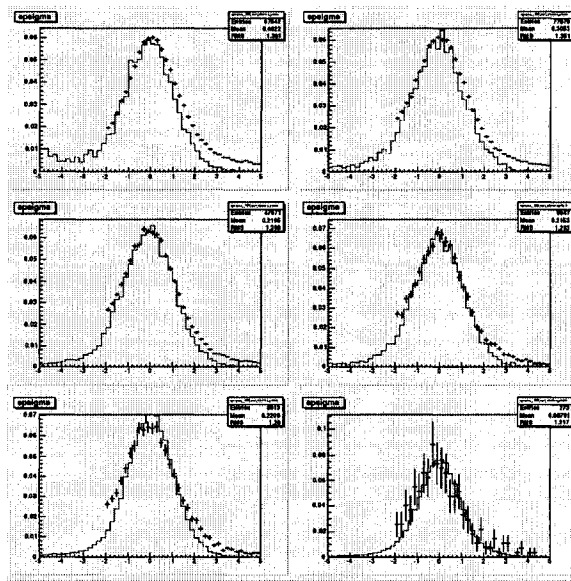


Figure 5.14: Overlays of signalized energy over momentum variable as function of p_T for data and simulation in p_T classes.

We conclude that data and simulation are very similar in terms of electron identification variables.

5.7 Corrections

5.7.1 General Description

The correction for geometrical acceptance and reconstruction efficiency as function of p_T is calculated in the following way:

- 10^8 electrons and positrons with flat distributions in p_T (0.0-6.0 GeV), $y(-.5 - .5 \text{ GeV})$, $\phi(0.0 - 2\pi)$, and $z_{vtx}(-40.0 - 40.0 \text{ cm})$, are generated using a Monte-Carlo event generator called EXODUS.

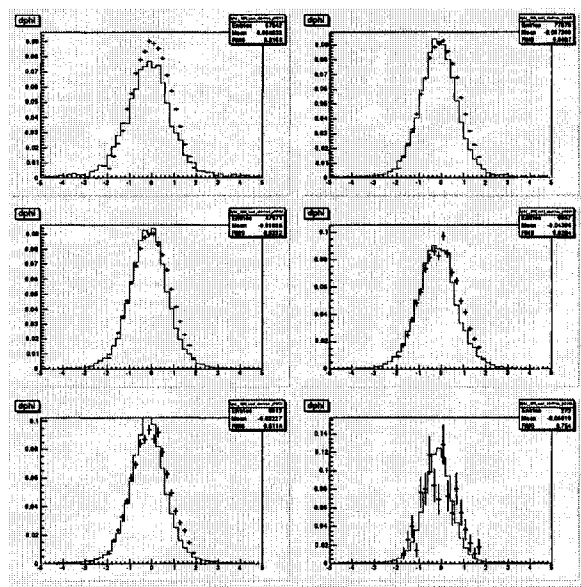


Figure 5.15: Overlays of signalized phi variable as function of p_T for data and simulation in p_T classes.

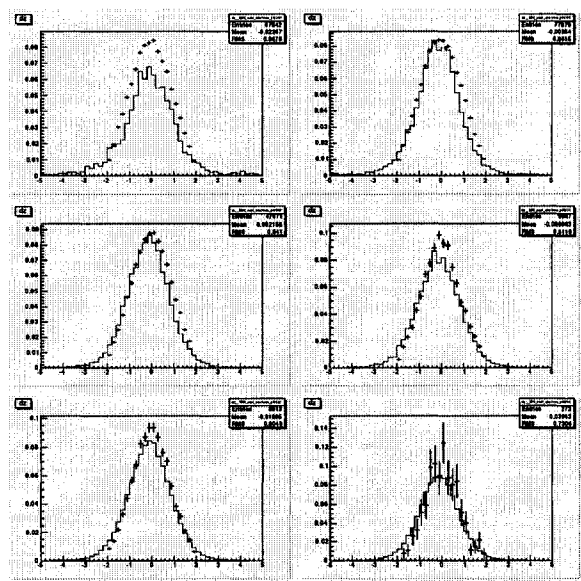


Figure 5.16: Overlays of signalized dz variable as function of p_T for data and simulation in p_T classes.

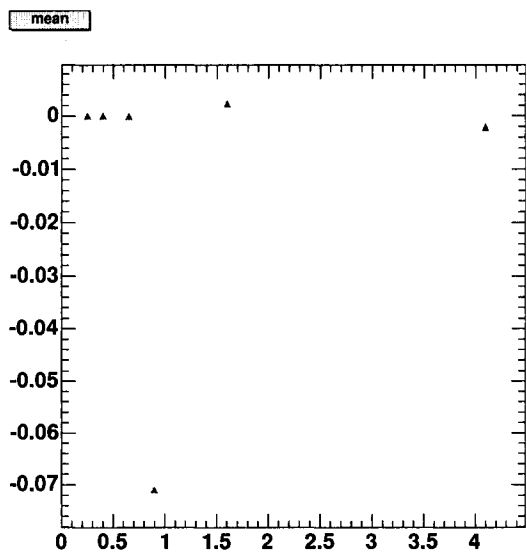


Figure 5.17: mean of gaussian fits to signalized energy over momentum variable as function of p_T .

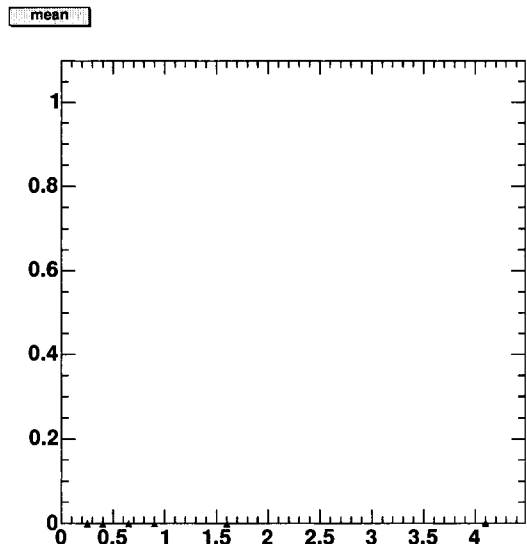


Figure 5.18: mean of gaussian fits to signalized phi variable as function of p_T .

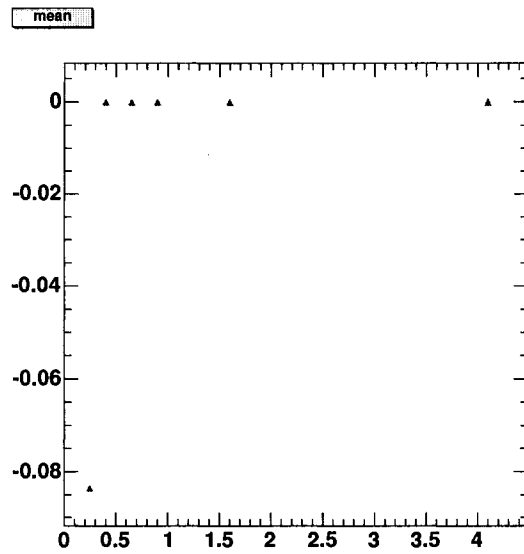


Figure 5.19: mean of gaussian fits to signalized dz variable as function of p_T .

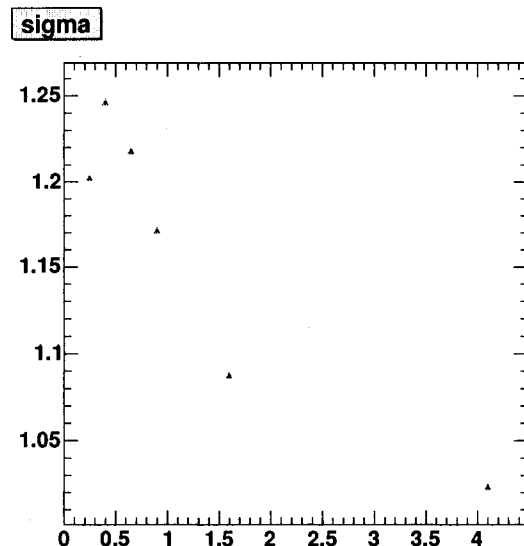


Figure 5.20: sigma of gaussian fits to signalized energy over momentum variable as function of p_T .

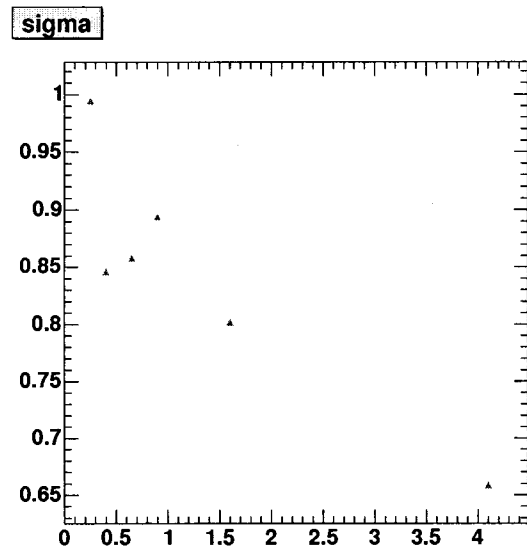


Figure 5.21: sigma of gaussian fits to signalized phi variable as function of p_T .

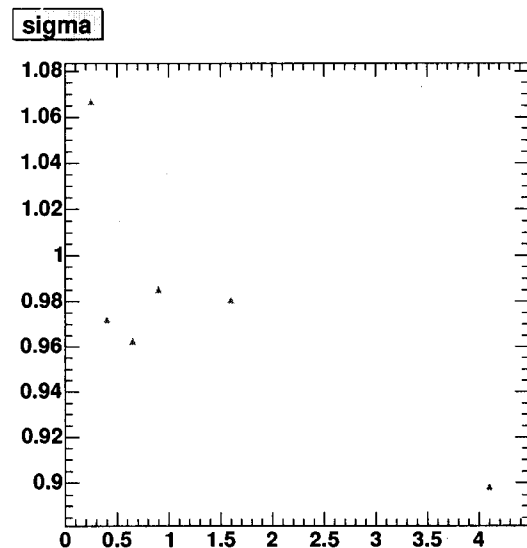


Figure 5.22: sigma of gaussian fits to signalized dz variable as function of p_T .

- PISA ³ files are generated from the EXODUS input, with PISA configured to simulate the Au + Au Run II configuration of the experiment,
- the PISA files are run through the standard Run-2 reconstruction using the same version of the PHENIX, offline analysis software libraries that were used originally for the production of the data,
- input and reconstructed p_T distributions are weighted consistently such that the input agrees in shape with the finally measured, fully corrected invariant electron spectra. ,
- the ratio of generated and reconstructed spectra defines the single particle correction function. This process needs to be iterated until the calculated correction function doesn't change any further. As the starting point, we use the original flat p_T distribution. The iteration converges already after the second step. That means that the correction function is not very sensitive to the exact form of the weighting function as long as it roughly reflects the shape of the true spectra, and
- the multiplicity dependent efficiency loss caused by high detector occupancy is estimated using a standard PHENIX technique of embedding simulated single-electrons into real events and evaluating the probability to reconstruct the embedded particle in the merged event.

The resulting single-electron correction functions, not including the embedding correction, from the first and second iteration step are shown in Fig. 5.23. The correction function does not differ from the second iteration step for any

³a GEANT based simulation of the interaction of particles with the PHENIX detector.

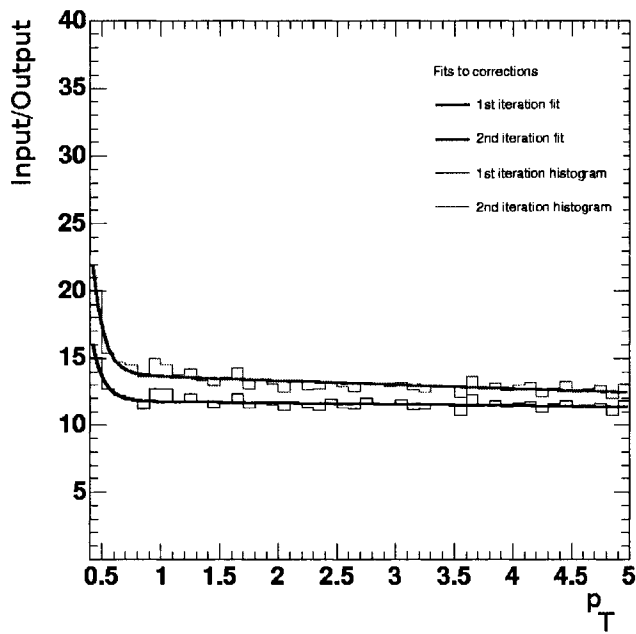


Figure 5.23: Corrections for acceptance and reconstruction efficiency are shown as function of p_T . Both the first and the second iterations are shown. The latter is applied track-by-track in the analysis.

further iterations. We apply the fit to this correction function track-by-track in the analysis.

In principle, the shape of the fully corrected electron spectra could change with event centrality. Thus, the weighting function would also depend on centrality. Together, these two dependencies would lead to different correction functions for the individual centrality classes. However, the resulting correction function is not very sensitive to the weighting function. As long as the weighting spectra do not exhibit vastly different shapes (and they do not), the single-electron correction function turns out to be effectively centrality independent.

5.7.2 Normalization of the EE Rungroup

It was discussed earlier that this correction, can only be applied to the QM rungroup. We have shown that applying it to the EE rungroup, will result in the correct shape of the corrected spectra (since the shape of raw electron spectra is the same in both rungroups), but not necessarily in the correct absolute normalization. It turns out, the normalization is also essentially the same. Fig. 5.5 shows the ratio of the corrected Minimum bias electron spectra from both rungroups together with a fit to a constant. The ratio is p_T independent (which we knew already) and very close to unity. We rescale the correction function for the EE rungroup by the fit value (1.019), and assign a systematic uncertainty of 3 % to this normalization procedure as discussed earlier.

5.7.3 Embedding Correction

To account for the multiplicity dependent efficiency loss, we apply a p_T independent correction determined via a standard embedding technique used in PHENIX analysis. The correction is really a scale factor applied to the p_T spectra that accounts for the limited efficiency of the track reconstruction. Events with higher numbers of charged particles, can and do lose tracks as the reconstruction algorithms are applied and this scale factor will correct for it. The embedding efficiencies were determined in [15] and the efficiencies used are summarized in Table 5.2 below.

To determine this correction, simulated tracks are embedded within events from real data and then passed through the reconstruction software. An examination of the resulting reconstructed set of tracks allows us to determine an efficiency associated with high numbers of tracks in events. The inverse of that efficiency is our correction.

5.8 Systematic Uncertainties

Each source of systematic error in this measurement is taken into account in this section. Systematic sources are considered separately and then combined into a total figure. At high p_T , in our region of main interest, systematic uncertainties are similar in size to the statistical uncertainties.

For the Cocktail subtraction method, the systematic errors will dominate the measurement of non-photonic electrons at low p_T . This is an unavoidable consequence of the method. At low p_T , the inclusive spectrum is mostly background. The cocktail's purpose is to simulate this portion of the spectrum.

The more background there is, the more the cocktail looks like the inclusive spectrum. When we then take the difference of the inclusive and the cocktail, we calculate the difference of two large numbers that are close to each other. Standard error propagation then generates large systematic errors. This is why the cocktail is essentially a high p_T technique. The method works best where the signal to background ratio is high.

In general, we have to consider three contributions to the total systematic errors in this analysis.

1. The fully corrected inclusive electron spectra suffer from systematic uncertainties due to the electron identification cuts, the stability and active area of the detector, the correction function, and the embedding correction. In addition, the renormalization of the EE rungroup introduces a further (small) systematic. The last one, is the only uncertainty listed that is present in this analysis but not in [68]. This group of uncertainties is called *internal* as they are generated by the method used here in this single-electron analysis.
2. To determine the spectra of electrons from non-photonic sources, the electron cocktails from [12] are subtracted from the inclusive spectrum. These, of course, are subject to the systematic uncertainties discussed in detail in [12]. The cocktail is fully discussed in Sec. 5.11.
3. For the calculation of the nuclear modification factor, additional systematic uncertainties related to the reference spectrum from $p + p$ collisions (see [14]) and the nuclear overlap integral T_{ab} are present and must be taken into account as well.

In the following sections, the individual contributions to the total systematic uncertainty are discussed. I mainly focus on the internal systematics since the other contributions are documented in detail elsewhere [12] [14] [68].

5.8.1 Internal Systematics

- Limited Statistics of Monte-Carlo: 5 %

Our estimate of 5 % follows [68] and is consistent with the relative statistical error of every p_T bin in the histogram from which the correction is determined.

- Electron ID cuts

Systematic uncertainties are associated with the cuts for identification of electrons. To estimate an error for each cut, the entire analysis was repeated using two modified cut values: one tighter cut and one looser cut compared to the nominal value. The percent deviation from the new modified result with the unmodified cut was determined as a function of p_T as shown in Figs. 5.24 - 5.29.

Labeling the spectra as tight, loose, and normal we defined the systematic error as

$$\frac{\max\left(\frac{modified}{nominal} - 1\right)}{\sqrt{12}} \times 2 \quad (5.5)$$

The systematics are slightly p_T dependent, but conservatively we assign the maximum value for all p_T . The modified values for the cuts were chosen to be the same as those used in [68] to allow for direct comparisons

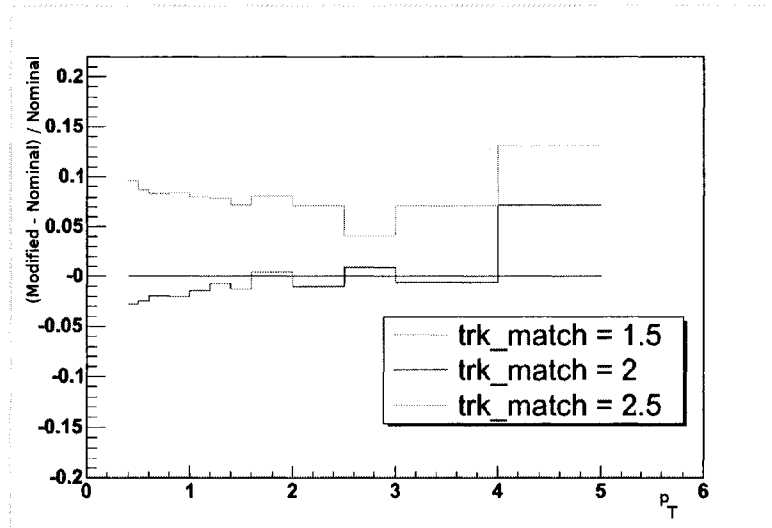


Figure 5.24: Systematic error associated with the track matching.

of the final results. The systematic errors quoted in [68] are happily confirmed here. The current systematic uncertainties are:

- Track-matching cut: 5.8 %,
- n0 cut: 10.4 %,
- n3 cut: 1.7 %,
- chi2 cut: 2.9 %,
- disp cut: 4.6 %, and
- Energy/momentum cut: 2.9 %.

- Detector acceptance: 5 %

The relative agreement between data and simulation for the detector acceptance in the QM rungroup was examined thoroughly for the con-

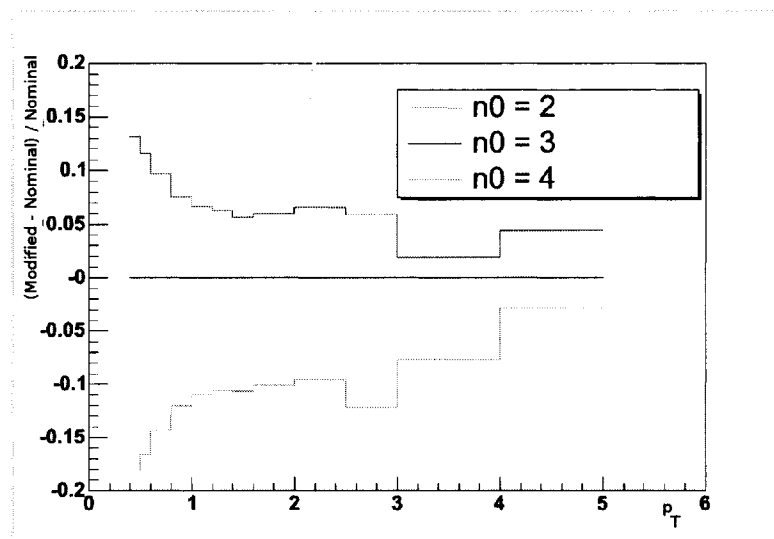


Figure 5.25: Systematic error associated with the n_0 cut.

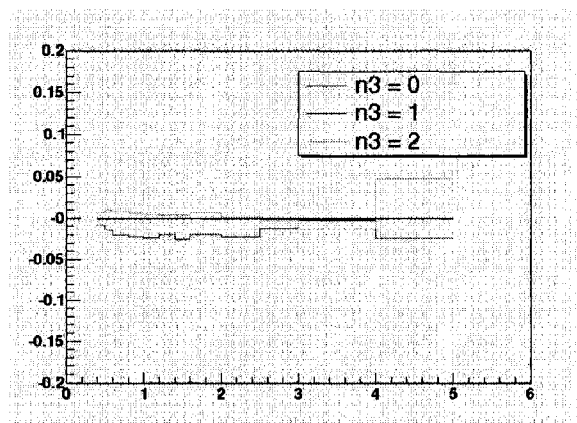


Figure 5.26: Systematic error associated with the n_3 cut.

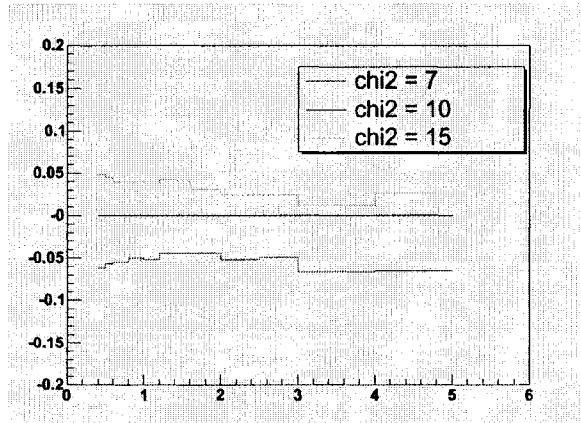


Figure 5.27: Relative error obtained by a variation of the chi2 track variable from which a systematic error is obtained.

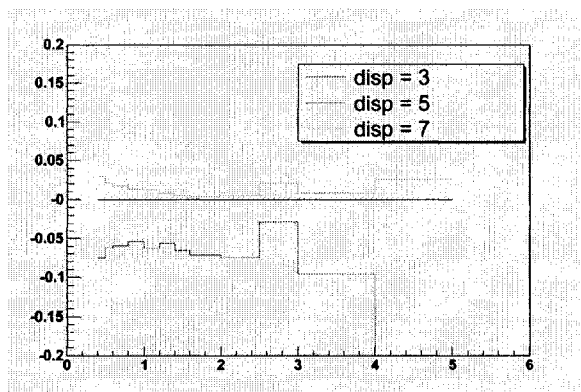


Figure 5.28: Systematic error associated with the disp cut.

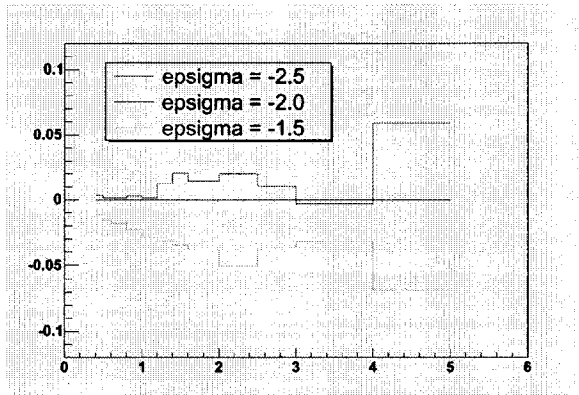


Figure 5.29: Systematic error associated with the signalized e/p cut.

verter analysis and is detailed in [68]. Instead of repeating the same studies, we quote the value 5 % from [68] for this systematic uncertainty.

- EE rungroup normalization

As discussed before 5.7.2, the absolute normalization of the EE rungroup to the fully corrected QM rungroup can be achieved to within a systematic uncertainty of about 3 %. This value is conservative.

- Embedding correction: 1-7 % (centrality dependent)

Both the East and West arms of the detector were studied separately and the embedding corrections were found to be different for both by a significant amount that is still unexplained.

5.8.2 Cocktail Systematics

As discussed, in [12], the systematic uncertainties associated with the cocktails in various centrality classes, increase from about 10 % at low p_T to about 15 %

Table 5.2: Centrality dependent embedding efficiencies for each centrality class are tabulated here. The inclusive spectra are scaled by these numbers to account for the higher number of tracks in more central collisions and the consequent reduction in reconstruction efficiency.

Centrality Class	Average	East	$\frac{A-E}{E}$
Min. Bias	0.834	0.781	0.064
00 - 10 %	0.791	0.738	0.067
10 - 20 %	0.827	0.760	0.081
20 - 40 %	0.869	0.817	0.060
40 - 60 %	0.924	0.890	0.037
60 - 92 %	0.965	0.959	0.006

at high p_T . Conservatively we assign a p_T independent systematic of 15 % for all p_T and centrality classes.

5.8.3 p + p Reference

The p + p reference spectrum is taken from ppg037 [14]. We use the point-by-point systematic uncertainty quoted there. The relative error for the p + p spectrum is roughly 15% at high p_T .

5.8.4 T_{ab}

The values for the nuclear overlap integrals defined in 4.0.1 (T_{ab}) and the corresponding uncertainties for the various centrality classes are taken from [16]. They are listed in Tab. 5.3. These uncertainties are p_T independent.

5.8.5 Summary

A summary of all systematics for this analysis is given in Table 5.4. For each contribution, we have repeated and confirmed an earlier determination by [68].

Table 5.3: Centrality dependent relative systematic errors associated with T_{AB} .

Centrality Class	T_{ab}	Rel. Error
Min. Bias	6.14	0.073
00 - 10 %	22.75	0.069
10 - 20 %	14.27	0.070
20 - 40 %	7.07	0.082
40 - 60 %	2.16	0.120
60 - 80 %	.49	0.285

Table 5.4: Summary of all internal systematics for the analysis. This summary includes both internal and external errors.

Systematic	Error
Statistics on Monte-Carlo	5 %
Track Matching	5.8 %
n0	10.4 %
n3	1.7 %
chi2	2.9 %
disp	4.6 %
depemc	2.9 %
Acceptance	5 %
EE Renormalization	3 %
Embedding correction	1-7 %

This was to be expected and adds confidence to the result.

5.9 Fully-corrected Inclusive Electron p_T Spectra

The resulting fully corrected invariant electron p_T spectra are shown in Figs. 5.30 - 5.36 for all centrality classes. These spectra are not bin-width corrected (see Sec. 5.12.1). Currently, we apply this correction only for the non-photonic spectra, after the cocktails (see below) have been subtracted. The correspond-

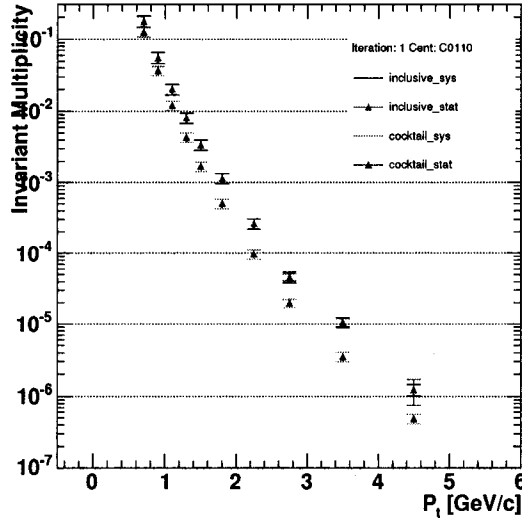


Figure 5.30: Overlay of inclusive electrons and coctail for 0 - 10 % centrality class. Error bars (brackets) are statistical (systematic) errors.

ing background electron cocktails are overlayed.

5.10 Electron Cocktail Calculations

For a detailed description of the cocktails used here, I will just refer you to 5.11. Here, I will just list the electron sources that contribute to the current cocktails:

- Dalitz decays of light neutral mesons. ($\pi_0 \rightarrow \gamma e^+ e^-$, η, ω, ϕ , etc...),
- conversions of photons from the decay of light neutral mesons,
- dielectron decays of vector mesons (ρ, ω, ϕ ...),
- weak decays of kaons (K_{e3}), and

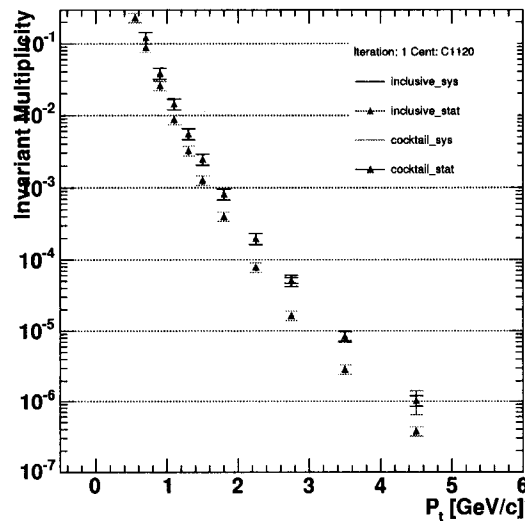


Figure 5.31: Overlay of inclusive electrons and coctail for 10 - 20 % centrality class. Error bars (brackets) are statistical (systematic) errors.

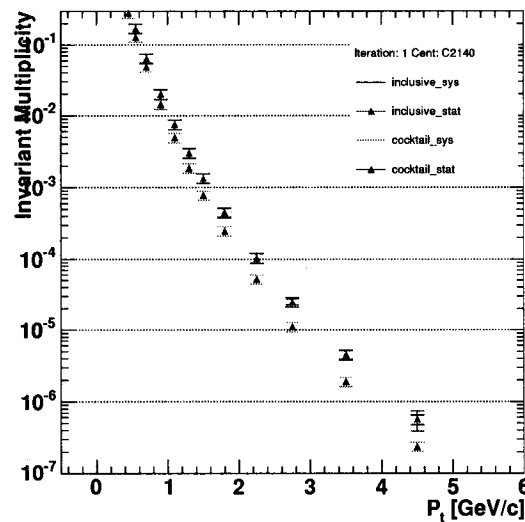


Figure 5.32: Overlay of inclusive electrons and coctail for 20 - 40 % centrality class. Error bars (brackets) are statistical (systematic) errors.

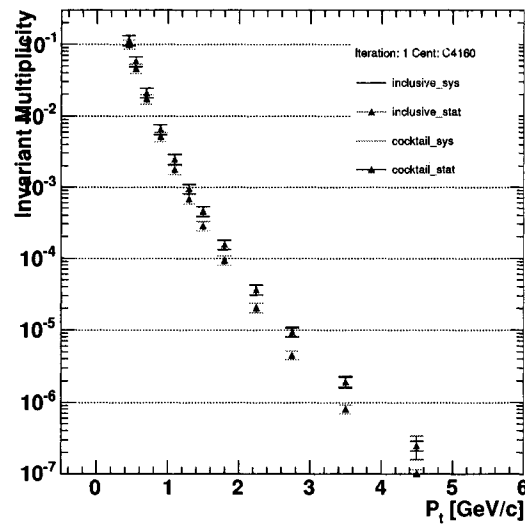


Figure 5.33: Overlay of inclusive electrons and coctail for 40 - 60 % centrality class. Error bars (brackets) are statistical (systematic) errors.

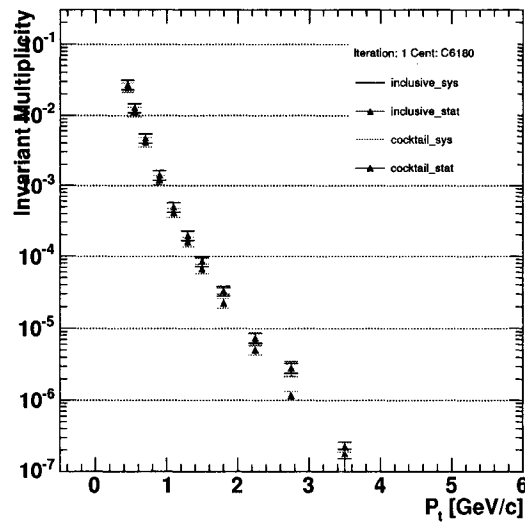


Figure 5.34: Overlay of inclusive electrons and coctail for 60 - 80 % centrality class. Error bars (brackets) are statistical (systematic) errors.

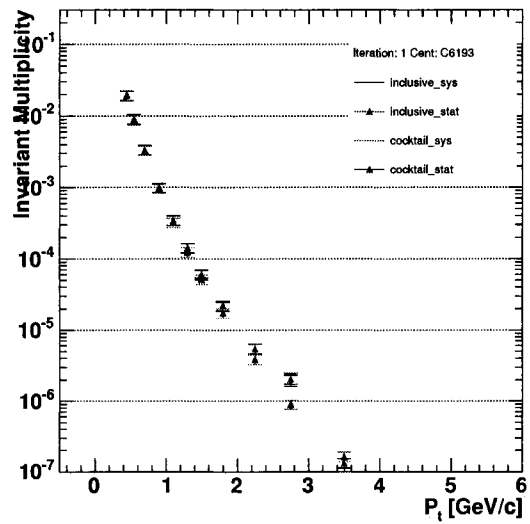


Figure 5.35: Overlay of inclusive electrons and coctail for 60 - 92 % centrality class. Error bars (brackets) are statistical (systematic) errors.

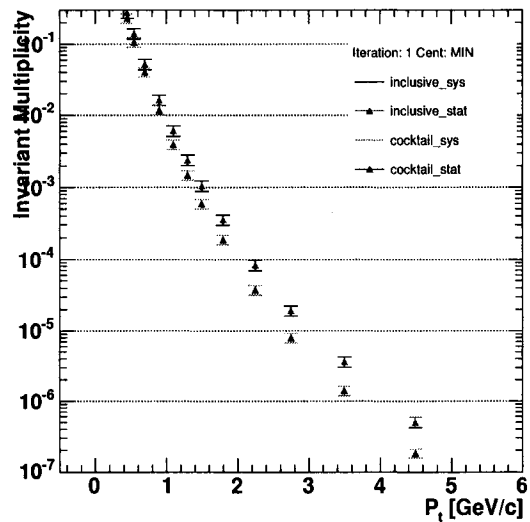


Figure 5.36: Overlay of inclusive electrons and coctail for Minimum Bias. Error bars (brackets) are statistical (systematic) errors.

- direct radiation (virtual photons and conversions of real photons).

A breakdown of the minimum bias cocktail is shown in Fig. 5.37. The upper panel shows an overlay of the cocktail, the measured inclusive p_T spectrum of electrons, and the corresponding spectrum for each cocktail component. The lower panel shows the relative contribution to the total for each cocktail component.

The subtraction of these cocktails from the inclusive spectra leaves us with electrons from the following possible sources:

- semi-leptonic decays of particles carrying heavy flavor, mainly charm, but also a significant contribution from beauty decays at high p_T ,
- thermal radiation, which is expected to be small and concentrated at low p_T (if present at all),
- Drell-Yan (which shouldn't be important for the p_T range we are considering) and ,
- new physics.

5.11 Details of the Cocktail

This section describes the calculation of an electron cocktail $(e^- + e^+)/2$ for Au + Au collisions at $\sqrt{s_{NN}} = 200$ GeV using the EXODUS event generator and decay machinery. The input for the calculation is taken from published PHENIX Run-2 data. For the calculation of electrons from photon conversions,

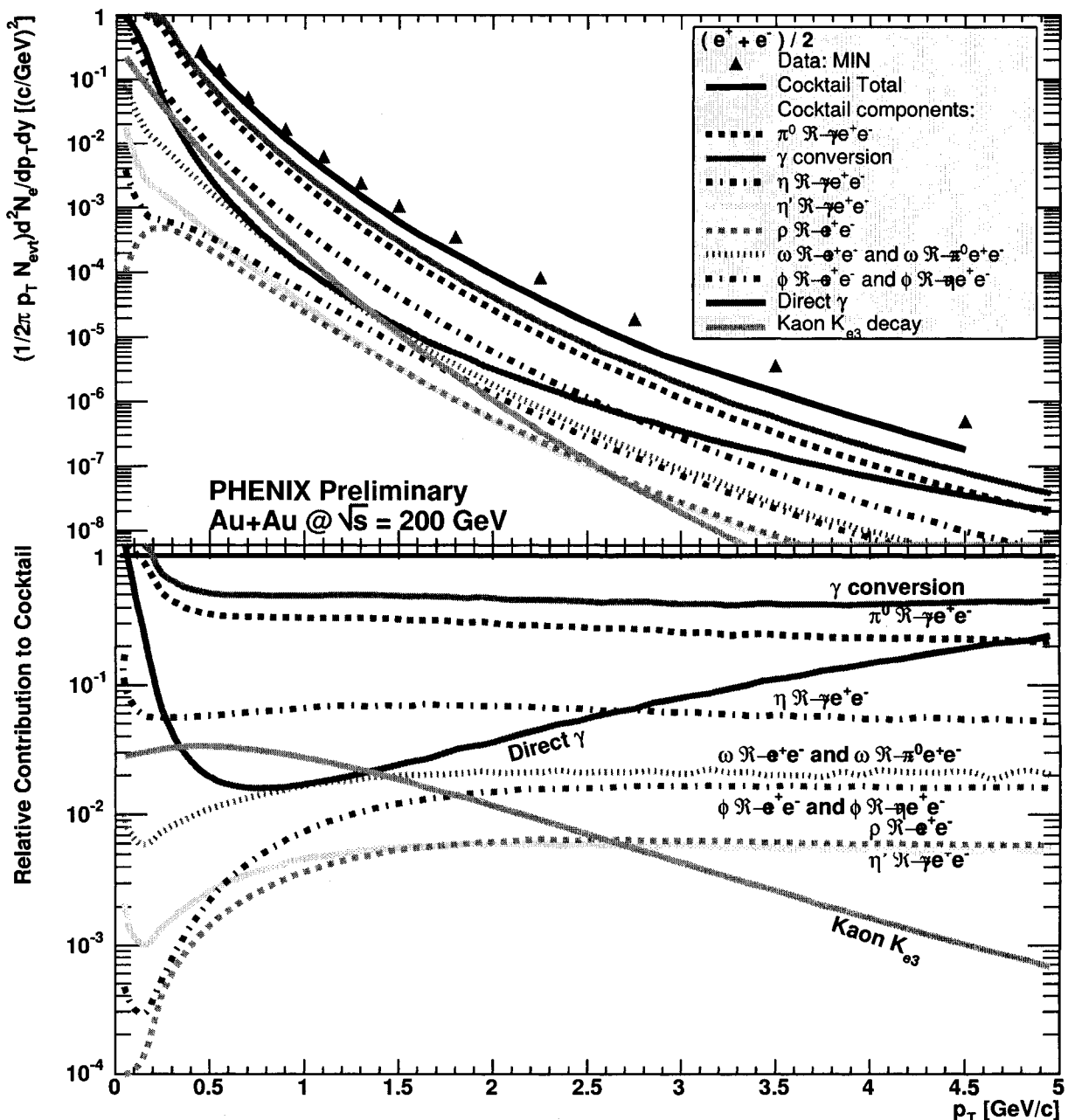


Figure 5.37: The upper panel shows the minimum bias cocktail overlayed with the minimum bias inclusive electron spectrum. Each component is shown as well. The breakdown by contribution is laid out in the legend. The lower panel shows the relative contribution of each component in the cocktail.

the material taken into account corresponds to the material present in the PHENIX experiment in Run-2. The general procedure of cocktail calculations with EXODUS was described in detail already in Refs. [60, 61]. Here, we focus on a careful description of the parameterizations used as input for the present cocktail calculation, present the resulting cocktails in various Au + Au centrality bins, discuss the systematic uncertainties, and compare the photonic part of the cocktails with the corresponding photonic spectra as determined via a single electron *converter subtraction* analysis of the Run-2 Au + Au data [62]

5.11.1 Overview

The electron sources considered in the present cocktail fall into one of two categories, *i.e.* photonic or non-photonic sources. The subsequent sections describe the implementation of the following photonic sources

- Dalitz decays of light neutral mesons: $\pi^0, \eta, \omega, \eta', \phi$
- conversions of photons from decays of these light neutral mesons in material
- conversion of direct photons, *e.g.* from quark-gluon Compton scattering, in material

Non-photonic sources that are implemented are

- di-electron decays of light vector mesons: ρ, ω, ϕ
- weak kaon decays, referred to as K_{e3} decays

- virtual direct photons from initial hard scattering processes

Particle properties, *i.e.* masses and branching ratios for the various decay modes, are implemented according to [59]. Thermal radiation is not included in the present cocktail.

5.11.2 Neutral pions

The dominant electron source is the π^0 meson, directly via its Dalitz decay $\pi^0 \rightarrow \gamma e^+ e^-$ and indirectly via conversion electrons from photons originating from $\pi^0 \rightarrow \gamma\gamma$. An excellent parameterization of the invariant pion spectra is therefore mandatory for a high quality electron cocktail.

The rapidity distribution of neutral pions is assumed to be flat around mid rapidity. This assumption is well justified and we do not assign a systematic uncertainty to it.

As discussed in [60] it is a reasonable approach to determine the neutral pion p_T distribution used as input for the cocktail calculation by a simultaneous fit to published charged and neutral pion data. Here, we use the neutral pion data from [63] and the charged pion data from [64]. The combined data are fit according to the following modified Hagedorn parameterization:

$$\frac{1}{(2\pi p_T)} \frac{d^2 N}{dp_T dy} = \frac{c}{(\exp(-ap_T - bp_T^2) + p_T/p_0)^n} \quad (5.6)$$

Fig. 5.38 shows the minimum bias pion data together with the fit (left panel). The ratio of data and fit (right panel) demonstrates the excellent quality of this parameterization. The error bars shown are purely statistical. The corresponding fits and ratios for the Au+Au centrality classes 0-10 %,

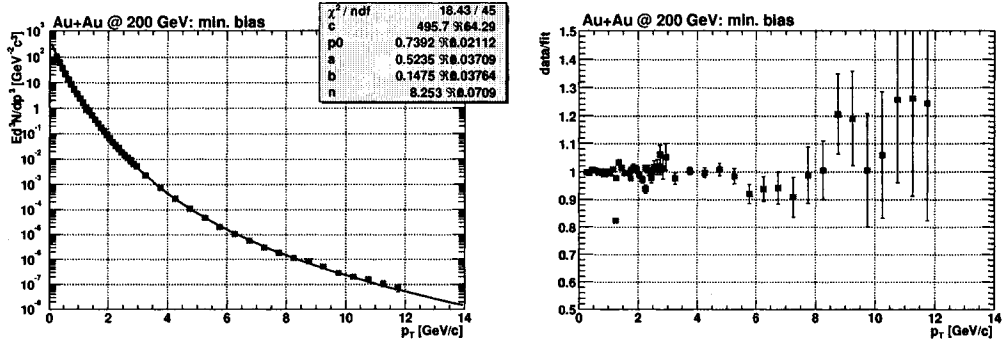


Figure 5.38: Fit of the combined charged (blue symbols at low p_T) and neutral pion spectra (red symbols at high p_T) according to Eq. 5.6 in minimum bias collisions (left panel) and ratio of data and fit (right panel). Error bars are statistical uncertainties only.

10-20 %, and 20-40 % are shown in Fig. 5.39. The remaining centrality classes 40-60 %, 60-80 %, and 60-92 % are displayed in Fig. 5.40.

The fit parameters for the pion invariant p_T distribution are summarized in Tab. 5.5 together with the corresponding values of dN_{π^0}/dy , as obtained by integrating the fit, which determines the absolute normalization of the electron cocktail.

In order to estimate the systematic uncertainty of the electron cocktail due to the uncertainty of the pion input parameterization, we adopt the following strategy:

1. move all charged and neutral pion data points up (down) by their individual systematic uncertainties taken from Refs. [63, 64].
2. redo the fit procedure described above to determine the 1σ upper (lower) systematic error parameterization for the pion input.
3. rerun the full cocktail for upper (lower) limits for the pion input.

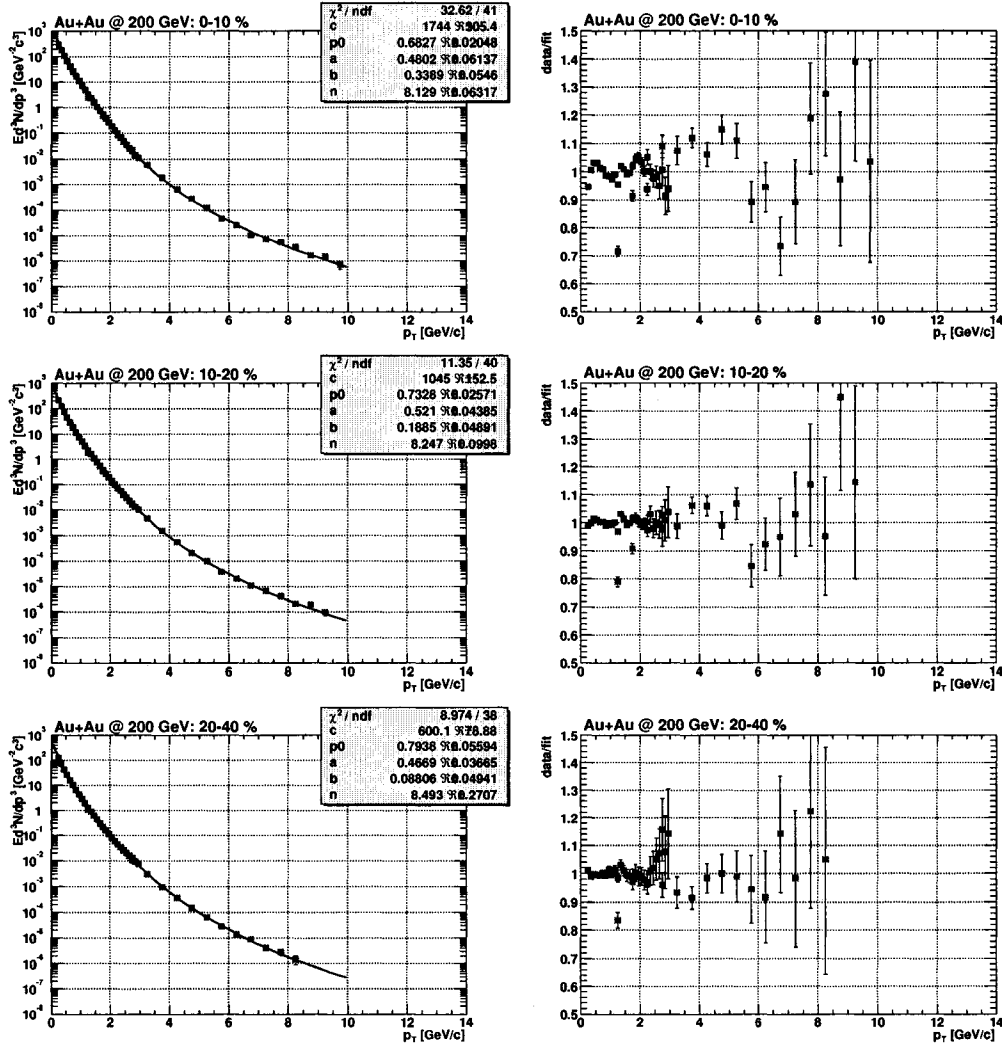


Figure 5.39: Fits of the combined charged (blue symbols at low p_T) and neutral pion spectra (red symbols at high p_T) according to Eq. 5.6 in 0-10 % (upper panels), 10-20 % (middle panels), and 20-40 % (lower panels) central collisions are shown on the left. The corresponding ratio of data and fits are shown on the right. Error bars are statistical uncertainties only.

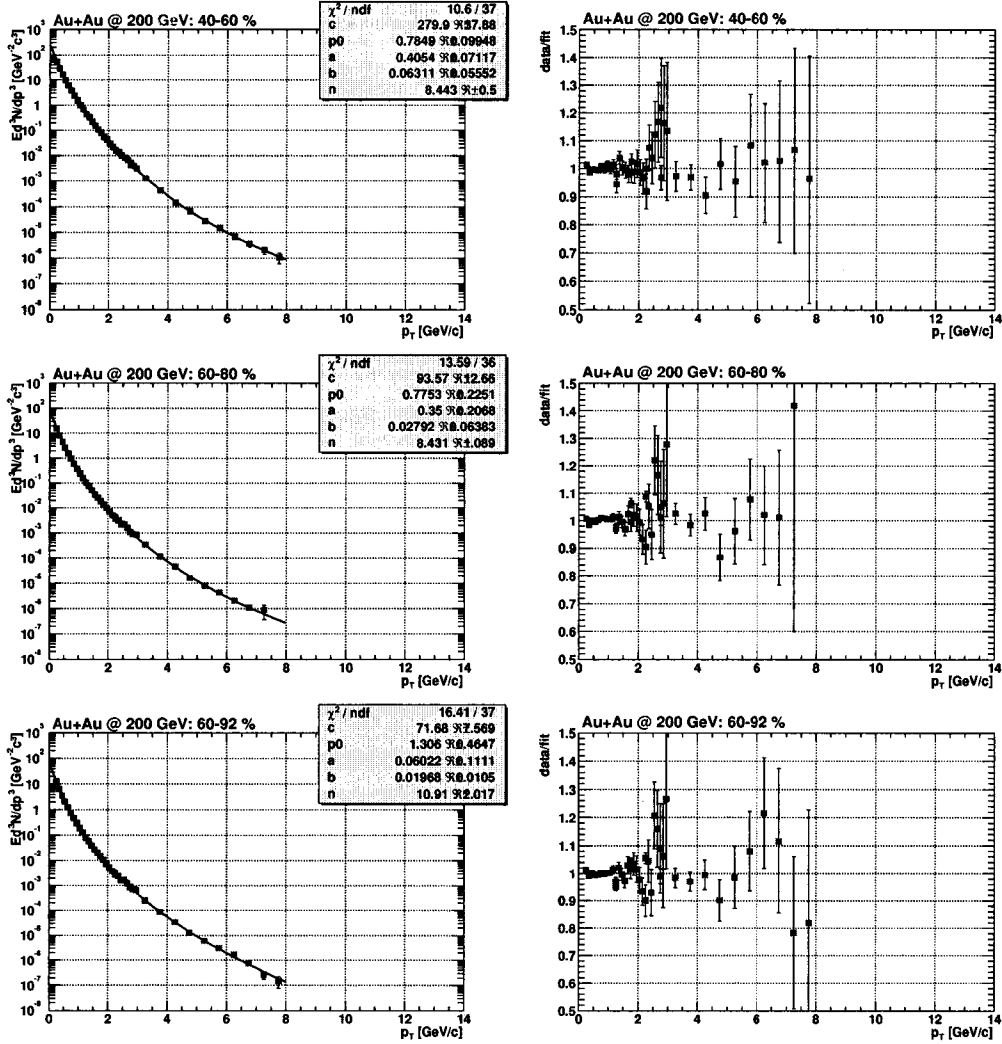


Figure 5.40: Fits of the combined charged (blue symbols at low p_T) and neutral pion spectra (red symbols at high p_T) according to Eq. 5.6 in 40-60 % (upper panels), 60-80 % (middle panels), and 60-92 % (lower panels) central collisions are shown on the left. The corresponding ratio of data and fits are shown on the right. Error bars are statistical uncertainties only.

centrality	c [(GeV/c) $^{-2}$]	a [(GeV/c) $^{-1}$]	b [(GeV/c) $^{-2}$]	p_0 [GeV/c]	n	dN $_{\pi^0}$ /dy
min. bias	495.7	0.5235	0.1475	0.7392	8.253	95.51
0 - 10 %	1744.0	0.4802	0.3389	0.6827	8.129	293.4
10 - 20 %	1045.0	0.5210	0.1885	0.7328	8.247	202.0
20 - 40 %	600.1	0.4669	0.0881	0.7938	8.493	116.0
40 - 60 %	279.9	0.4054	0.0631	0.7849	8.443	46.67
60 - 80 %	93.57	0.3500	0.0279	0.7753	8.431	13.37
60 - 92 %	71.68	0.0602	0.0197	1.306	10.91	10.52

Table 5.5: Fit parameters for the neutral pion invariant p_t distributions according to Eq. 5.6. In addition, the last column gives the integrated neutral pion yield corresponding to the parametrization.

centrality	c [(GeV/c) $^{-2}$]	a [(GeV/c) $^{-1}$]	b [(GeV/c) $^{-2}$]	p_0 [GeV/c]	n	dN $_{\pi^0}$ /dy
min. bias	530.9	0.5329	0.1526	0.7300	8.182	102.4
0 - 10 %	1891.0	0.4807	0.3505	0.6749	8.070	315.0
10 - 20 %	1119.0	0.5287	0.1929	0.7250	8.184	216.4
20 - 40 %	636.1	0.4754	0.0838	0.7897	8.443	124.1
40 - 60 %	297.7	0.4117	0.0582	0.7809	8.392	49.97
60 - 80 %	99.29	0.3174	0.0160	0.8088	8.559	14.30
60 - 92 %	76.36	0.0373	0.0211	1.391	11.24	11.27

Table 5.6: Fit parameters for the 1σ upper limit for the neutral pion invariant p_t distributions according to Eq. 5.6.

centrality	c [(GeV/c) $^{-2}$]	a [(GeV/c) $^{-1}$]	b [(GeV/c) $^{-2}$]	p_0 [GeV/c]	n	dN $_{\pi^0}$ /dy
min. bias	459.9	0.5121	0.1409	0.7513	8.344	88.65
0 - 10 %	1597.0	0.4793	0.3251	0.6924	8.204	271.7
10 - 20 %	970.4	0.5118	0.1832	0.7425	8.327	187.5
20 - 40 %	563.9	0.4566	0.0925	0.7994	8.556	107.9
40 - 60 %	262.1	0.3966	0.0680	0.7914	8.513	43.38
60 - 80 %	87.98	0.3681	0.0404	0.7554	8.367	12.44
60 - 92 %	67.05	0.0953	0.0187	1.202	10.51	9.778

Table 5.7: Fit parameters for the 1σ lower limit for the neutral pion invariant p_t distributions according to Eq. 5.6.

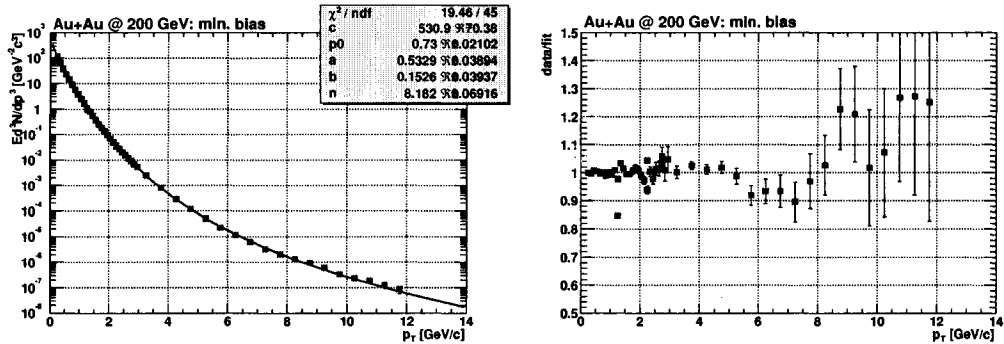


Figure 5.41: Fit of the combined charged (blue symbols at low p_T) and neutral pion spectra (red symbols at high p_T) according to Eq. 5.6 in minimum bias collisions (left panel) and ratio of data and fit (right panel). All data points have been moved up by their individual systematic uncertainty to estimate a 1σ upper limit for the pion input. Error bars are statistical uncertainties only.

4. the difference between the cocktails using upper (lower) limits for the pion input and the cocktails derived from the unmodified pion input defines the 1σ sys. uncertainty of the cocktail due to the uncertainty of the pion input.

The 1σ upper systematic limits on the pion input are shown in Figs. 5.41 (min. bias), 5.42 (0-10 %, 10-20 %, and 20-40 % central), and 5.43 (40-60 %, 60-80 %, and 60-92 % central). The corresponding fit parameters are summarized in Tab. 5.6.

The 1σ lower systematic limits on the pion input are shown in Figs. 5.44 (min. bias), 5.45 (0-10 %, 10-20 %, and 20-40 % central), and 5.46 (40-60 %, 60-80 %, and 60-92 % central). The corresponding fit parameters are summarized in Tab. 5.7.

The current approach is based on the assumption of charge symmetry, *i.e.* that the spectra of neutral pions agree with the average of charged pions

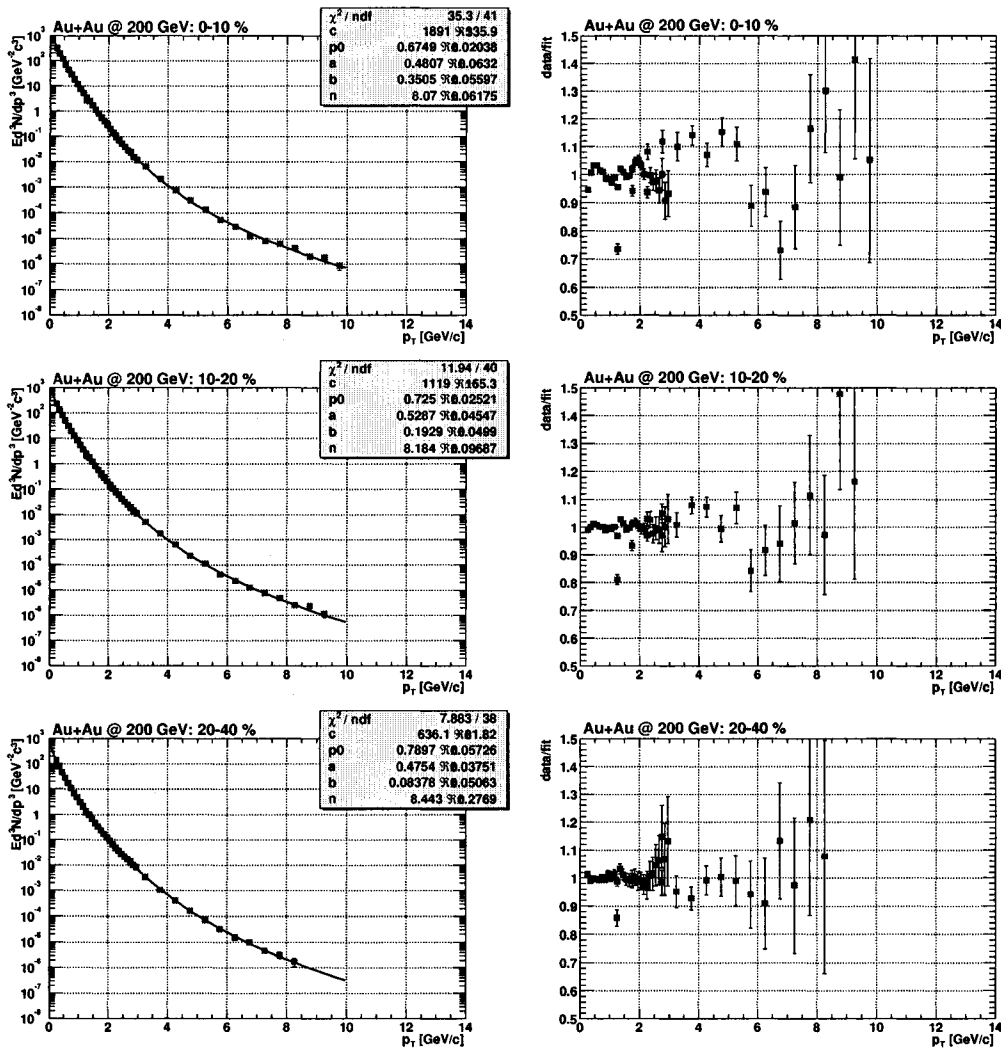


Figure 5.42: Fits of the combined charged (blue symbols at low p_T) and neutral pion spectra (red symbols at high p_T) according to Eq. 5.6 in 0-10 % (upper panels), 10-20 % (middle panels), and 20-40 % (lower panels) central collisions are shown on the left. All data points have been moved up by their individual systematic uncertainty to estimate a 1σ upper limit for the pion input. The corresponding ratio of data and fits are shown on the right. Error bars are statistical uncertainties only.

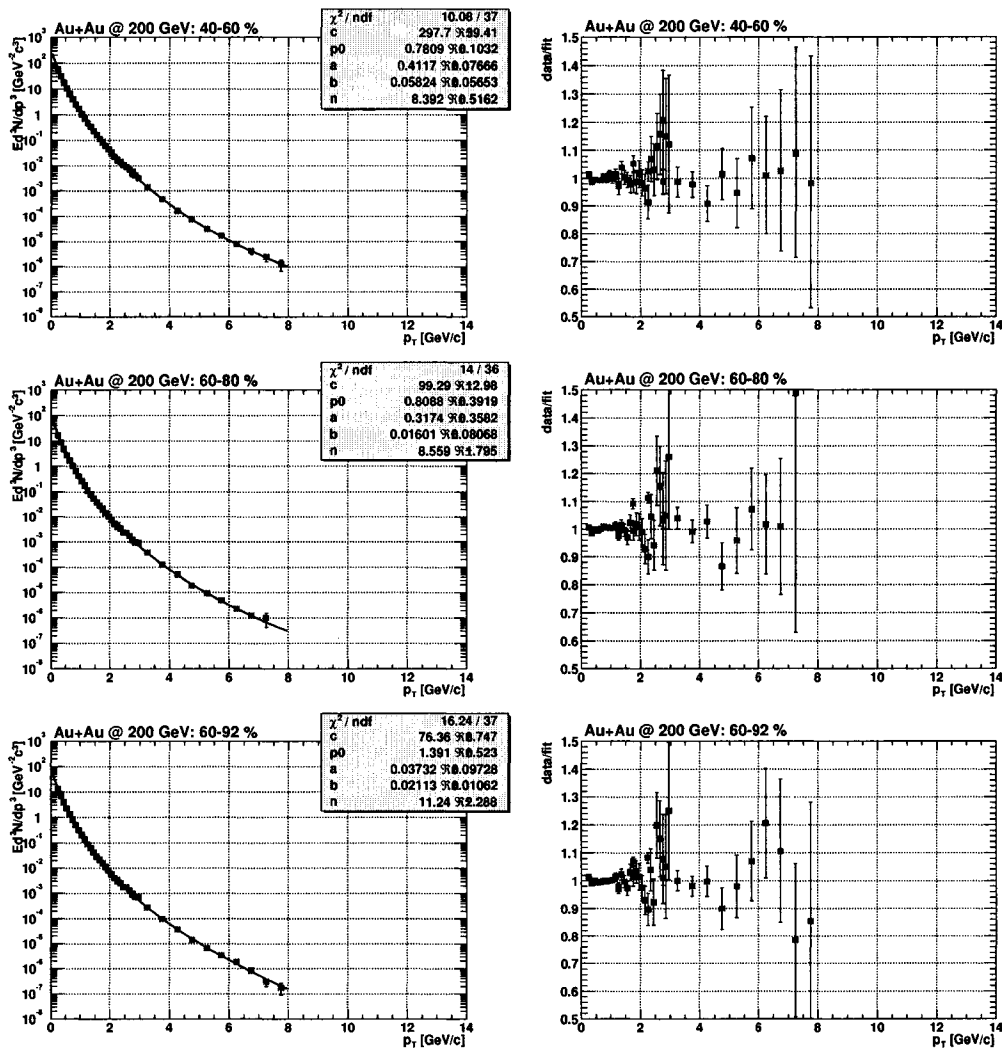


Figure 5.43: Fits of the combined charged (blue symbols at low p_T) and neutral pion spectra (red symbols at high p_T) according to Eq. 5.6 in 40-60 % (upper panels), 60-80 % (middle panels), and 60-92 % (lower panels) central collisions are shown on the left. All data points have been moved up by their individual systematic uncertainty to estimate a 1σ upper limit for the pion input. The corresponding ratio of data and fits are shown on the right. Error bars are statistical uncertainties only.

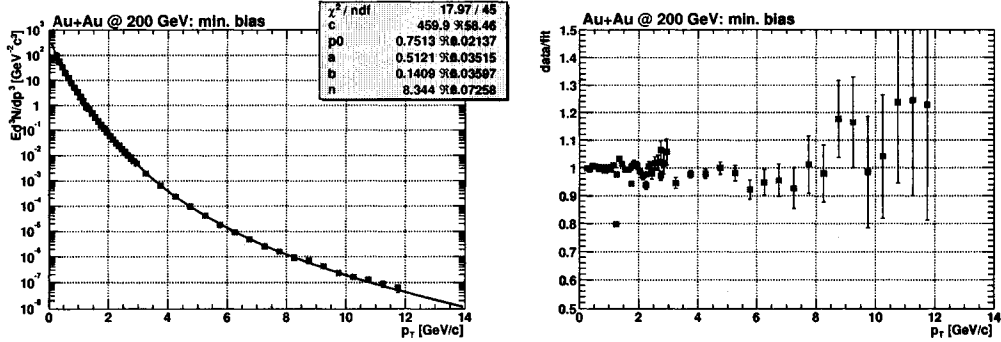


Figure 5.44: Fit of the combined charged (blue symbols at low p_T) and neutral pion spectra (red symbols at high p_T) according to Eq. 5.6 in minimum bias collisions (left panel) and ratio of data and fit (right panel). All data points have been moved down by their individual systematic uncertainty to estimate a 1σ lower limit for the pion input. Error bars are statistical uncertainties only.

$\pi^0 = (\pi^+ + \pi^-)/2$. This assumption is not exactly correct, mainly because of the decay $\eta \rightarrow 3\pi^0$ which creates a charge asymmetry. This effect is tiny and relevant only at low p_T (below 0.5 GeV/c) as can be shown via simulations, *e.g.* by PYTHIA. This is demonstrated in Fig. 5.47, which shows the ratio $2\pi^0/(\pi^+ + \pi^-)$ as function of p_T determined in a PYTHIA calculation of 200 GeV p+p collisions [65]. The p_T dependence can be parameterized according to:

$$\frac{2\pi^0}{\pi^+ + \pi^-} = 1 + \frac{0.636}{\exp(7.74p_T)} \quad (5.7)$$

This expression is multiplied as a correction to Eq. 5.6 to determine the final cocktail input for the invariant spectra of neutral pions. It is important to note that this correction is essentially irrelevant for the electron p_T range of interest here.

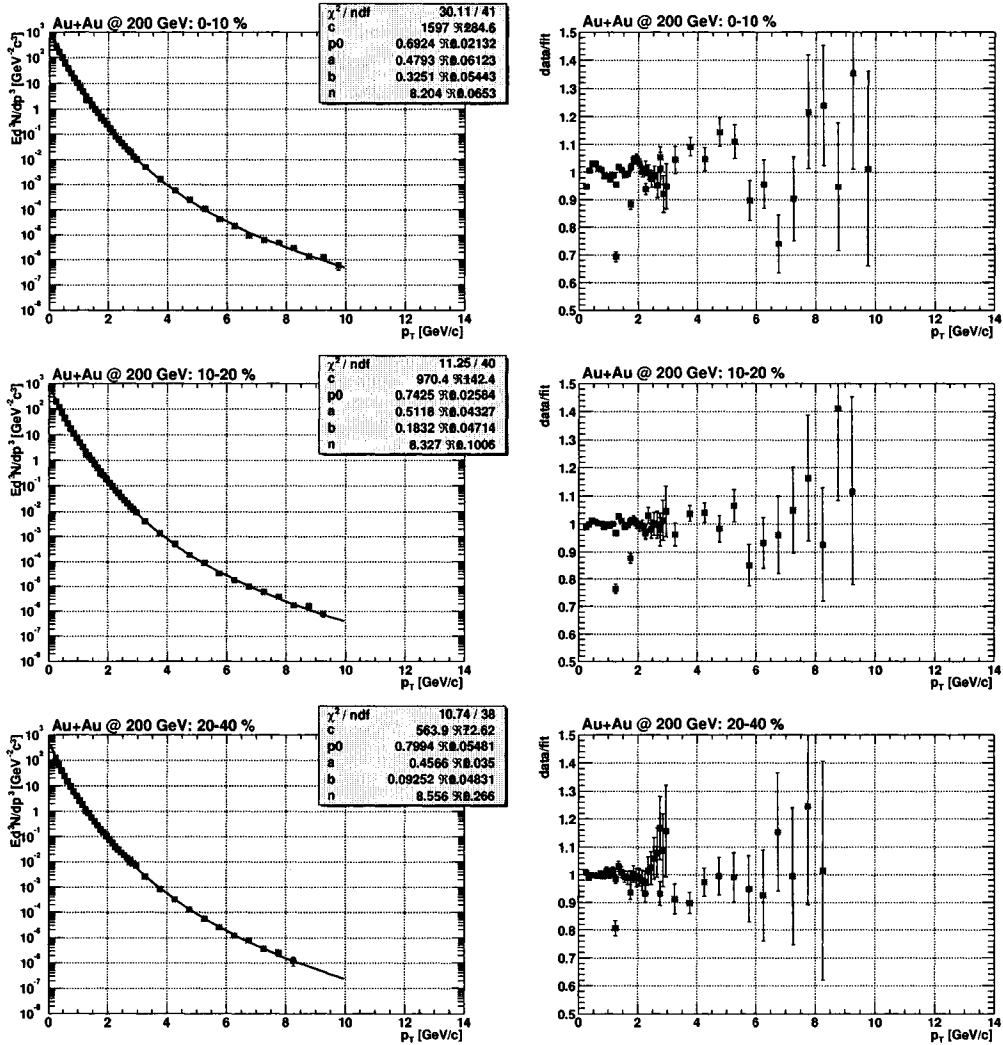


Figure 5.45: Fits of the combined charged (blue symbols at low p_T) and neutral pion spectra (red symbols at high p_T) according to Eq. 5.6 in 0-10 % (upper panels), 10-20 % (middle panels), and 20-40 % (lower panels) central collisions are shown on the left. All data points have been moved down by their individual systematic uncertainty to estimate a 1σ lower limit for the pion input. The corresponding ratio of data and fits are shown on the right. Error bars are statistical uncertainties only.

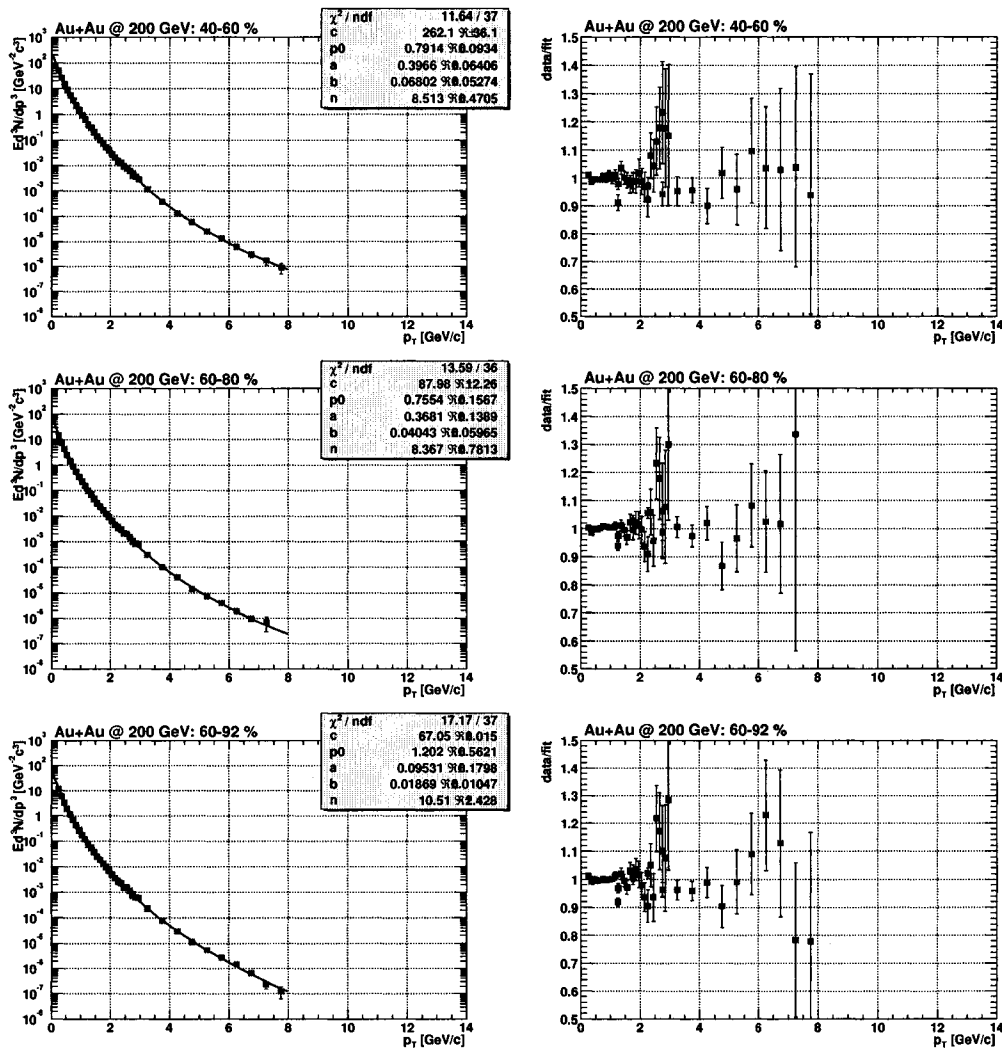


Figure 5.46: Fits of the combined charged (blue symbols at low p_T) and neutral pion spectra (red symbols at high p_T) according to Eq. 5.6 in 40-60 % (upper panels), 60-80 % (middle panels), and 60-92 % (lower panels) central collisions are shown on the left. All data points have been moved down by their individual systematic uncertainty to estimate a 1σ lower limit for the pion input. The corresponding ratio of data and fits are shown on the right. Error bars are statistical uncertainties only.

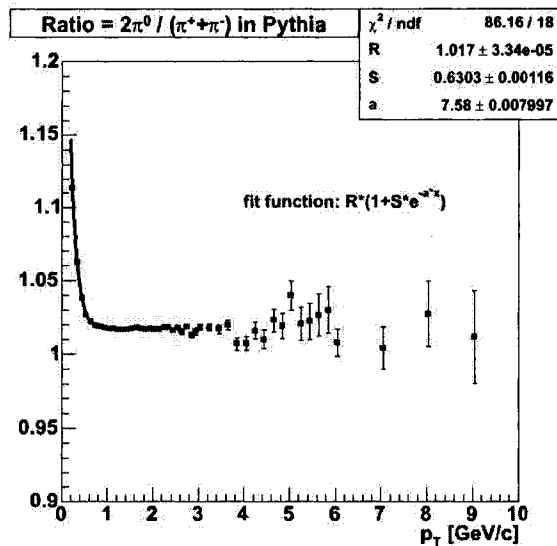


Figure 5.47: Ratio of π^0 and the average of π^+ and π^- from a minimum bias PYTHIA calculation of 200 GeV p+p collisions [65].

5.11.3 Other light mesons

While other light mesons contributing to the inclusive electron spectrum via their decays as considered in the present cocktail are the η , ρ , ω , η' , and ϕ mesons, it is only the η meson that plays a significant role, in particular at high p_T .

As for the π^0 , the rapidity distribution of all other mesons can safely assumed to be flat around mid rapidity. We do not assign a systematic error to this assumption.

The shape of the invariant p_T distributions and the relative normalization to the π^0 are required as input parameter. They are determined in exactly the same way as discussed in [60], i.e. the p_T spectra are determined from the pion spectrum by m_T scaling, *i.e.* the same modified Hagedorn parameterization is

used (Eq. 5.6), only p_T is replaced by $\sqrt{p_T^2 + m_{meson}^2 - m_{\pi^0}^2}$.

The relative normalization to the pion is given by the ratios meson-to-pion at high p_T (5 GeV/c is used here). The following values are used, consistent with the ones given in [60] except for the η meson, where the new value of 0.45 is in line with the PHENIX η analysis in 200 GeV p+p collisions [66] and the world average η production systematics from hadronic collisions [67]. The systematic uncertainties correspond to conservative estimates of 30 % 1σ sys. errors on all meson-to-pion ratios except for the η meson, for which the uncertainty is slightly less in accordance with the value used in [68] driven by the available η measurements [66, 67]:

- $\eta/\pi^0 = 0.45 \pm 0.10$
- $\rho/\pi^0 = 1.00 \pm 0.30$
- $\omega/\pi^0 = 1.00 \pm 0.30$
- $\eta'/\pi^0 = 0.25 \pm 0.075$
- $\phi/\pi^0 = 0.40 \pm 0.12$

While all higher mass mesons except for the η are essentially irrelevant in terms of their contribution to the total electron yield, it is important to demonstrate that the chosen parameterization is reasonable for the η meson. While it would be most desirable to compare the parameterization of the η invariant p_T distribution as m_T scaled pion p_T distribution for the current case of Au + Au collisions at 200 GeV, this cross checks needs to be postponed until official η meson spectra become available for the Au + Au system. What

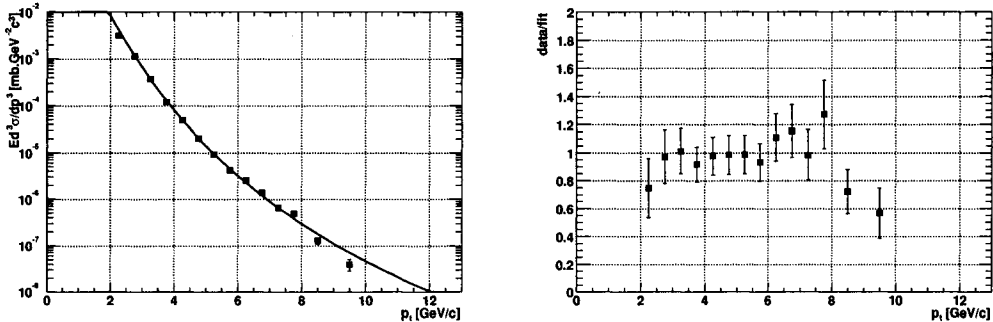


Figure 5.48: η meson invariant cross section (data points) compared with an m_T scaled modified Hagedorn parameterization of the corresponding pion spectra for $p + p$ collisions at 200 GeV (left panel, from [69]). The error bars are statistical only. In the ratio of data to parameterization (right panel), the error bars are the quadratic sum of statistical and systematic uncertainties.

is available right now, are invariant η meson spectra from $p + p$ collisions at 200 GeV [66]. Fig. 5.48 shows the comparison of the corresponding η meson data with the current m_T scaled modified Hagedorn parameterization (fit to pion data from $p + p$ collisions at 200 GeV [69]) both on an absolute scale (left panel) and in form of the ratio of data and parameterization (right panel). In the p_T range covered by the measurement the agreement between η cocktail input and the data is excellent.

5.11.4 Electrons from photon conversions

The treatment of photon conversions is the only ingredient of the current cocktail that depends on the configuration of the experiment, since photon conversions depend on the amount and position of material present in the active area of the experiment, of course. A readjustment of the ratio *Conv/Dalitz* (reconstructed electrons from conversions / reconstructed electrons from Dalitz

decays) for neutral pions for various experimental setups, will allow to reuse the current cocktail calculation for any other Au + Au runs at 200 GeV (in particular, for a Run-4 analysis).

Electrons from photon conversions in material are not intrinsically implemented in EXODUS. However, it is a very good approximation that the p_T spectra of conversion electrons are very similar to the spectra of electrons from Dalitz decays, which are "internal" conversions. It is because of two effects that the spectra of Dalitz and conversion electrons are not identical.

First, the photon conversion probability does not only depend on the material in which the conversion takes place, it also depends slightly on the photon energy, in principle introducing a small p_T dependence of the ratio $Conv/Dalitz$. However, this p_T dependence is very small. For photon energies above 1 GeV (corresponding to electron $p_T \approx 0.5$ GeV/c), the conversion probability rises only marginally [70]. A precise treatment of the photon conversion probability, nevertheless, requires a full GEANT simulation.

Second, the momentum of electrons originating from photon conversions is reconstructed incorrectly if the conversion occurs at a non-zero radial distance R from the coordinate origin in the transverse plane, as it is the case for all conversions. The momentum misreconstruction depends on R . This effect can also be treated only in a full simulation.

Consequently, we follow the same approach as in [69]. The ratio of electrons from photon conversions to electrons from Dalitz decays ($Conv/Dalitz$) is determined as function of electron p_T in a full GEANT (PISA) simulation of neutral pions, which takes the effects discussed above into account intrinsically. It is then well justified to use the same ratio $Conv/Dalitz$, corrected for the

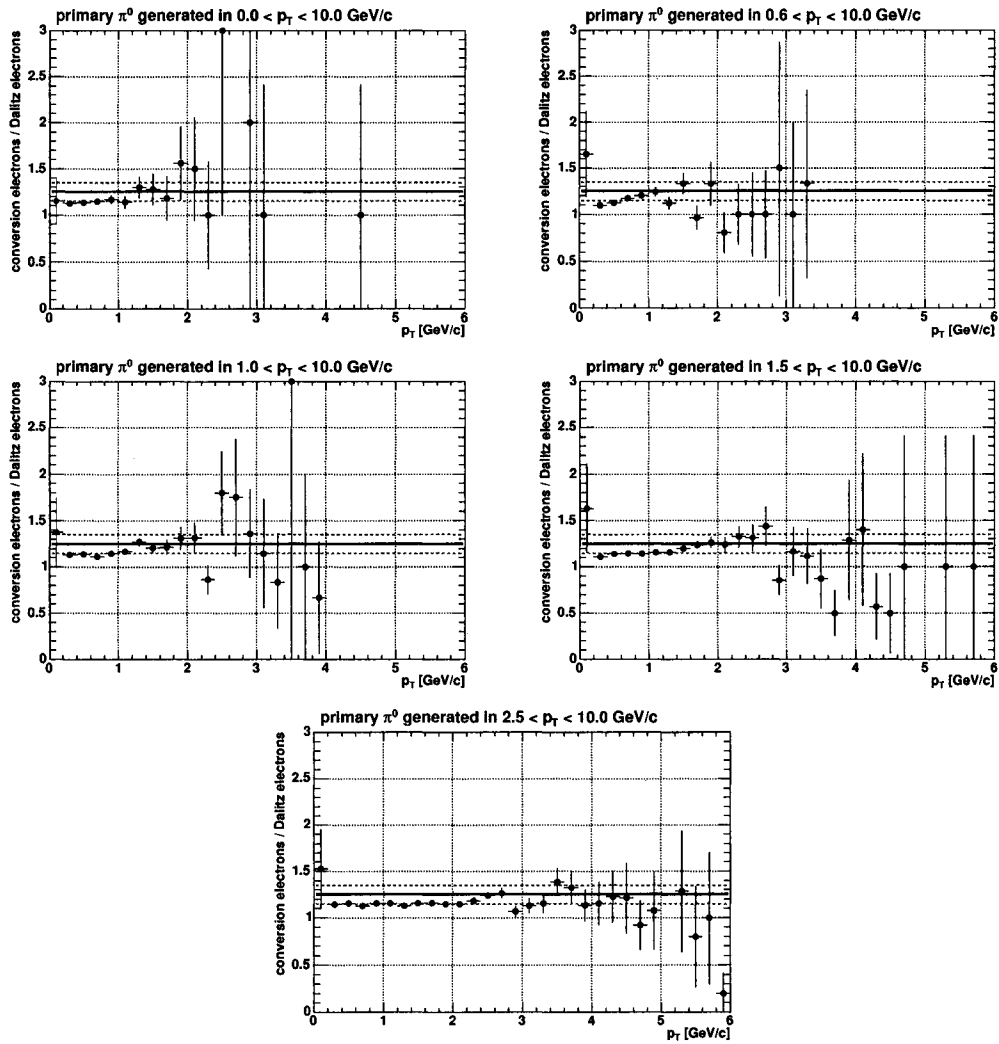


Figure 5.49: Ratio of reconstructed electrons from photon conversions and from Dalitz decays as function of electron p_T for five π^0 simulations using various lower limits on the π^0 p_T . The lines indicate the ratio that is finally adopted for the current cocktail, *i.e.* 1.25 ± 0.10 .

(small) differences in the relative branching ratios into real and virtual photon decay channels, for the decays of heavier mesons.

A full PISA simulation of neutral pions was performed already for the Run-2 configuration of PHENIX in the course of the *converter subtraction* analysis that lead to the publication [68] and which is documented in detail in [62]. Here, we use the eTree files that were generated from the simulation (see [62] for details of the simulation). Since the reconstruction efficiency both for electrons from Dalitz decays and, in particular, from conversions depends on the electron ID cuts, it is important to point out that the ratio *Conv/Dalitz* was determined here for exactly the same electron ID cuts as used in [62, 68] as well as in the corresponding *cocktail subtraction* analysis as documented in [71].

Full π^0 simulations have been performed for [62] with a realistic input p_T distribution⁴. In addition to the *unbiased* simulation, in which primary π^0 have been generated in the range $0 < p_T < 10$ GeV/c, four additional simulation have been performed to increase the statistics at higher p_T . Primary π^0 have been generated in the ranges $p_T^{thresh} < p_T < 10$ GeV/c with p_T^{thresh} values of 0.6, 1.0, 1.5, and 2.5 GeV/c, respectively.

The resulting ratios of conversion electrons and electrons from Dalitz decays are shown in Fig. 5.49. It is interesting to note that all ratios increase slightly at the p_T value that is equal to the threshold value p_T^{thresh} for the parent π^0 used in the respective simulation. This points to a subtle kinematical effect that might bias the ratio of interest for electron p_T value below p_T^{thresh} . Therefore,

⁴Since we are only interested in the ratio of electrons from conversions and Dalitz decays, we are not very sensitive on the exact form of the parameterization.

it seems reasonable to chose

$$\frac{(e^+ + e^-) \text{ from conversion}}{(e^+ + e^-) \text{ from Dalitz}} = 1.25 \pm 0.10 \quad (5.8)$$

as final input for the current cocktail calculation, as indicated by the lines in Fig. 5.49. In accordance with [69] the ratios do not show a significant p_T dependence. By construction, this ratio is consistent with the corresponding conversion rate in Au+Au Run-2 as studied via the *converter subtraction* technique [62, 68].

In addition to the systematic of 8 % associated with the uncertainty in extracting the ratio of conversion electrons to Dalitz electrons from the simulation files (see Eq. 5.8), one has to consider the uncertainty in the material present in the PHENIX acceptance during the Au + Au portion of Run-2. This was studied extensively in [62] via the full reconstruction of e^+e^- pairs from photon conversions both in data and in the simulation. It was shown that the material implemented in the simulation agrees with the material in the experiment within 4.4 %. Adding this uncertainty in quadrature with the value of 8 % quoted above results in a total systematic uncertainty of 9.1 % for the ratio of electrons from conversions and Dalitz decays in the current cocktail.

5.11.5 Weak kaon decays: K_{e3}

Kaons contribute to the inclusive electron spectrum vias their so-called K_{e3} decays, *e.g.* $K_L^0 \rightarrow \pi^\pm e^\mp \nu_e$. Since these are weak decays, the decay electrons do not originate from the primary collision vertex. The resulting momentum

mis-reconstruction can only be treated with via a full GEANT/PISA based simulation. Such a simulation was already performed for the *converter subtraction* analysis [62, 68] of electrons in Run-2 Au + Au collisions, and for the current cocktail we use these results.

Fig. 5.50 shows the invariant spectra of electrons from K_{e3} decays as obtained from the simulations in [62] in various centrality bins from Run-2 Au + Au collisions. The spectra are fit according to the parameterization

$$E \frac{d^3N}{d^3p} = \frac{c}{(p_T + 1.8\text{GeV}/c)^{17}} \quad (5.9)$$

It turns out that the spectral shape does not change as function of centrality. Therefore, Eq. 5.9 is used as parameterization for the K_{e3} input for the current cocktail, with the normalization c corresponding to the values shown in Fig. 5.50.

We assign a conservative systematic uncertainty of 30 % for the K_{e3} contribution to the current cocktail.

5.11.6 Direct radiation

Two contributions from direct radiation to the inclusive electron spectra are currently included in the cocktail:

- conversion of direct real photons, *e.g.* from quark-gluon Compton scattering, in material in the PHENIX acceptance
- direct virtual photons $\gamma^* \rightarrow e^+e^-$

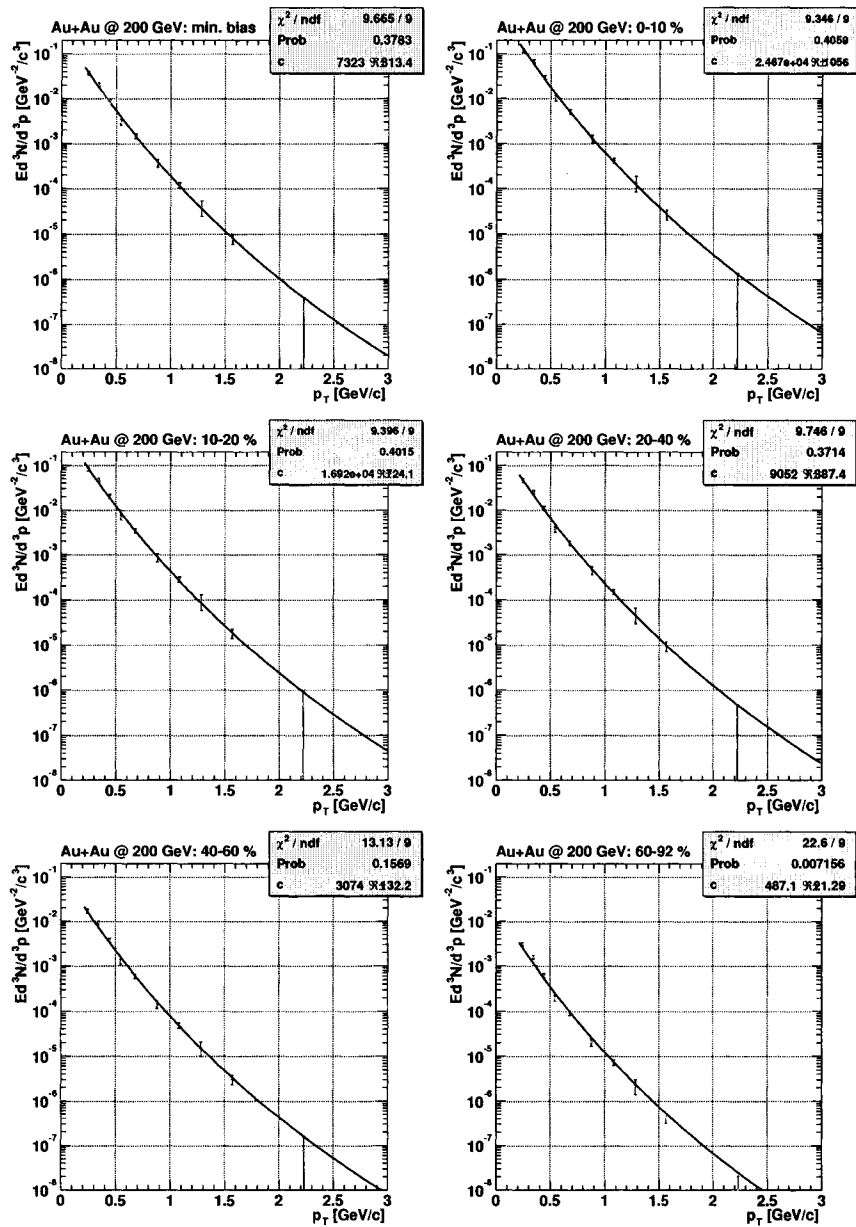


Figure 5.50: Invariant multiplicity distributions of electrons and positrons from K_{e3} decays in various Run-2 Au + Au centrality classes (taken from [62]). The error bars are purely statistical. The lines correspond to fits according to Eq. 5.9.

The relation between these two contributions naturally is about the same as for Dalitz decays of light mesons and the corresponding decays involving a real photon. In both cases, we deal with a source emitting photons that can be either real ($\pi^0 \rightarrow \gamma\gamma$ OR direct photon) or virtual ($\pi^0 \rightarrow \gamma e^+e^-$ OR virtual photon). This similarity allows to implement the contributions from direct radiation into the cocktail via a so-called *direct pion*. This object is defined as a neutral pion with an invariant p_T distribution and normalization chosen such that the spectrum of decays photons (from the standard decay $\pi^0 \rightarrow \gamma\gamma$) is consistent with the spectrum of the expected direct (real) photons. The standard treatment of photon conversions in EXODUS (as the scaled spectrum of electrons from Dalitz decays, as discussed above) will then provide the spectrum of conversions of these direct photons. At the same time, the Dalitz component of these *direct pions* itself will provide an estimate for the contribution from virtual photons. The only small complication one has to deal with is related to the fact that the ratio of virtual to real photons depends on the mass of the parent meson in the standard formalism [72]. The larger the parent mass, the larger the virtual contribution relative to the real one. However, this ratio saturates quickly with increasing parent mass. Therefore, we chose the relative branching ratio of the η meson as a representative case. The approach described here relies on the availability of a paramterization of a pion invariant p_T distribution that results in a decay photon spectrum that is consistent with a realistic direct photon spectrum.

To construct the contributions from direct radiation in all centrality bins for Run-2 Au + Au data and, consistently, for Run-2 p + p data (see [69]), we take the following approach:

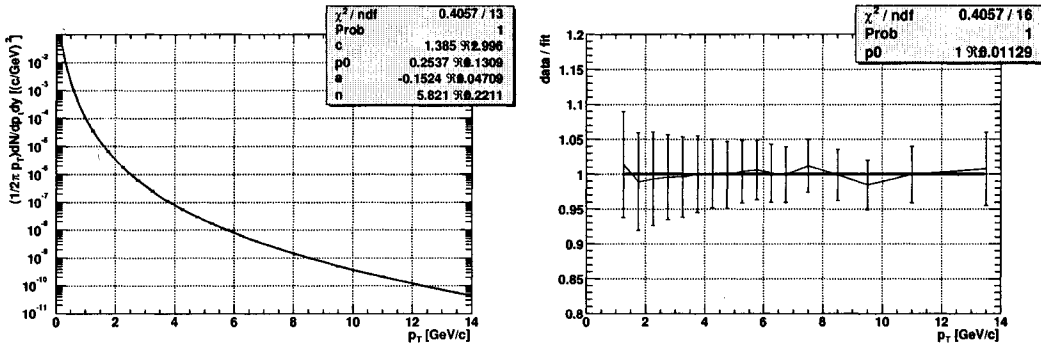


Figure 5.51: Fit to a NLO direct photon calculation [75] with the modified Hagedorn parameterization from Eq. 5.10 (left panel) and ratio of NLO *i.e.* data to the fit (right panel).

1. construct a *direct pion* parameterization that generates a decay spectrum consistent with the Run-2 p + p result for direct photons [73].
2. scale the p + p *direct pion* parameterization to Au + Au with the appropriate number of binary collisions N_{coll} (or nuclear overlap integral T_{AB}) for the various centrality bins taken from [63].

This procedure relies on the assumption that the direct photon spectra scale with N_{coll} from p + p to Au + Au collisions, *i.e.* $R_{AA} = 1$ for direct photons, independent on the Au + Au centrality class. This assumption is very well justified as discussed in [74].

It is shown in [73], that the PHENIX measurement of direct photons in p + p collisions at 200 GeV is consistent, within substantial uncertainties, with an NLO calculation [75]. As demonstrated in Fig. 5.51, the NLO *data* can be parameterized nicely with a modified Hagedorn parameterization

$$E \frac{d^3 N}{d^3 p} = \frac{c}{(\exp(-ap_T) + p_T/p_0)^n} \quad (5.10)$$

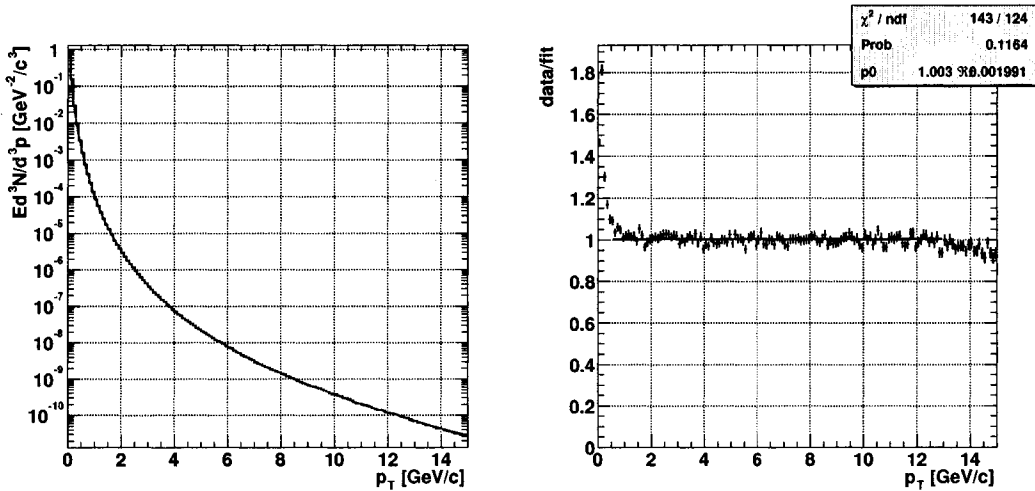


Figure 5.52: Invariant direct photon spectrum from the current $p + p$ cocktail together with the fit (red line) to the NLO input (left panel) and ratio of data to fit (right panel).

where multiplicity N and cross section σ are related via the $p + p$ inelastic cross section of 42.2 mb, *i.e.* $N = \sigma/42.2$ mb.

It should be pointed out that for $p_T < 1.25 \text{ GeV}/\text{c}$, the fit is not supported by any NLO data points but is only extrapolated. Extrapolations of power law fits beyond the range of available data are known to be notoriously unreliable. Given the facts that, on average, direct photons below 1.25 GeV/c yield electrons below 0.7 GeV/c (where the electron measurement gets very difficult anyhow), and that the contribution of direct photons relative to the other sources (mainly neutral pions) at low p_T is tiny, the extrapolation issue is ignored here.

A *direct pion* spectrum that results in a decay photon spectrum consistent with the NLO input is given by

$$E \frac{d^3 N}{d^3 p} = \frac{1}{(\exp(0.1 \times p_T) + p_T/0.34)^{5.89}} \quad (5.11)$$

with the absolute normalization being tied to the neutral pion (as for the treatment of mesons with mass larger than the π^0 in EXODUS). A value of 0.0262 for the ratio *direct pion*/ π^0 results in the direct photon invariant multiplicity distribution shown in the left panel of Fig. 5.52. The ratio of this direct photon spectrum implemented in the current cocktail and the NLO input fit shown in the right panel of Fig. 5.52 demonstrates the excellent quality of the direct photon parameterization for p + p collisions.

This *direct pion* input parameterization is subsequently scaled with the appropriate number of binary collisions N_{coll} (taken from [63]) from p + p to Au + Au collisions in the various centrality bins.

The systematic uncertainty of the direct photon contribution to the cocktail is large. In accordance with the values quoted in [73], we assign a sys. error of 50 % to the direct photon spectrum in p + p. For Au + Au collisions we add the sys. uncertainties in N_{coll} in quadrature to the 50 % error from the p + p baseline.

5.11.7 Electron cocktail

The resulting electron cocktails for various centrality classes in Run-2 Au + Au collisions at 200 GeV are shown in Figs. 5.53, 5.54, and 5.56. ROOT files with the cocktails and corresponding macros to produce the plots can be found at

<http://www.phenix.bnl.gov/WWW/p/draft/ralf/cocktail/auau200/run2/>

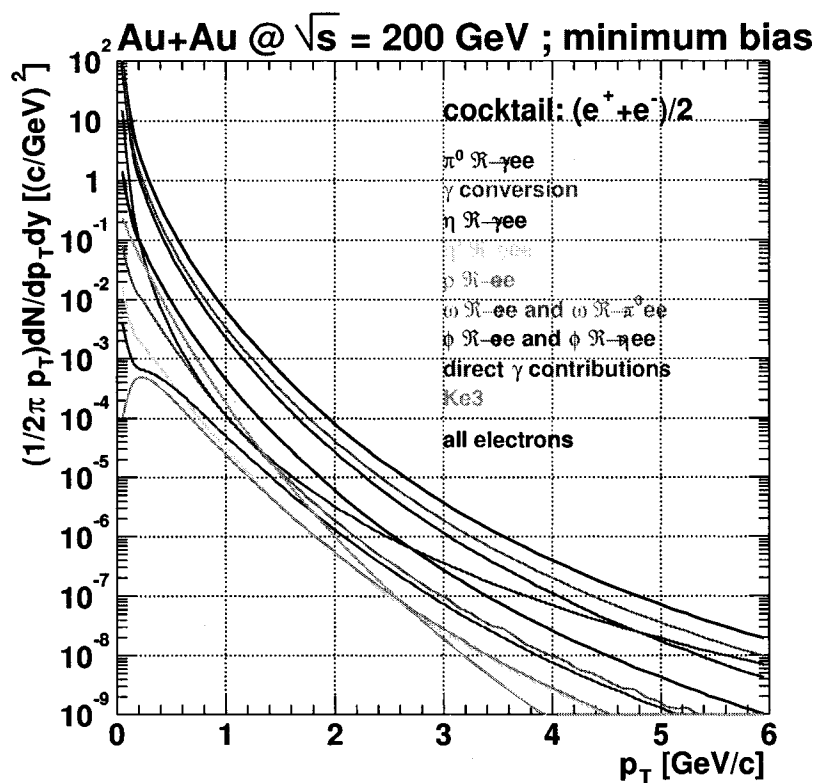


Figure 5.53: Invariant yield of electrons from all implemented sources for minimum bias Au + Au collisions at 200 GeV (Run-2).

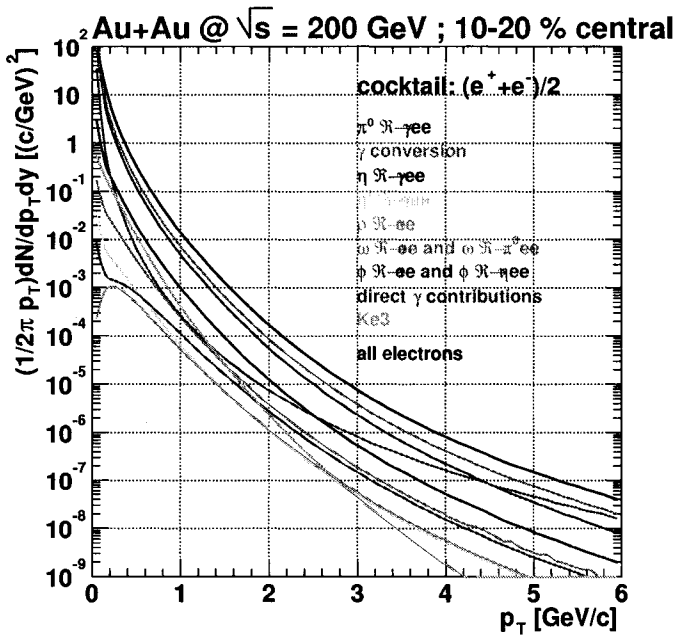
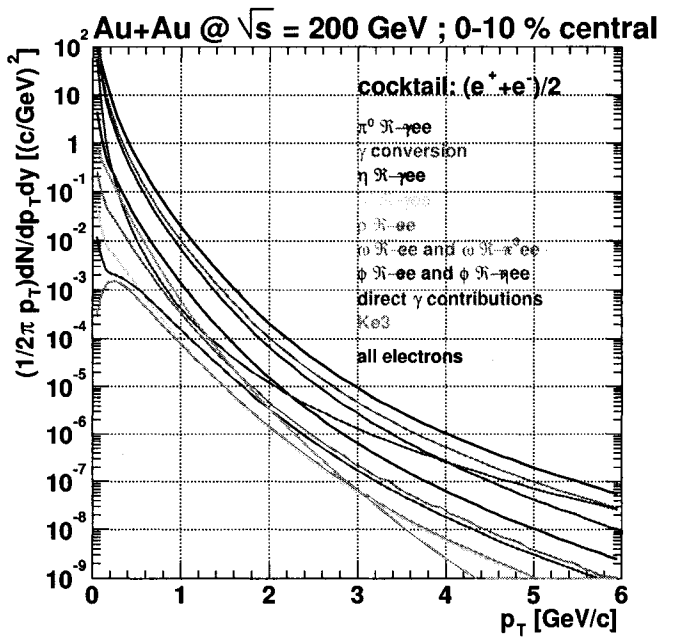


Figure 5.54: Invariant yield of electrons from all implemented sources for 0-10 % central (upper panel) and 10-20 % central (lower panel) $\text{Au} + \text{Au}$ collisions at 200 GeV (Run-2).

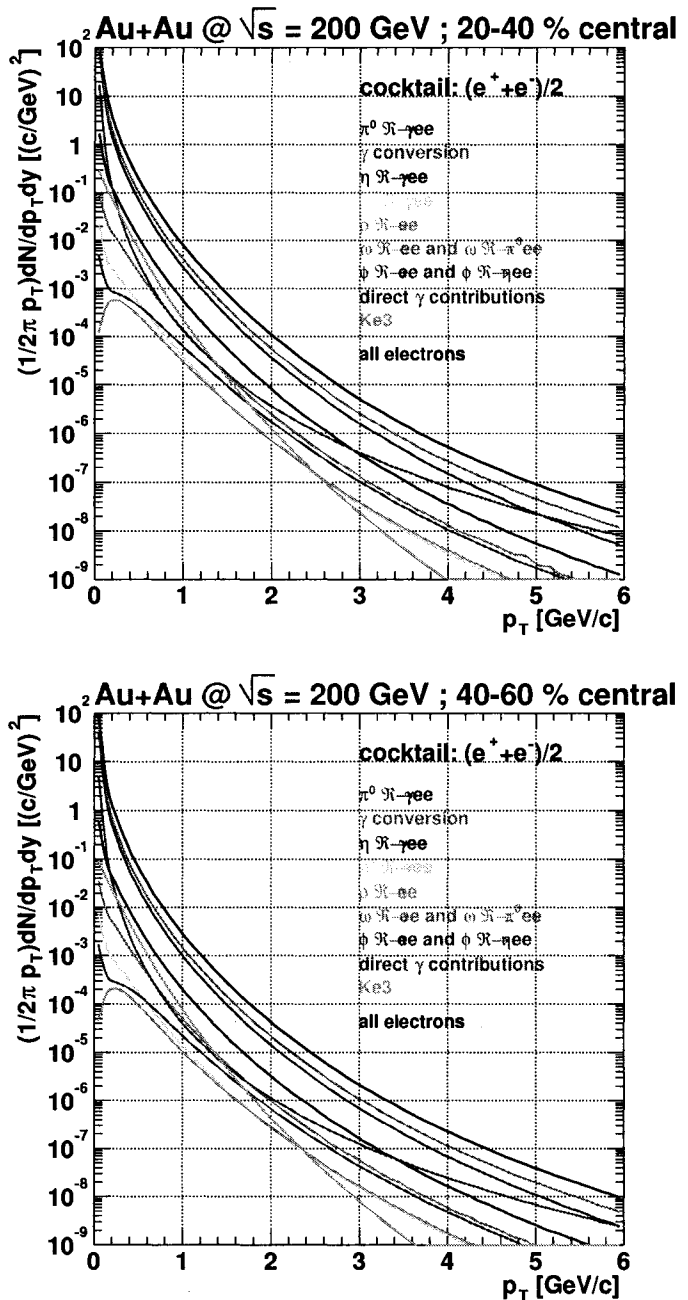


Figure 5.55: Invariant yield of electrons from all implemented sources for 20-40 % central (upper panel) and 40-60 % central (lower panel) Au + Au collisions at 200 GeV (Run-2).

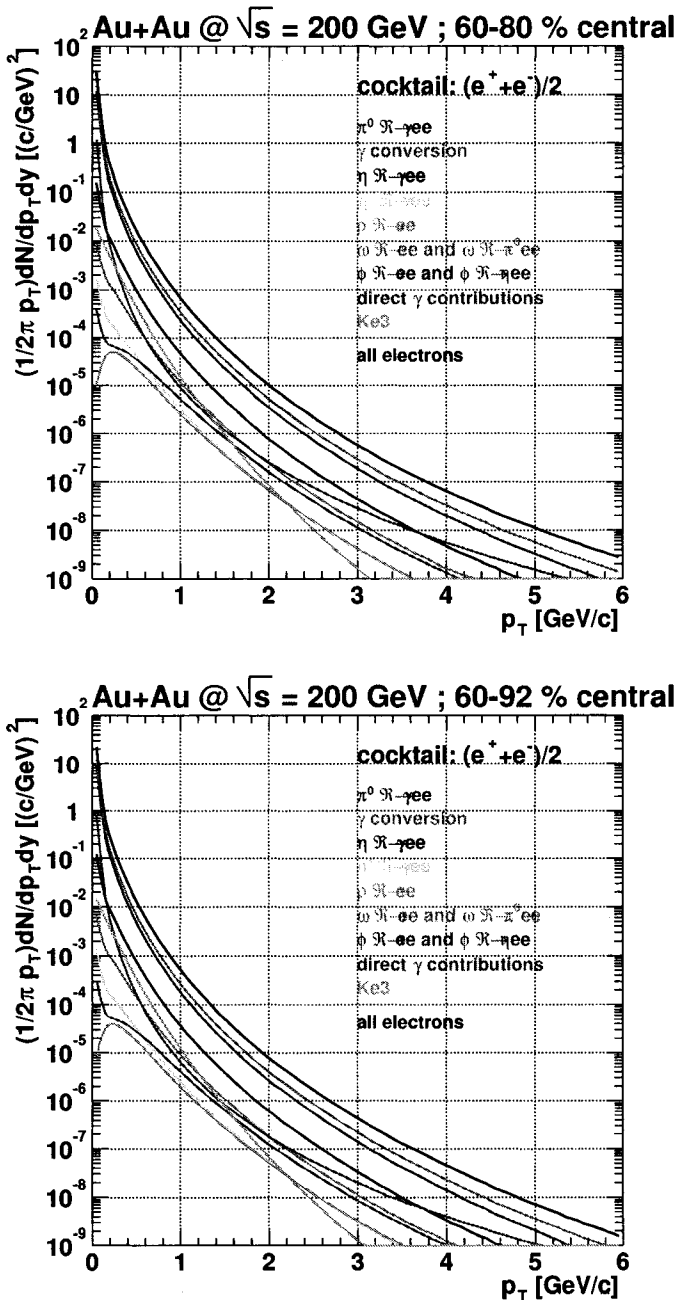


Figure 5.56: Invariant yield of electrons from all implemented sources for 60-80 % central (upper panel) and 60-92 % central (lower panel) Au + Au collisions at 200 GeV (Run-2).

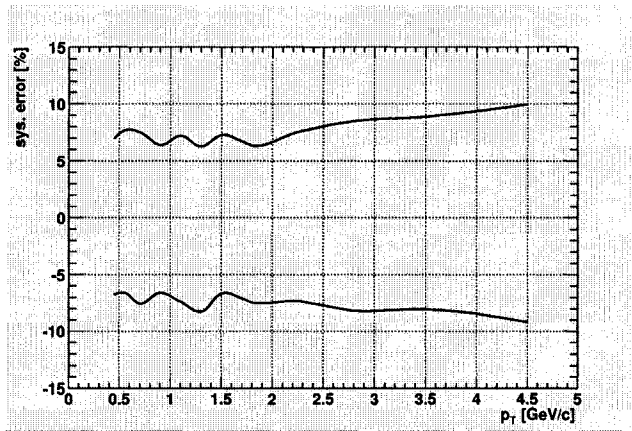


Figure 5.57: Systematic error of the full cocktail due to the uncertainty in the pion input for minimum bias Au + Au collisions at 200 GeV (Run-2). Statistical fluctuation will be smoothed by a fit in the end.

5.11.8 Systematic error estimate

The systematic uncertainties associated with the individual cocktail ingredients were already discussed in the relevant sections above. Here, the various contributions are listed again and it is shown how the sys. errors of the cocktail ingredients are combined into the sys. uncertainty of the full cocktails. The minimum bias case is taken as an example for the discussion of the procedure⁵:

1. The sys. uncertainty of the full cocktail is dominated by the contribution from the uncertainty in the pion input at low and intermediate p_T . It is evaluated by moving the individual data points up/down by their 1σ sys. error, redoing the fit, and rerunning the full cocktail calculation. The difference between these upper/lower 1σ bounds and the optimum cocktail define the sys. error shown in Fig. 5.57. The associated uncertainty rises slightly from low to high p_T .

⁵In the end, the total sys. uncertainties are given for all centrality classes.

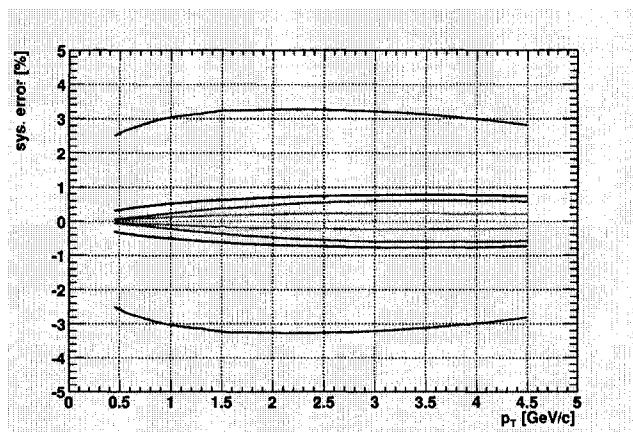


Figure 5.58: Systematic error of the full cocktail due to the uncertainty associated with the decays of other light mesons for minimum bias Au + Au collisions at 200 GeV (Run-2). From top to bottom, the curves correspond to contributions from decays os η (red), ω (blue), ϕ (magenta), and ρ mesons (green).

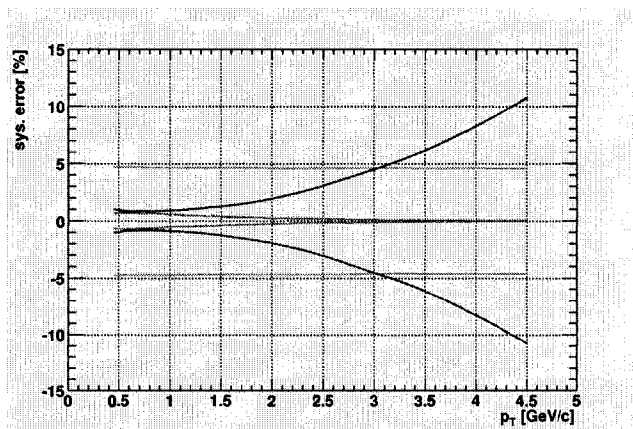


Figure 5.59: Systematic error of the full cocktail due to the uncertainty associated with the contributions from photon conversions (light blue curve at $\approx 4\%$), from K_{e3} decays (green curve approaching zero towards high p_T), and from direct radiation (dark blue curve diverging towards high p_T) for minimum bias Au + Au collisions at 200 GeV (Run-2).

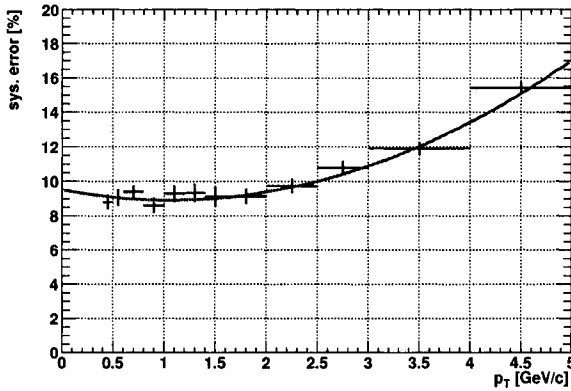


Figure 5.60: Total systematic error of the full cocktail for minimum bias Au + Au collisions at 200 GeV (Run-2) together with a parabola fit.

2. The sys. error associated with the uncertainties in the input from other light meson decays are shown in Fig. 5.58. Note the different vertical scales in Figs. 5.57 and 5.58. Only the η meson is of any relevance.
3. The sys. error associated with the uncertainty in the photon conversion rate is almost constant as function of p_T as demonstrated in Fig. 5.59.
4. The sys. error associated with the contribution from K_{e3} decays is tiny as shown in Fig. 5.59 and relevant at low p_T only, if at all.
5. The sys. error associated with contributions from direct radiation increases with p_T and becomes dominant only at high p_T as demonstrated in Fig. 5.59.

The quadratic sum of these five contributions is plotted in Fig. 5.60 together with a parabolic fit according to

$$\text{sys. error} = (a + b \times p + T + c \times p_T^2)\% \quad (5.12)$$

centrality	a	b [(GeV/c) $^{-1}$]	c [(GeV/c) $^{-2}$]
min. bias	9.5	-1.1	0.52
0 - 10 %	9.9	-1.5	0.73
10 - 20 %	9.7	-1.2	0.57
20 - 40 %	9.1	-0.45	0.37
40 - 60 %	9.0	-0.02	0.25
60 - 80 %	8.8	0.35	0.15
60 - 92 %	8.8	0.23	0.19

Table 5.8: Fit parameters for the total systematic uncertainty of the current cocktails according to Eq. 5.12.

The fit parameters for the total systematic uncertainties of the cocktails for minimum bias collisions as well as for the other centrality classes are summarized in Tab. 5.8.

5.11.9 Comparison with the converter measurement

A cross check of prime importance is to compare the photonic part of the current cocktail, *i.e.* the sum of all contributions except for the decays of kaons K_{e3} and dielectron decays of vector mesons, with the measured spectrum of electrons from photonic sources from the converter subtraction analysis [62]. While tabulated values for the photonic part of the inclusive electron spectrum are not officially documented, the corresponding spectra have been provided by T. Hachiya in a private communication. Since these available invariant spectra are not bin-width corrected it is important to compare them with the photonic cocktail spectrum using the same binning, such that the bin-width correction cancels in the ratio.

The ratios of measured photonic electron spectra and the photonic part of

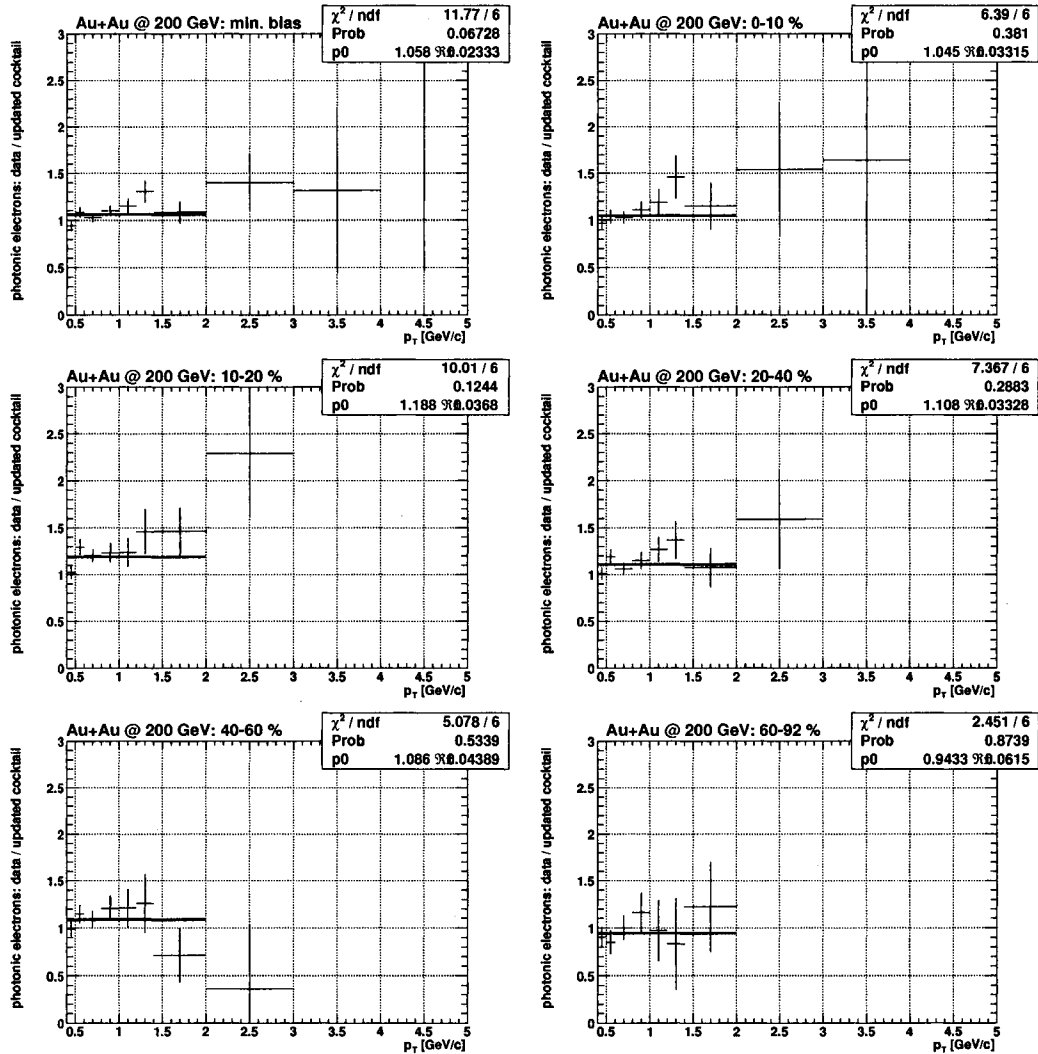


Figure 5.61: Ratios of measured electron spectra from photonic sources (from Ref. [62]) and the photonic part of the current cocktail as function of p_T for all available centrality classes. All ratios are fit with a constant for $p_T < 2$ GeV/c.

the cocktail are shown as function of p_T for all available centrality classes in Fig. 5.61. The ratios are fit with a constant in the range $p_T < 2 \text{ GeV}/c$. While all ratios, except for the one for the most peripheral collisions, are slightly larger than unity by $\approx 10\%$, this deviation from one is not significant, given the sys. uncertainties of the cocktail and the photonic electron spectra, which both are in the order of 10 %. It is important to point out that a photonic ratio data/cocktail significantly larger than unity would imply the presence of a photonic electron source currently not implemented in the cocktail. Thermal radiation would be such a source, and contributions to the photonic electron spectra on the level of a few percent are actually not unexpected. In principle, the ratios shown in Fig. 5.61 allow to determine an upper limit for thermal photon production in 200 GeV Au+Au collisions.

5.12 p_T Spectra Of Electrons From Non-Photonic Sources

For all centrality classes, we subtract the corresponding cocktail from the inclusive electron spectrum point by point. The resulting non-photonic p_T spectra are shown in Figs. 5.62 - 5.67. The data from the present analysis are labeled *Cocktail*. The data points labeled *Converter* are the final published results from [68], which are shown for comparison. Apparently, the two analyses agree very nicely. Since the two analyses do not use the same binning⁶, we can't calculate a point-by-point ratio. To allow for a more quantitative com-

⁶The binning of the spectra in the current analysis was chosen to be the same as used in the p + p analysis [14], such that the nuclear modification factor R_{AA} can be calculated point-by-point.

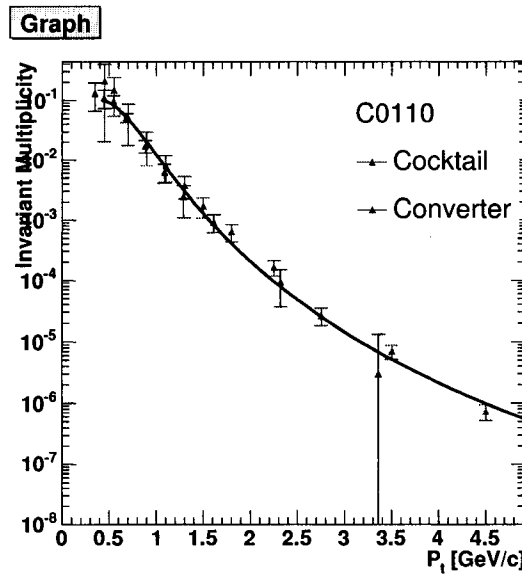


Figure 5.62: Overlay of Non-Photonic spectra from converter and the cocktail analysis for 00 - 10 % in centrality. Also shown is a fit resulting from fitting to the combination of both spectra according to Eq. 5.13.

parison of the two data sets, we therefore fit both sets simultaneously with the following functional form:

$$\frac{1}{2\pi p_T} \frac{dN}{dp_T dy} = \frac{c}{e^{-ap_T} + \frac{b}{p_T}^n}. \quad (5.13)$$

The fits are shown as solid curves in Figs. 5.62 - 5.67. We then divide both data sets by the fit and plot the ratio as function of p_T in Figs. 5.68 - 5.73. The ratio plots confirm the good agreement of the two data sets and emphasize again the strengths of the two methods. The converter analysis results in a superior measurement at low p_T , whereas towards high p_T the non-photonic electron spectra currently can only be measured with reasonable precision using the cocktail method.

Graph

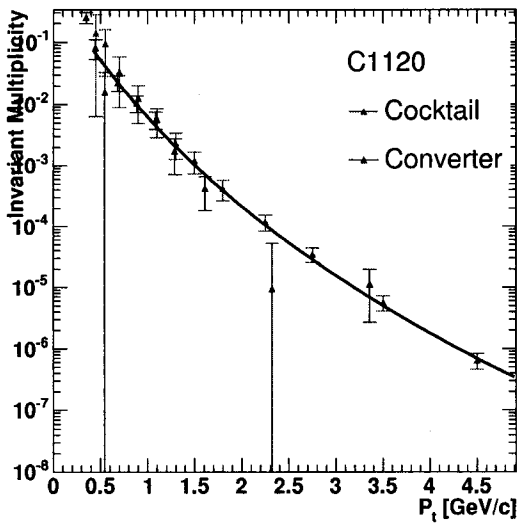


Figure 5.63: Overlay of Non-Photonic spectra from converter and the cocktail analysis for 10 - 20 % in centrality. Also shown is a fit resulting from fitting to the combination of both spectra according to Eq. 5.13.

Graph

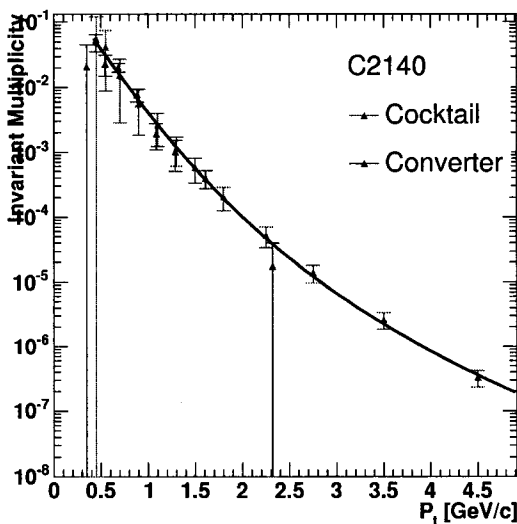


Figure 5.64: Overlay of Non-Photonic spectra from converter and the cocktail analysis for 20 - 40 % in centrality. Also shown is a fit resulting from fitting to the combination of both spectra according to Eq. 5.13.

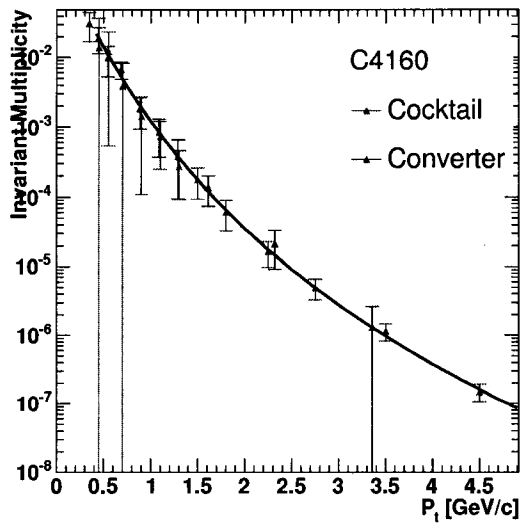
Graph

Figure 5.65: Overlay of Non-Photonic spectra from converter and the cocktail analysis for 40 - 60 % in centrality. Also shown is a fit resulting from fitting to the combination of both spectra according to Eq. 5.13.

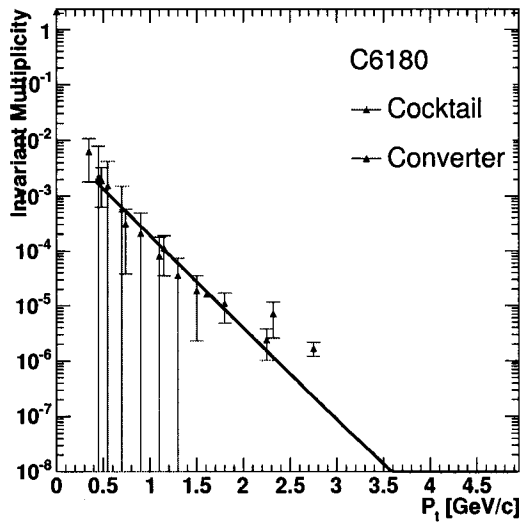
Graph

Figure 5.66: Overlay of Non-Photonic spectra from converter and the cocktail analysis for 60 - 80 % in centrality. Also shown is a fit resulting from fitting to the combination of both spectra according to Eq. 5.13.

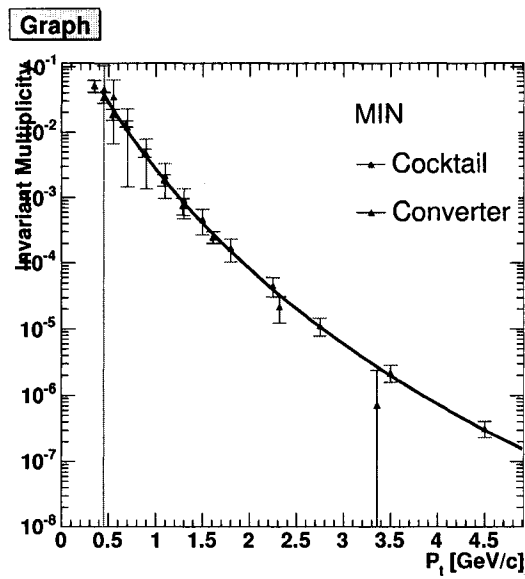


Figure 5.67: Overlay of Non-Photonic spectra from converter and the cocktail analysis for minimum bias. Also shown is a fit resulting from fitting to the combination of both spectra.

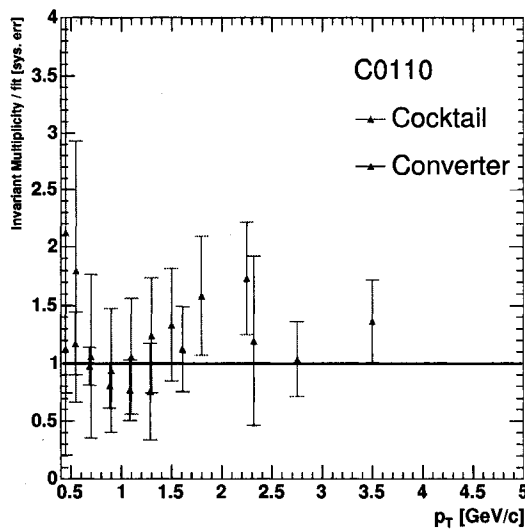


Figure 5.68: Ratio of Non-Photonic spectra to the merged fit P_T spectra for 0-10% centrality overlayed with the same spectrum from converter. The fit results from fitting to the combination of both spectra according to Eq. 5.13.

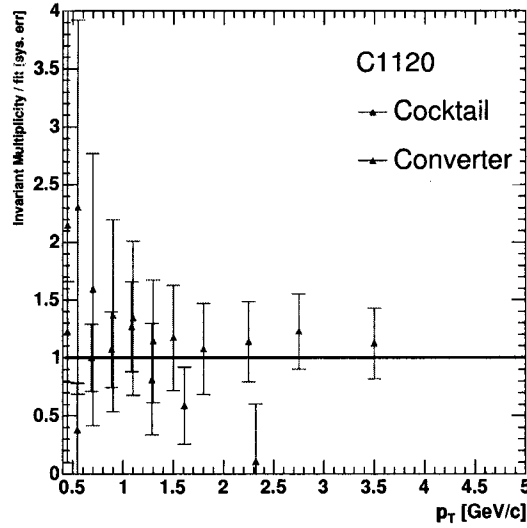


Figure 5.69: Ratio of Non-Photonic spectra to the merged fit P_T spectra for 10-20% centrality overlayed with the same spectrum from converter. The fit results from fitting to the combination of both spectra according to Eq. 5.13.

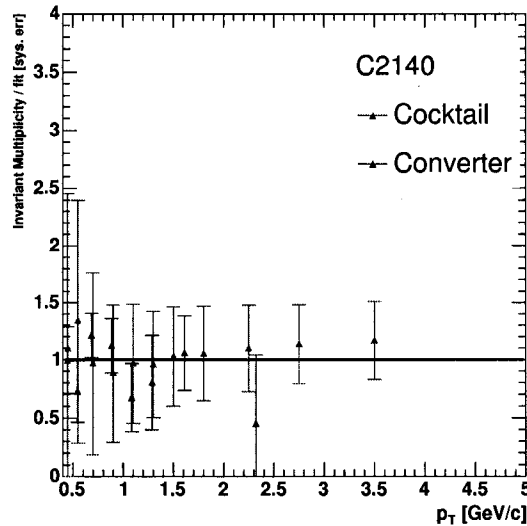


Figure 5.70: Ratio of Non-Photonic spectra to the merged fit P_T spectra for 20-40% centrality overlayed with the same spectrum from converter. The fit results from fitting to the combination of both spectra according to Eq. 5.13.

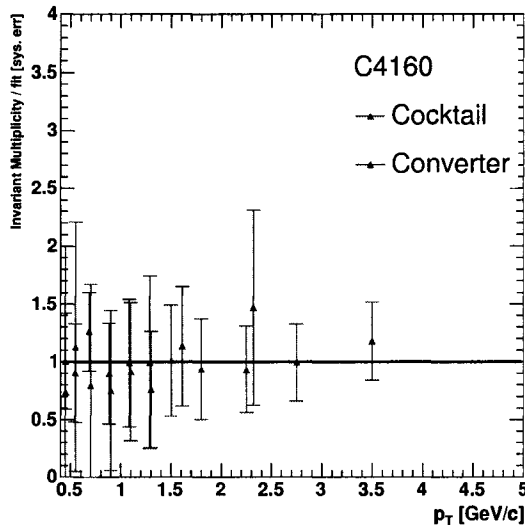


Figure 5.71: Ratio of Non-Photonic spectra to the merged fit P_T spectra for 40-60% centrality overlayed with the same spectrum from converter. The fit results from fitting to the combination of both spectra according to Eq. 5.13.

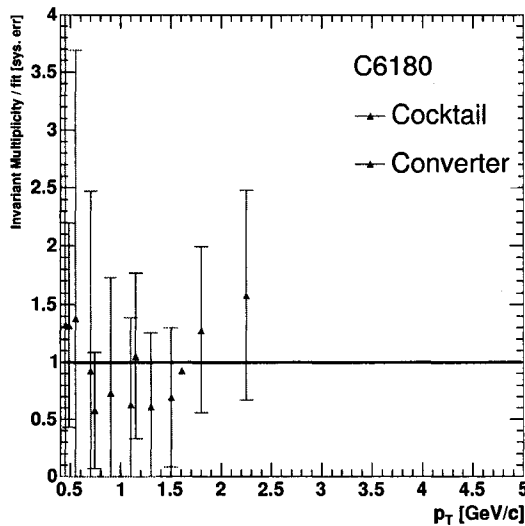


Figure 5.72: Ratio of Non-Photonic spectra to the merged fit P_T spectra for 60-80% centrality overlayed with the same spectrum from converter. The fit results from fitting to the combination of both spectra according to Eq. 5.13.

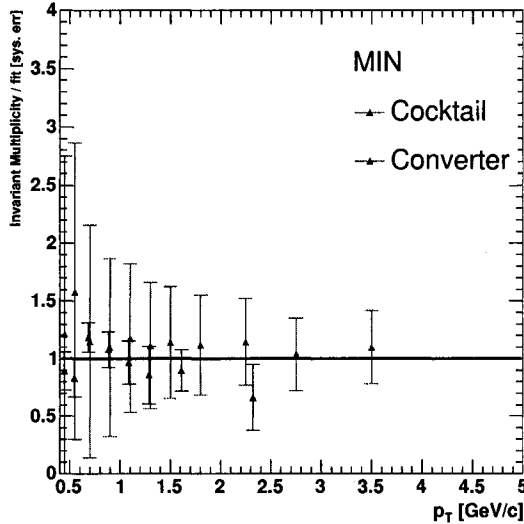


Figure 5.73: Ratio of Non-Photonic spectra to the merged fit p_T spectra for Minimum Bias overlayed with the same spectrum from converter. The fit results from fitting to the combination of both spectra according to Eq. 5.13.

5.12.1 Bin Shift Correction

Due to the width of the binning and the non-constant and steeply falling nature of the true distributions being represented by our histograms, the expected value of p_T for each bin in the distributions is shifted with respect to the center point [43]. To correct for this the following procedure was employed:

- Fit the data using the form given in Eq. 5.13.
- Find the expected p_T where the function takes on its mean value in the given p_T bin by solving

$$f(p_T) = \frac{\int_a^b f(p_T) dp_T}{b - a} \quad (5.14)$$

for p_T .

- Move the data points to their corrected values found in the previous step.
- Repeat the above steps iteratively until the expected value of p_T no longer changes significantly from iteration to iteration. In practice, this takes 5-10 iterations.
- Once the procedure has converged, move the points to their final locations defined by

$$y' = y \frac{f(\frac{b-a}{2})}{\langle p_T \rangle} \quad (5.15)$$

$$\delta y' = \delta y \frac{f(\frac{b-a}{2})}{\langle p_T \rangle} \quad (5.16)$$

All the non-photonic spectra shown have been bin shift corrected in this way.

5.12.2 Binary Scaling Of Non-Photonic Electron Yields

The main result of [68] is the observation of *binary scaling* of the non-photonic electron yields, *i.e.* the integral of the electron spectra is proportional to the number of binary collisions in a given Au-Au centrality bin.

As was done for [68], we calculate the integrated electron yields in the range $0.8 < p_T < 4.0$ GeV/c, divide this by the corresponding number of binary collisions N_{bin} in that centrality class, and plot the resulting ratio as a function of N_{bin} in Fig. 5.74 together with the published measurement from

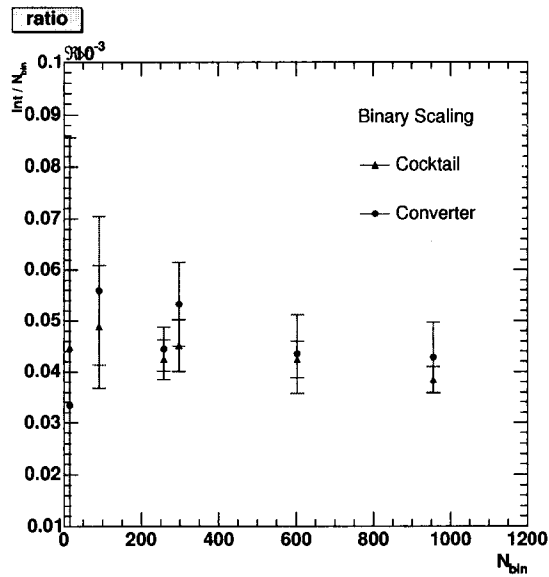


Figure 5.74: Integrals of the p_T spectra from each centrality, divided by N_{bin} as a function of N_{bin} from the present analysis and from [68].

[68]. The error bars shown are purely statistical. As expected already from the direct comparison of the non-photonic spectra presented above, the current analysis is in good agreement with [68].

5.13 Non-Photonic Electron R_{AA}

We calculate the nuclear modification factors R_{AA} for non-photonic electrons by dividing the corresponding invariant p_T spectra obtained in the present analysis by the reference measurement from [14] shown in Fig. 5.75. The p + p reference was scaled by the appropriate nuclear overlap integral T_{AB} , which we take from [16].

The resulting plots of R_{AA} from non photonic electron sources is shown for the various centrality classes in Fig. 5.76. In each plot, the error bars (elec-

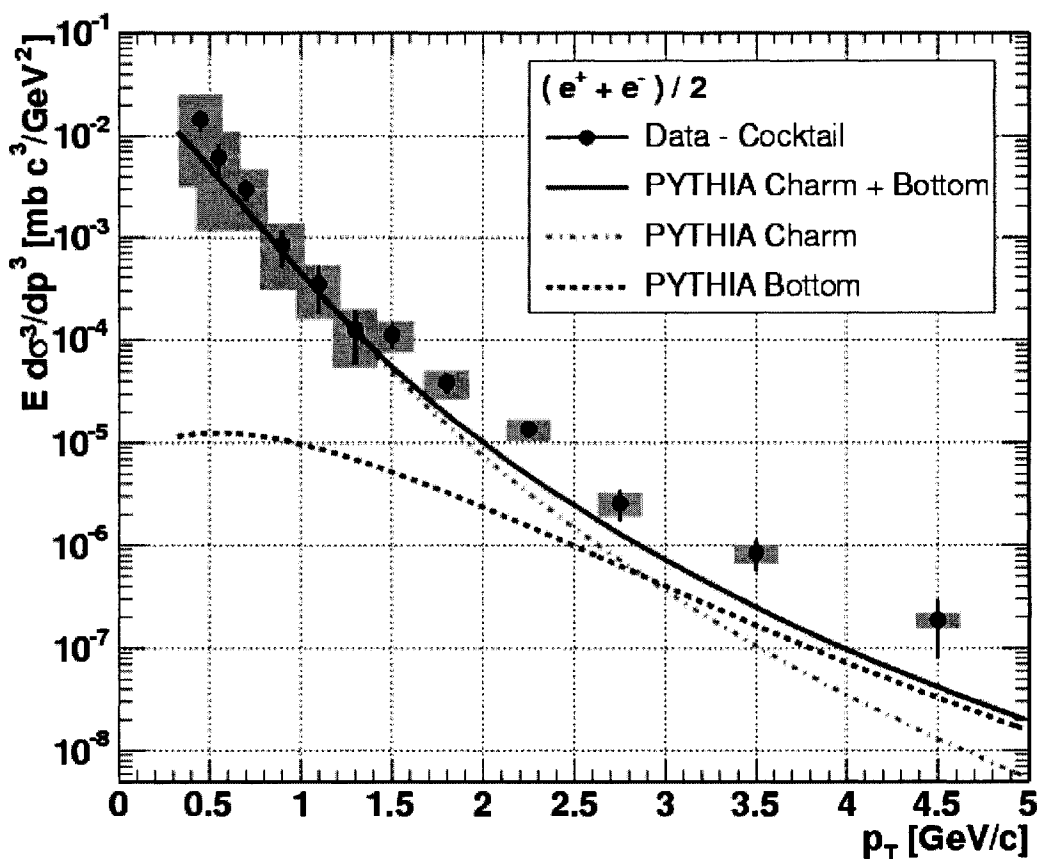


Figure 5.75: Reference spectrum of electrons from $p + p$ collisions taken from [14]. Also shown are the predicted contributions from charm and beauty.

tronic version: black) denote statistical errors, the boxes (electronic version: grey) denote systematic errors, and the bands centered around one (electronic version: blue) represent the p_T independent errors associated with T_{ab} . In central and mid-central collisions a clear suppression of electrons from non-photonic sources is observed at high p_T , consistent with the notion of energy loss of heavy quarks in the hot and dense medium created in Au-Au collisions at RHIC.

Data tables can be found in Sec. A at the end of this thesis.

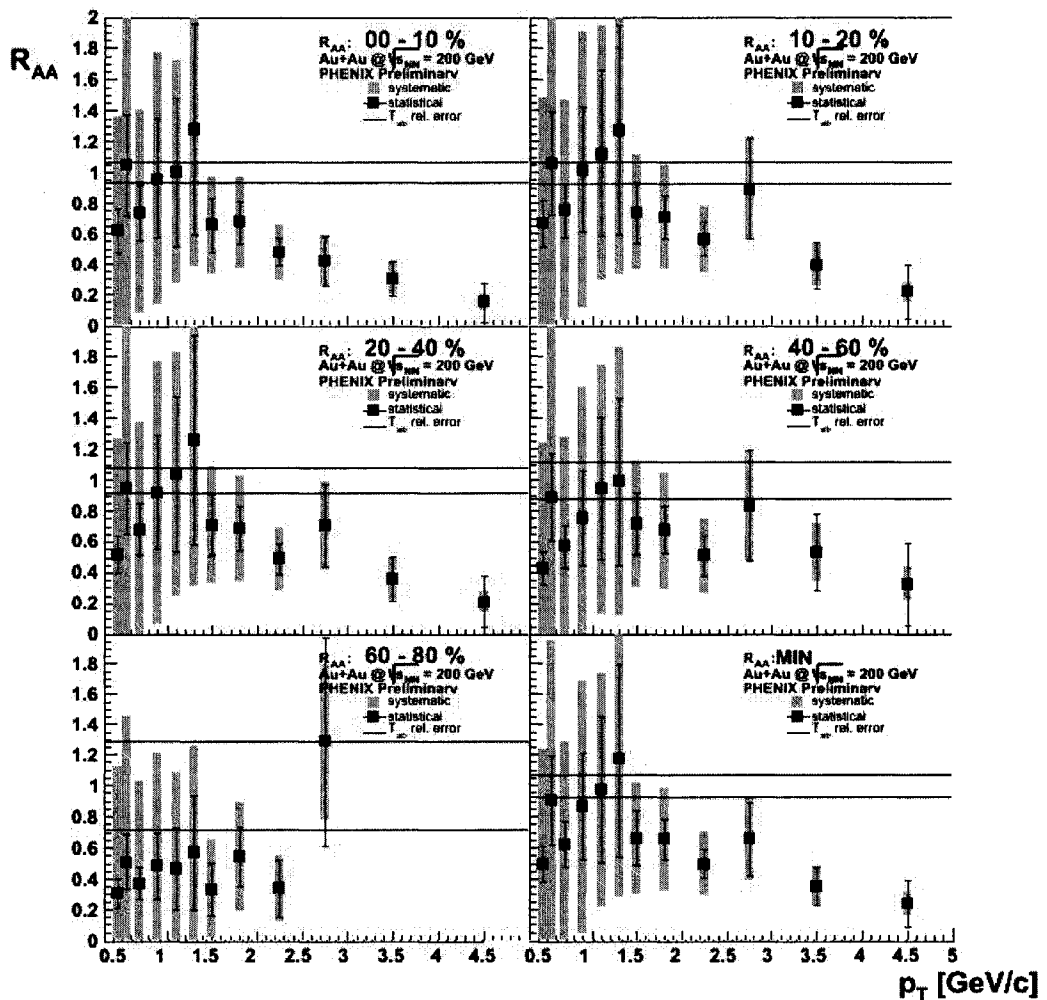


Figure 5.76: R_{AA} by Centrality for non-photonic electrons. Suppression is clearly seen at high p_T where the data falls below unity, indicating the presence of a medium. Systematic errors are large at low p_T so we can not make any statement there about a possible nuclear modification.

5.14 Integrated R_{AA}

5.14.1 Definition of Integrated R_{AA}

In order to investigate the centrality dependence of the observed suppression of electrons from heavy-flavor decays at high p_T , we calculate the R_{AA} over a larger range by combining several p_T bins. We define the integrated quantity $R_{AA}^{p_T^{low}-p_T^{high}}$ as

$$R_{AA}^{p_T^{low}-p_T^{high}} = \frac{\int_{p_T^{low}}^{p_T^{high}} \frac{d^2N}{dp_T dy} dp_T}{T_{AB} \int_{p_T^{low}}^{p_T^{high}} 2\pi p_T \frac{d^3\sigma}{d^3p} dp_T}, \quad (5.17)$$

where $\frac{d^2N}{dp_T dy}$ is the transverse momentum distribution of electrons from heavy-flavor decays measured in Au-Au collisions (in a given centrality bin), and $\frac{d^3\sigma}{d^3p}$ is the corresponding invariant cross section measured in p-p (from [14]).

For p_T^{high} , we chose 5.0 GeV/c. p_T^{low} is varied from 2.0 to 3.0 GeV/c, *i.e.* we calculate $R_{AA}^{2.0-5.0}$, $R_{AA}^{2.5-5.0}$, and $R_{AA}^{3.0-5.0}$ for all centrality bins except for the 60-80 % central bin, where the available p_T reach does not allow for a calculation of $R_{AA}^{p_T^{low}-p_T^{high}}$. Technically, the calculation is not carried out as an integration, but by summing the corresponding high p_T bins.

5.14.2 Treatment of Uncertainties

Since we are interested in the centrality dependence of the integrated R_{AA} , we separate the uncertainties in $R_{AA}^{p_T^{low}-p_T^{high}}$ in three classes

1. Uncertainties that are centrality independent. These uncertainties affect

$R_{AA}^{p_T^{low}-p_T^{high}}$ in all centrality bins in the same way and, therefore, should not be taken into account when judging the centrality dependence. Most uncertainties do fall into this category. We consider the following uncertainties as centrality independent:

- the total uncertainty in the p-p reference integral (stat. and systematic uncertainty),
- all systematic uncertainties on the inclusive electron spectra in Au-Au (except for the uncertainty associated with the multiplicity dependent efficiency loss (embedding correction)). Neither the active area (needed for normalization) nor the matching and electron identification cuts vary with centrality, and
- the systematic uncertainty in the cocktail related with the material in the PHENIX acceptance (needed for the calculation for photon conversions).

2. Systematic uncertainties which vary point-by-point in centrality. Here, we consider:

- the uncertainty associated with the multiplicity dependent efficiency loss (embedding correction),
- all systematic uncertainties in the cocktail except for the systematic related with the material in PHENIX. It should be possible to separate out further cocktail systematics that are not strictly centrality dependent. However, since at high p_T the ratio of inclusive electron spectra to cocktail is large, not much can be gained by

Table 5.9: Integrated nuclear modification factors $R_{AA}^{2.0-5.0}$, $R_{AA}^{2.5-5.0}$, and $R_{AA}^{3.0-5.0}$ with stat. uncertainty σ_{stat} , centrality dependent systematic uncertainty σ_{sys}^{cent} , and centrality independent systematic uncertainty σ_{sys}^{nocent} .

Centrality Class	$R_{AA}^{2.0-5.0}$	σ_{stat}	σ_{sys}^{cent}	σ_{sys}^{nocent}
Min. Bias	0.494	0.020	0.085	0.195
00 - 10 %	0.434	0.029	0.066	0.163
10 - 20 %	0.576	0.040	0.096	0.216
20 - 40 %	0.498	0.039	0.091	0.200
40 - 60 %	0.557	0.073	0.115	0.240
Centrality Class	$R_{AA}^{2.5-5.0}$	σ_{stat}	σ_{sys}^{cent}	σ_{sys}^{nocent}
Min. Bias	0.488	0.033	0.078	0.204
00 - 10 %	0.342	0.046	0.054	0.142
10 - 20 %	0.610	0.068	0.093	0.244
20 - 40 %	0.512	0.066	0.084	0.215
40 - 60 %	0.654	0.127	0.116	0.284
Centrality Class	$R_{AA}^{3.0-5.0}$	σ_{stat}	σ_{sys}^{cent}	σ_{sys}^{nocent}
Min. Bias	0.329	0.035	0.050	0.142
00 - 10 %	0.271	0.053	0.038	0.114
10 - 20 %	0.352	0.071	0.055	0.148
20 - 40 %	0.330	0.069	0.053	0.143
40 - 60 %	0.485	0.143	0.080	0.213

minimizing the centrality dependent cocktail systematics, and

- the systematic uncertainty of the nuclear overlap integral T_{AB} .

3. the statistical uncertainty of the measurement in Au-Au

These three uncertainty classes are propagated independently from each other into the corresponding uncertainties on $R_{AA}^{p_T^{low}-p_T^{high}}$.

5.14.3 Results

The resulting integrated R_{AA} values are tabulated in Tab. 5.9 and plotted as function of the average number of participants in each centrality bin in

Fig. 5.77. For comparison, we overlay $R_{AA}^{2.5-5.0}$ from neutral pions⁷ (from [17]).

This comparison is mainly to guide the eye, since correctly one should compare R_{AA} of pions in a given p_T bin with the R_{AA} of D mesons (not electrons from D mesons) in the same p_T bin. The relation between the decay electron p_T distribution and the one of the parent mesons can be determined only in a model dependent way. Furthermore, the situation gets more complicated given the significant contribution of bottom decays in the highest p_T bins. This unfolding procedure is an important step in a future analysis.

In order to judge quantitatively, whether integrated R_{AA} plots shown in Fig. 5.77 reveal a centrality dependence, we fit the data (after adding the statistical and point-by-point systematic errors in quadrature) with a constant and calculate the χ^2 . We find $\chi^2/\text{ndf} = 1.53/3$, $5.97/3$, and $1.72/3$ for constant fits to $R_{AA}^{2.0-5.0}$, $R_{AA}^{2.5-5.0}$, and $R_{AA}^{3.0-5.0}$, respectively, indicating that the present data do not support the claim of a significant centrality dependence of the observed suppression at high p_T . It is no surprise that fits with linear functions give better χ^2 and indicate a stronger suppression in more central collisions as is also observed for neutral pions.

⁷we have added the quoted systematic errors on the integrated R_{AA} and the separately quoted error on T_{AA} in quadrature to calculate $\sigma_{\text{sys}}^{\text{cent}}$. $\sigma_{\text{sys}}^{\text{nocent}}$ is given by an overall uncertainty of 10 % on the p-p normalization.

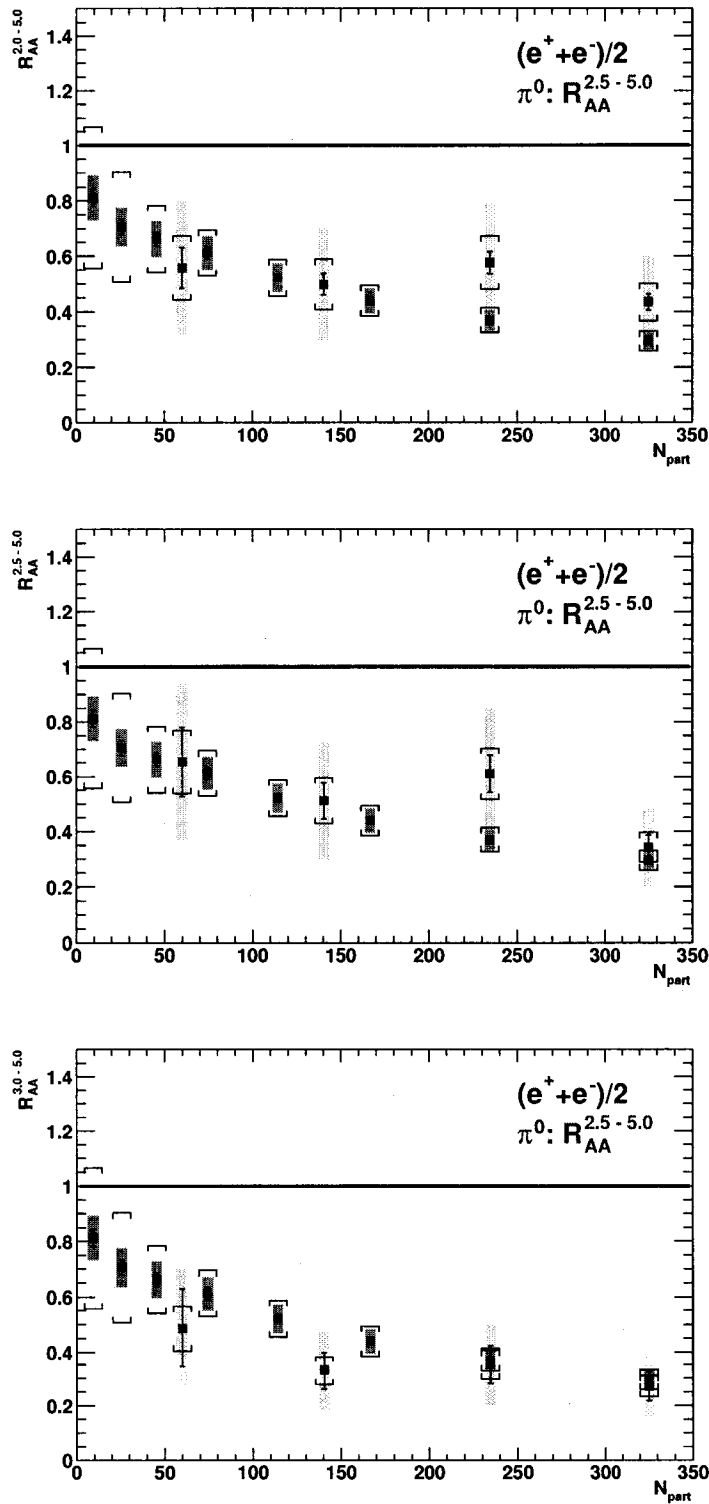


Figure 5.77: Integrated R_{AA} as function of N_{part} for three values of p_T^{low} : 2.0 GeV/c (upper panel), 2.5 GeV/c (middle panel), and 3.0 GeV/c (lower panel). Error bars are statistical only, brackets are point-by-point systematics, and boxes are centrality independent systematics. For (unfair) comparison (see text), we overlay $R_{AA}^{2.5-5.0}$ of neutral pions (from [17]).

Chapter 6

Comparison to Theory and Conclusions

6.1 Central Collisions

In Fig. 6.1, theoretical predictions for R_{AA} of single-electrons from charm decays in the 10% most central collisions are overlayed with the data. Four curves are present in the plot. The upper-most and the two bottom most curves (electronic version: upper - black, lower - blue) come from [38] and the second curve from the top (electronic version: magenta) is from [41].

The three curves from [38] represent different values of \hat{q} which denotes the average squared transverse momentum transferred from the medium to the hard scattered parton per unit path length. As discussed in 2.2.1, \hat{q} is a transport coefficient that characterizes the medium. One thinks of this as a measure of how much energy a quark will lose to the medium as it passes through. The larger \hat{q} gets, the larger the loss of energy and a \hat{q} of zero is interpreted within this model as no energy loss what so ever. The values for \hat{q} were chosen to be consistent with current measurements so the same values were used here as well [39] [40].

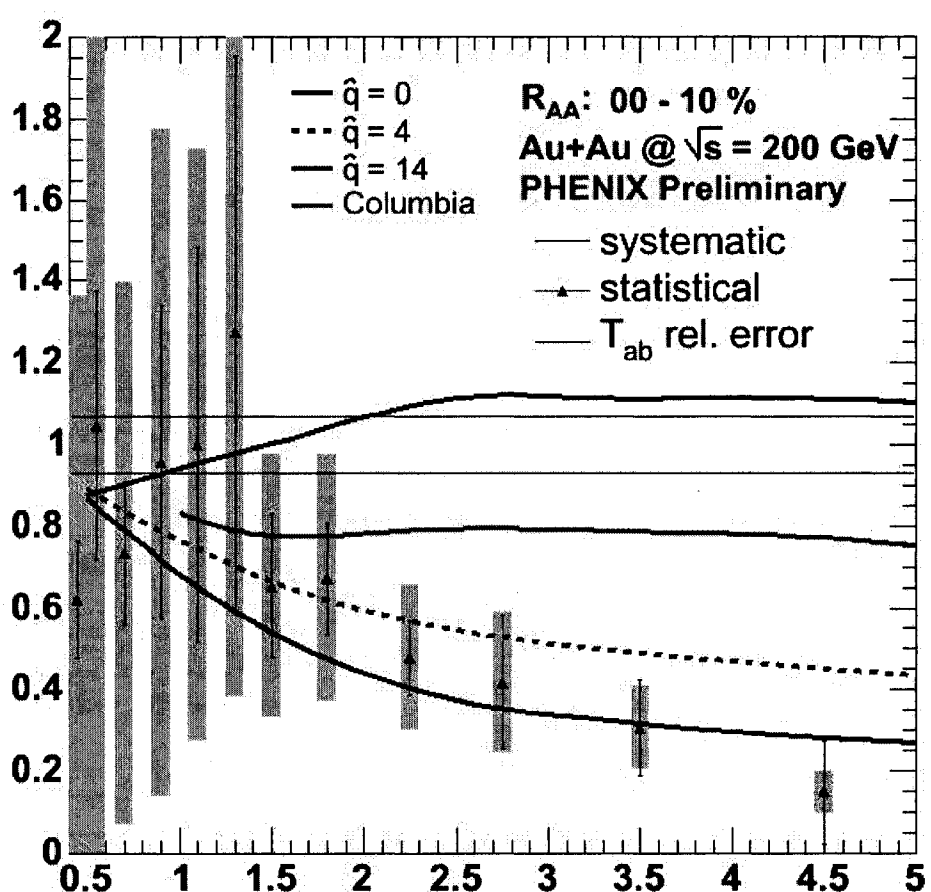


Figure 6.1: Theoretical predictions for R_{AA} overlaid with the data of this thesis for the 10% most central collisions.

All curves are consistent with the data below 2 GeV/c. The systematic errors in the measurement (represented by the boxes) don't allow us to say much. Above 2 GeV/c, we have a different story. It appears that both non-zero values of \hat{q} from [38] are consistent with the data. The calculation from [41] does not reproduce the data at high p_T . It must be pointed out that each of these theory curves does *not* contain any contribution due to bottom. Our current understanding is that at some point around 4.5 GeV/c, the bottom production will turn on and start to contribute, causing the R_{AA} to rise.

6.2 Considerations

6.2.1 The Theoretical Point Of View

To shore up some meaning, I will first gather up in one place those points that I believe all theorists working in this field right now would consider important for any interpretation. In some way, each of the following items must be reconciled within any interpretation of the measured nuclear modification factors.

- **High p_T partons are expected to suffer a significant medium-induced energy degradation prior to hadronization in the vacuum.**

This is the basis for the entire measurement detailed in this thesis. Taken at face value, it is our current best explanation for what is happening when we observe suppression. Other possible explanations exist but none are so simple and so consistent in the context of the current measurements.

- Elliptic flow should be present and smaller for heavy quarks (charm and bottom) as compared to the flow associated with the lighter up and down quarks.

This statement is very intuitive and highlights our common sense expectations about what is happening within any medium we create. Any suppression that we observe in the R_{AA} should be consistent with our notion of flow. If the R_{AA} falls below unity, and it does so very clearly at high p_T in our most central collisions, then we think of this as being caused by an interaction between the quarks and the medium that was created.

In short, there should be a flow. Furthermore as the next bullet points out, we naively expect a flow that will be consistent and reasonable with respect to any observed flow of pions.

- The relative yields of identified high p_T hadrons will test the prediction that medium-induced parton energy loss depends on the identity of the parent parton.

Hard gluons lose more energy than hard quarks due to the stronger coupling to the medium, and the energy loss of massive quarks is further reduced due to the mass-dependent restriction of the phase space into which medium-induced gluon radiation can take place. This is a fancy way of saying we understood the dead cone effect and if it really exists, it will manifest itself in the R_{AA} .

- Recent data from RHIC show that gluon jet quenching is present.

The presence of jet quenching is very strong evidence favoring the presence of an sQGP. Heavy quark jets are excellent probes of the color field in the sQGP because their high mass changes the sensitivity of both elastic and inelastic energy loss mechanisms in a well defined way. And these changes are understood to be relative to those of light quark and gluon jets. If one or the other of jet quenching or heavy-quark suppression is present, but not both, we must be able to explain how these two observations are consistent. We believe both will be present when the plasma is produced.

- **Gluon jet fragmentation into D and B mesons can be safely neglected.**

The study of open heavy quark mesons, namely the D and B mesons, has this very important advantage over similar studies of the open light kaons and pi-mesons. Any evidence to the contrary in a measured D or B-meson spectrum will be a major complication for any interpretation. We may safely consider the heavy quark mesons as sensitive to the large difference between quark and gluon energy loss.

- **If the R_{AA} is measured and finally considered too strong in the context of our current model, we must invoke new energy loss mechanisms that have yet to be postulated.**

The two sets of theoretical predictions overlaid with the 0-10% most central R_{AA} are similar to a degree, but they represent two different approaches that not only diverge in their final results, but also in their assumptions and

p_T ranges of validity. How much we read into the final overlays and the agreement or disagreement with the data and each other depends on our understanding of each approach.

In both cases, the first task is to create code that will produce the spectrum of hadrons that carry the open charm (beauty). This means writing down an expression for the cross-section that accounts for the following:

- Initial heavy quark distributions from pQCD
- heavy flavor energy loss
- fragmentation of heavy quarks into open heavy flavor mesons.
- Open meson decays to electrons

Both calculations make the assumption of a static medium which is perhaps a misnomer. The assumption amounts to saying that the partons are moving through the medium at such a high momentum that in comparison, the medium is effectively a bunch of motionless Yukawa type scattering centers. Any possible energy loss in the form of gluon radiation, in this situation is small when compared to the total energy E of the parton.

The expression for the radiative gluon density is taken in both cases to be the sum of a vacuum density and an in-medium density. This type of situation is common in statistical field theory since in the absense of a medium, we must be left with just the vacuum contribution. The separate terms usually drop out from the calculation in a very natural way. The details of each method are laid out for the Columbia groups GLV approach in [41] and for Arnesto et. al. in [38].

These are the common points that are shared by each prediction. Differences begin to emerge as these different ingredients (factors in the meson production cross-section) are obtained and utilized in different ways. It is important to note that if these models can not explain the data, then our basic ideas of what is happening will need to be radically altered at a very fundamental level.

I say this because while the calculations are complicated and lengthy, they are generally conventional and rest upon the evaluation of Feynman diagrams for the radiative energy loss. The method in both cases for calculating the gluon radiation is to write down the diagrams corresponding to partons scattering off multiple Yukawa potentials and then radiating gluons as a result. The resulting integrals for the amplitudes are expanded in terms of a dimensionless opacity parameter that characterizes the medium and approximations are made in order to carry out the integrations. Again, the details are contained in [38] and [41] and I do not discuss them further here except to note (just to comfort the reader) that the zeroth order term in the opacity expansion corresponds to the vacuum term and has a very physical interpretation – this term describes the dead cone effect.

6.2.2 Combined Effects & Range of Validity

As stated in [38], the main concern are the multiple effects that will influence the spectra to varying degrees. Each will have a weaker or stronger impact depending on the p_T range and this in the end will have *huge* consequences for any interpretation we make.

In an attempt to untangle each individual effect and its impact of each on the R_{AA} , we may attempt to take ratios of modification factors from heavy quarks and their light counterparts. Unfortunately, this is not possible experimentally. On the other hand, it is possible to do so using theoretical models. This will be an important next step for future analyses that extend the results of this thesis. The taking of ratios of nuclear modification factors is most valuable to us as a guide to understanding the contributions of these multiple effects. I will not go deeply into the resulting ratios of modifications here but it is important to understand the phenomena at work and so each contribution is described below.

To start off, consider the parton energy loss; it has a color charge dependence. Hadrons containing light flavors will have contribution from hard fragmenting gluons. The gluons will have a stronger coupling to any medium created in the collisions and so they should lose more energy. The effect can be seen by taking ratios of modification factors; the heavy flavor R_{AA} divided by the light flavor R_{AA} . There should be an enhancement in such ratios of heavy to light nuclear modification factors for all values of p_T .

As stated many times before, charm and bottom are massive quarks and they will lose less energy in a medium than up and down quarks. This further enhances heavy-to-light ratios as long as the parton mass is not negligible compared to the partonic p_T .

We also expect to see a medium dependent trigger bias that takes two forms. The p_T spectrum of the parent parton causes this effect. Out to high p_T , the massive quark transverse momentum spectra has a lower slope than the same spectra for the light quarks. In general, the more negative the deriva-

tive of the spectrum, the more the same parton energy loss leads to a stronger reduction of the nuclear modification factor and this translates into an enhanced heavy-to-light ratio of nuclear modification factor.

The fragmentation of the parent partons will also affect the resulting R_{AA} . In particular, the fragmentation functions of heavy quarks are usually steeper than the corresponding ones for light quarks. In such a case, we should again find that the parton energy loss will lead to a suppression in the R_{AA} . As before, the ratios of heavy and light modification factors will fall to lower values.

A final examination by Arnesto et. al, of their theoretical ratios of modification factors indicate a safe range for the theoretical interpretations of their model lying between $p_T = 7$ and $p_T = 12$ GeV *for heavy quarks*. It is unknown how this range of validity translates onto the electrons which result from their decays. As stated in [38],

“For $p_T < 7$ GeV, soft hadron production or non-perturbative hadronization mechanisms in the medium like recombination or coalescence (and the possibility of thermalization and collisional energy loss) have to be considered to account for the sizable particle species dependence of the nuclear modification factors. Here, parton energy loss alone cannot be expected to provide a reliable description. This complicates the analysis of heavy meson spectra and their decay products at low p_T .”

6.2.3 Choosing Heavy Over Light Quarks

The charm are considered hard probes as already discussed in the introduction and using them, instead of pions or some other particle, to form an R_{AA} has many advantages.

Djordjevic et. al. describe clearly that heavy flavor spectra are critical for a theoretical understanding because they do not suffer from some of the light quark problems. The light quarks are considered “fragile” in the sense that light hadron modification factors are sensitive to geometrical fluctuations of the jet production points near the surface or “nuclear corona”. The heavier quarks will not be affected in the same manner and the radiative energy loss will indeed be smaller. If, in the region around 10 GeV/c in p_T , radiative energy loss really is the dominant jet quenching mechanism as they suspect, then examination of heavy open charm and bottom mesons should allow an examination of the density evolution and the opacity of the sQGP that is possibly being produced.

To be fair, there are disadvantages too. To be sure, the heavy quark decay lepton measurements are complicated because bottom decay leptons are likely, diluting the spectrum of electrons from charm for $p_T > 3$ or 4 GeV/c. The processes involved in jet quenching should further increase the contribution of bottom to our electron spectra. This will strongly influence the nuclear modification factor of electrons in the Au + Au collisions at RHIC.

6.3 General Approach – Arnesto et. al.

6.3.1 Method

Without going into great detail, I outline the procedure followed by Arnesto et. al. The first step in the general procedure used for unravelling the different effects discussed before must be to, establish what are considered the benchmark results., i.e. understand the case where the transport coefficient \hat{q} is zero. This benchmark is then taken to represent the case for which there is no energy loss. This generates the black line in Fig. 6.1.

With a benchmark in hand to use as a reference, they model the medium dependence of the energy loss. This means deciding within the model what the probability is for a quark to lose energy and what to do with a quark after it has lost all the energy it had. Such a probability must be dependent on the transport coefficient and the different choices the authors make bracketing reasonable values lead to the solid and dashed curve of Fig. 6.1. When a quark loses all its energy In their model, it gets redistributed thermally. When all this is done, the spectra are complete and the R_{AA} is formed. One can take further ratios of R_{AA} for light and heavy quarks to untangle the separate effects

6.3.2 Assumptions

The parameterization of the fragmentation functions used in the cross-section for heavy meson production is derived from the string model implemented in the general release of PYTHIA [76]. To be precise, PYTHIA is used to generate pp events containing the heavy quarks. Heavy flavor mesons that result, are

forced to decay semi-leptonically. In this fashion, they can extract the heavy quark yields and the corresponding probabilities for a quark to fragment into a hadron with a given p_T and then again into an electron with a different p_T . These are the probabilities used as the definition of fragmentation functions.

It is well known that PYTHIA does not accurately reproduce the charm cross sections without tuning so that it matches up with real data. So as is done by many groups, they tune PYTHIA. In this case, they tuned PYTHIA to reproduce the shape of STAR's experimental data for the D meson p_T distribution in the d + Au collisions measured by the STAR Collaboration.

Any parton energy loss that may be caused by the medium, will depend strongly on two things; the path length covered by the quark passing through and the density of the medium. Both path length and density will be described completely by the medium-induced gluon energy distribution, radiated off the hard parton. This distribution is a definition taken for the probability of energy loss in the cross section of heavy mesons. The transport coefficient enters at this point, since the dependence of heavy quark energy loss on density and path length depends explicitly on it. Physically, \hat{q} , denotes the average squared transverse momentum transferred from the medium to the hard parton per unit path length.

The locations of heavy mesons which are created is determined by sampling for the positions of the partons in the transverse plane of each nucleus-nucleus collision. The probability is given by the product of the nuclear thickness functions $T_A(s) T_B(b - s)$. For these thickness functions, they choose Woods-Saxon parameterizations of nuclear density profiles.

After interaction with the medium, a parton may lose all of it's energy.

Partons that lose all their energy due to medium effects are assumed to be redistributed according to a thermal distribution which depends on the temperature. For their analysis they used $T = 300$ MeV. One can also wonder if varying this temperature affects the results and the authors show that it does not. Simply varying T values between 5 and 500 MeV, proved that the final temperature of the thermal distribution only affects the nuclear modification factor for $p_T < 3$ GeV/c, safely outside the range we are interested in.

6.3.3 Interpretation

From examination of the heavy-to-light ratios, it is reasonable to conclude that the modification factors are sensitive to both the mass dependence of the parton energy loss (dead-cone effect) and the color charge dependence for two reasons.

The results are dependent on the particle species within this measurement region and that is a complication. The mass of the parton tends to control the energy loss for any $p_T < 12$ GeV/c, and thus it also controls any deviations away from unity that are present in modifications and ratios of modifications, but when there is species dependence, the application of parton energy loss becomes questionable. To be safe, as the authors make very clear, we should restrict our attention to values of quark p_T above 7 GeV/c. Though the interpretation is still murky; there will still be a large color charge dependence in the modifications.

When all is said and done, the comparison between the measurement of this thesis and the prediction of Arnesto et. al. is not all together fair. The

comparison can be made but we must be cautious. Differences between the modification factor we have measured and the theoretical prediction given by Arnesto et. al. can not be used to make any real strong statements or interpretations. The predictions for all values of \hat{q} , have *two* effects tangled up together: the mass dependence *and* the color charge dependence. Furthermore, the range of p_T where the predictions are considered valid by the authors and the range in p_T for our measurement do not overlap at all and so we can draw no real conclusions.

Of course a solid measurement of the D-meson and B-meson spectra at RHIC out to 12 GeV would be a logical next step for PHENIX. The measurement of an R_{AA} using electrons is really an indirect one and so taking ratios of heavy-to-light modification factors to make valid comparisons with theory is impossible for now.

The first most difficult challenge for any future analysis that follows our present approach will be to understand the pions above $p_T = 4.8$ GeV/c. This is the threshold momentum for a pion to emit Cherenkov radiation. With such pions, our current electron identification scheme will no longer work. The RICH subsystem will become swamped with the light from pions! Future analyses will need to deal with this in some way.

6.4 General Approach – Djordjevic et. al.

6.4.1 Method

The starting point is the same as for [38]. The cross-section for the production of heavy-flavor mesons is written down as a product of fragmentation functions, a probability of an interaction with the medium, and an electron decay spectrum; just as before.

The Columbia formalism utilizes initial p_T distributions for charm that are computed out to next-to-leading order with well known code [41]. The mass and factorization scales are tunable parameters within the model and so were chosen to agree with a previous theoretical analysis they used in [41]. The CTEQ6M parton distribution functions were used. The basis for the heavy-flavor suppression in this calculation is known as the DGLV generalization [41] of the GLV opacity expansion [41] to heavy quarks used previously.

Fragmentation functions for the formation of the D and B-mesons are extracted from e^+e^- data now rather than using a PYTHIA based model. This is complicated business that relies on previous work ?? but the important thing to note is that the fragmentation is now tuned to agree with real data and not extracted from a string model within PYTHIA. Beyond that, the leptonic decays of D and B mesons are controlled by decay spectra and branching ratios measured previously.

To my mind, choosing to use data over models is preferable and I consider it one of the strengths of this method. That is not to say, PYTHIA is not involved. The uncertainty in the model due to the choice of fragmentation and decay schemes is studied using the corresponding PYTHIA routines, assuming

Peterson fragmentation [76] with a range of parameters.

As always, the hard part in the procedure (and where the real interesting physics lies within our context) is the computation of the spectrum of gluons that are radiated away while passing through the nuclear medium. Their statement is that three effects must be calculated: the Ter-Mikayelian or massive gluon effect, transition radiation, and medium-induced energy loss. The first two effects end up canceling each other leaving only the spectrum of radiated gluons and as in the previous theoretical prediction, the expansion of the amplitudes corresponding to multiple scattering off of centers in a static medium is carried out in terms of opacity. Though in this case the calculation is based on an extension of the GLV method now extended and known as the DGLV method described in [41].

6.4.2 Interpretations

As before, the bottom is known to be an important contribution and the suppression we measure is not consistent with the prediction of the Columbia model and the author's current understanding. They go so far as to state:

"The preliminary electron data are so surprising that novel jet energy loss mechanisms may have to be postulated. The elliptic flow of high p_T heavy quarks can be accounted for, e.g., if the elastic cross sections of all partons, including bottom, are assumed to be anomalously enhanced to > 20 mb, far in excess of perturbative QCD predictions, up to at least $p_T = 10$ GeV/c. While these enhanced cross sections could lead to heavy flavor elliptic flow at the pion level even at high p_T , they may greatly overestimate the attenuation

of light and heavy flavored hadrons.”

The message to take home is that the suppression is more than they can account for and so the measured R_{AA} may be pointing towards new physics! This is very exciting and will be investigated in future runs at RHIC with PHENIX.

Chapter 7

Outlook

7.1 Preliminary Data for the Cocktail

This electron analysis was the last one to analyze RHIC Run II data. The collaboration is now focused on Run III and IV. The data set is larger and future analyses will lead to nice improvements in many of the PHENIX projects. This analysis is being repeated right now and the R_{AA} for the Run IV/III data has already achieved preliminary status in time for the Quark Matter 2005 conference being held in Budapest, Hungary. The R_{AA} is shown by centrality in Fig. 7.1.

The observed suppression is confirmed with much better precision. Expect to see much improved statistics in the Run IV data and an improved signal to background ratio. The Run IV analysis has just been declared preliminary and is shown in Fig. 7.1.

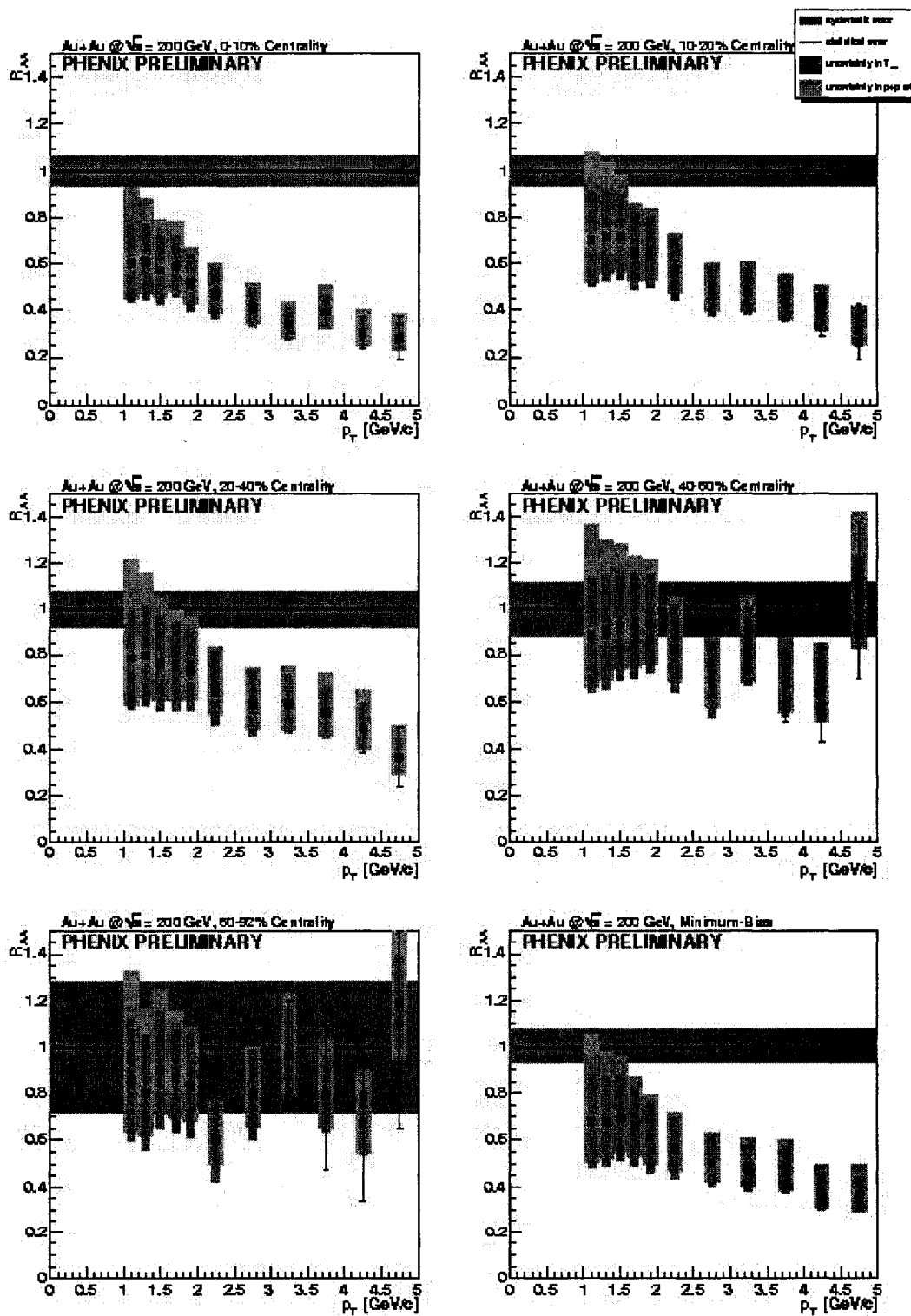


Figure 7.1: Non-photonic electron R_{AA} , by centrality class created using the Run IV Au + Au spectrum and a scaled Run III p + p spectrum.

7.2 Final Assesment

The nuclear modification factors measured in this thesis are if nothing else, fuel for our physical imaginaion. From my vantage point, as a member of a large experimental collaboration, the data says what it says and I am confident, the measurement is correct. We are consistent with previous measurements obtained by other experiments *and* PHENIX! (Recall the converter method.) As further supporting evidence, the latest data released by the STAR collaboration shown at Quark Matter '05 in Budhapest, Hungary is reproduced in Fig. 7.2.

The agreement is certainly encouraging but the plot also raises questions. Most important among them: “Where are the electrons from the bottom quark?” All present known interpretations make no distinction between charm and beauty when it comes to the modification factors. If all the same statements made in this thesis hold for beauty as well as charm, then given a bottom mass of 4.5 GeV, the modification factors should start to rise as we start to pick up electrons resulting ultimately from B-mesons and the original bottom quarks that comprise them. Where are they?

We also have two theoretical predictions that disagree. As we have just discussed at length in the previous section, each has many complications and neither one tends to lend themselves to simple interpretations. The final result is that we can not determine at this time, which of our models is correct. Possibly one, the other, or even both of them, are flawed. We are left only with puzzles and possibilities.

Only future PHENIX analysis will clarify the physics.

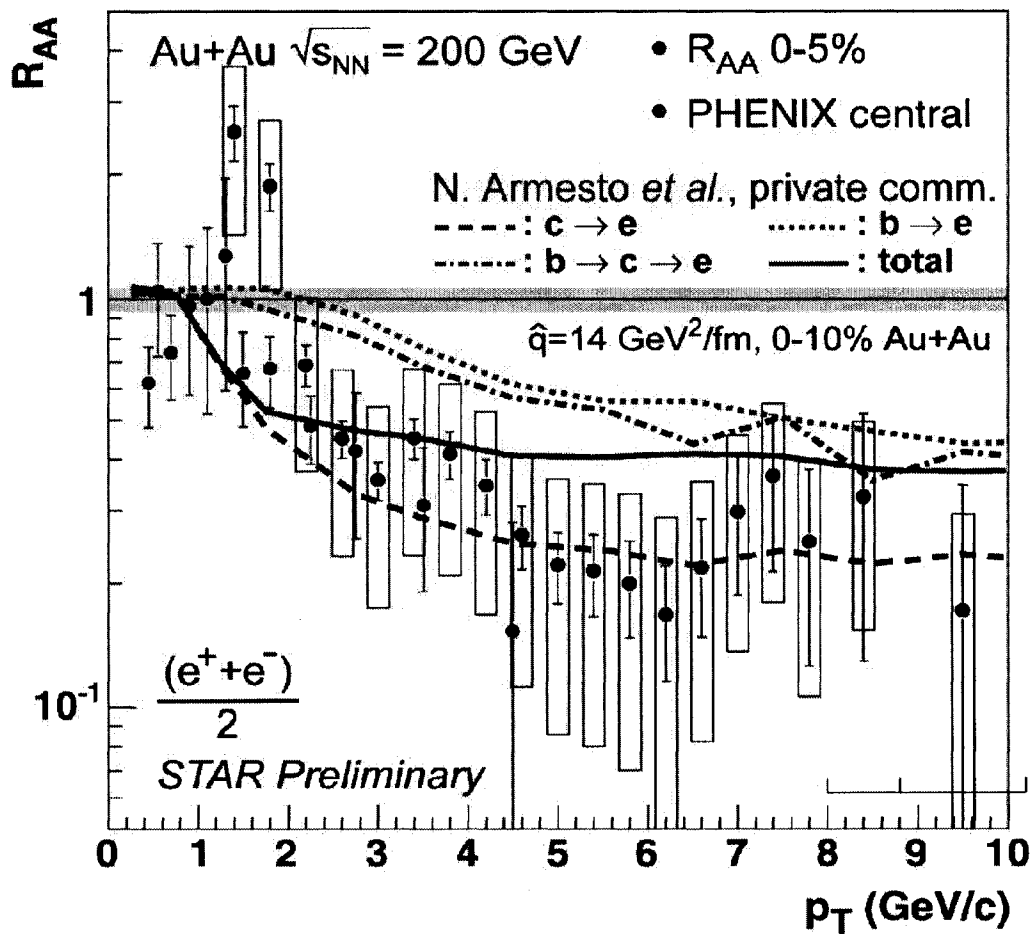


Figure 7.2: Non-photonic electron R_{AA} , by centrality class released by the STAR collaboration shown at Quark Matter '05 in Budapest.

Bibliography

- [1] Mekjian A. Z, *Phys. Rev. C* 17, 1051-1070
- [2] Hagedorn R(1965), *Nuovo Cimento*, 35, 395
- [3] Bjorken B. J. (1983), *Phys. Rev. D* 27, 140
- [4] Hanbury-Brown, R. Twiss, R. Q. (1954) *Phil. Mag.* 45, 633; (1956) *Nature* 177, 27; (1956) *Phil. Mag. Nature* 177, 27
- [5] Gyulassy, M. , Kauffmann, S. K., and Wilson, Lance W. (1979) *Phys. Rev. C* 20, 2267-2292
- [6] S.S. Adler et al, *Phys.Rev.Lett.* 91 (2003)
- [7] J. W. Cronin, H. J. Frisch, and M. J. Shochet, *Phys. Rev. D* 11, 3123 (1975)
- [8] F. Matathias, *Eftychios Felix Matathias: "Identified Particle Production in p + p and d + Au Collisions at RHIC Energies"*, Ph.D. thesis at Stony Brook University, Stony Brook, New York, December 2004
- [9] M. Lev and B. Peterson, *Z. Phys. C* 21 (1983) 155
- [10] A. Krzyqicki et all., *Phys. Lett B* 85, 407 (1979)

- [11] T. Hachiya, *PHENIX PPG035: Centrality Dependence of Charm Production from Single Electrons in Au+Au Collisions at $\sqrt{s_{NN}} = 200\text{GeV}$* , (PHENIX Experiment, 2004).
- [12] R. Averbeck, *PHENIX AN349: An electron cocktail for Au+Au collisions at $\sqrt{s_{NN}} = 200\text{GeV}$ (RunII)*, (PHENIX experiment, 2004).
- [13] S. Butsyk *Thesis, Stony Brook University, 2005*
- [14] S. Butsyk et al., *PHENIX PPG037: Open Charm Measurements from Single Electrons in p+p Collisions at $\sqrt{s} = 200\text{GeV}$* , (PHENIX Experiment, 2004).
- [15] Y. Akiba, R. Averbeck, T. Hachiya, A. Lebedev, T. Matsumoto, *PHENIX AN124: Single inclusive electrons from non-photonic sources in Au+Au collisions at $\sqrt{s_{NN}} = 200\text{GeV}$* , (PHENIX experiment, 2002).
- [16] S.S Adler et al., *PHENIX PPG014: Phys. Rev. Lett. 91, 072301 (2003)*, (PHENIX Experiment, 2004).
- [17] S. Mioduszewski: *private communication*
- [18] S. Eidelman et al., *Physics Letters B592, 1 (2004)*
- [19] Dokshitzer Y. L. and Kharzeev D. E., *Phys.Lett. B 519 199 (2001)*
- [20] Djordjevic M. and Gyulassy M., *Phys. Rev. C 68 (2003)*
- [21] Ter-Mikayelian M. L., *Dokl. Akad. Nauk SSSR 94 1033 (1954)*
- [22] J. D. Jackson, editor. *Classical Electrodynamics. John Wiley & Sons, Inc., New York, 3rd edition, 1999. ISBN 0-471-30932*

- [23] Zakharov B. G., *JETP Lett.* **76** 201 (2002)
- [24] K. Adcox et al., *Phys.Lett. B***561** (2003) 82-92
- [25] S. S. Adler et al., *Phys. Rev. C* **69**, 034910 (2004)
- [26] A. Bialas, *Nuclear Physics, A***715** (2003) 95c-97c
- [27] E. Fermi, *Prog. Theor. Phys.* **4** (1950) 570
- [28] I. Pomeranchuk, *Proc. USSR Academy of Sciences (in Russian)* **43** (1951) 889
- [29] R. Hagedorn, *Suppl. Nuovo Cimento* **2** (1965) 147
- [30] V. Koch, *Nuclear Physics A***715** (2003) 108c-117c
- [31] PHENIX collaboration *Nucl.Phys.A***757**:184-283,2005
- [32] L. McLerran *Nucl.Phys.A***699**:73-81,2002
- [33] The PHENIX collaboration *hep-ex/0507073*
- [34] The PHENIX collaboration *Phys. Rev. Lett.* **93**, 202002 (2004)
- [35] M. Harrison, T. Ludlam and S. Ozaki, *Nuclear Instruments and Methods in Physics Research Section A: Accelerators, Spectrometers, Detectors and Associated Equipment*, VOLUME 499, ISSUES 2-3, PAGES 235-880 (1 MARCH 2003) THE RELATIVISTIC HEAVY ION COLLIDER PROJECT: RHIC AND ITS DETECTORS
- [36] K. Adcox et al “Centrality Dependence of Charged Particle Multiplicity in Au-Au Collisions at $\sqrt{s_{NN}} = 130 \text{ GeV}$ ”, *PRL* **86** (2001) 3500

- [37] C. Y. Wong, “Introduction to high-energy heavy ion collisions,” SPIRES entry
- [38] Phys.Rev.D71:054027,2005 “*Testing the Color Charge and Mass Dependence of Parton Energy Loss with Heavy-To-Light Ratios at RHIC and LHC*”
- [39] A. Dainese, C. Loizides and G. Paic *Eur. Phys. J. C* 38 (2005) 461.
- [40] K. J. Eskola, H. Honkanen, C. A. Salgado and U. A. Wiedemann *Nucl. Phys. A* 747 (2005) 511.
- [41] Magdalena Djordjevic, Miklos Gyulassy (Columbia U.), Ramona Vogt (LBL, Berkeley & UC, Davis),. Jul 2005. 6pp. e-Print Archive: nucl-th/0507019 “*Influence of Bottom Quark Jet Quenching On Single Electron Tomography of Au + Au*.
- [42] K. Ikematsu et. al. *NIM A*411(98) 238-248
- [43] G. D. Lafferty and T. R. Wyatt *NIM A*355, 541 (1995)
- [44] http://www.bnl.gov/rhic/heavy_ion.htm
- [45] <http://www.bnl.gov/rhic/QGP.htm>
- [46] <http://www.astroscu.unam.mx/neutrones/home.html>
- [47] <http://www.bnl.gov/rhic>
- [48] T. J. Shea, R. L. Witkover, “*RHIC Instrumentation*” presented at the 1997 Particle Accelerator Conference,. Vancouver, BC, May 1997.

- [49] K. Adcox et al., *NIM A*499 489-507 (2003)
- [50] C. Adler et. al. *NIM A*470 (2001) 488-499
- [51] M. Aizawa et. al. *NIM A*499 (2003) 508-520
- [52] J. Jia *PHENIX Focus presentation, "How to Measure Charged Particles."*,
01/25/05
- [53] R. J. Glauber *Phys.Rev.* 130:2529-2539, (1963)
- [54] E. V. Shuryak and I. Zahed *Phys.Rev.C*70:021901,2004
- [55] E. V. Shuryak, *Nuclear Physics A*661 (1999) 119c-129c
- [56] M. Prakash and J. Lattimer, *Science, Vol 304, Issue 5670, 536-542 , 23 April 2004*
- [57] The PHENIX Collaboration *Phys. Rev. C* 71, 034908 (2005)
- [58] P. Braun-Munzinger, D. Magestro (Darmstadt, GSI), K. Redlich (Darmstadt, GSI Wroclaw U.), J. Stachel (Heidelberg U.) *Phys.Lett.B*518:41-46,2001
- [59] S. Eidelmann et al. Particle Data Group: *Phys. Lett.* **B592**, 1 (2004)
- [60] R. Averbeck, A. Drees, Y. Akiba, and T. Hachiya: *PHENIX Analysis Note AN089*
- [61] Y. Akiba, R. Averbeck, and T. Hachiya: *PHENIX Analysis Note AN101*
- [62] T. Hachiya and Y. Akiba: *PHENIX Analysis Note AN340*

- [63] S.S. Adler *et al.* PHENIX Collaboration: *Phys. Rev. Lett.* **91**, 072301 (2003)
- [64] S.S. Adler *et al.* PHENIX Collaboration: *Phys. Rev.* **C69**, 034909 (2004)
- [65] X. Li : *private communication*
- [66] H. Hiejima, J.C. Peng, M.G. Perdekamp, and A. Basilevsky: *PHENIX Analysis Note AN333*
- [67] M. Kaufmann and D. d'Enterria: *PHENIX Analysis Note AN337*
- [68] S.S. Adler *et al.* PHENIX Collaboration: *nucl-ex/0409028 accepted for publ. in Phys. Rev. Lett.*
- [69] Y. Akiba, R. Averbeck, S. Butsyk, X. Li, and G. Roche: *hep-ex/0508034*
- [70] Y.S. Tsai: *Rev. of. Mod. Phys.* **46** (1974) 815
- [71] J. Egdemir and R. Averbeck: *PHENIX Analysis Note AN351*
http://www.phenix.bnl.gov/WWW/p/draft/jamil/Electron_RAA.09.ps
- [72] N.M Kroll and W. Wada: *Phys. Rev.* **98** (1955) 1355
- [73] S.S. Adler *et al.* PHENIX Collaboration: *PPG049 paper draft*
- [74] S.S. Adler *et al.* PHENIX Collaboration: *PPG042 paper draft*
- [75] B. Jager, A. Schafer, M. Stratmann, and W. Vogelsang: *Phys. Rev.* **D67**, 054005 (2003)
- [76] <http://www.thep.lu.se/~torbjorn/Pythia.html>

Appendix A

Data Tables for Graphs

This appendix contains all the data that was presented in the main portion of the note in the form of tables for convenience and reference. As a rule, all plots were created using two sets of points; one for the systematic errors while the other was for the statistical ones. This is accurately reflected in the tables.

The first two large sets of data present in this section represent the progression of the data analysis, beginning from the initial inclusive spectra measured for each run group and ending with the final ratio or R_{AA} . The values of the data points are first listed in their own tables by centrality, followed by the associated errors contained in their own table. Each table has the same format.

Following these are the data points for the p + p reference measurement and the bin-shifted non-photonic spectra (by centrality), each in their own separate table.

DATA TABLES: point values

Minimum Bias :

p_T	QM2002	EE	Inclusive	Subtracted	Cocktail	Ratio
0.45	2.894E-01	2.787E-01	2.769E-01	2.316E-01	4.525E-02	0.498
0.55	1.463E-01	1.423E-01	1.412E-01	1.063E-01	3.485E-02	0.909
0.70	5.495E-02	5.280E-02	5.247E-02	4.043E-02	1.205E-02	0.624
0.90	1.720E-02	1.652E-02	1.641E-02	1.180E-02	4.610E-03	0.868
1.10	6.377E-03	6.148E-03	6.106E-03	3.970E-03	2.136E-03	0.978
1.30	2.600E-03	2.415E-03	2.413E-03	1.484E-03	9.289E-04	1.173
1.50	1.135E-03	1.061E-03	1.060E-03	5.952E-04	4.643E-04	0.661
1.80	3.809E-04	3.572E-04	3.566E-04	1.885E-04	1.681E-04	0.654
2.25	8.892E-05	8.363E-05	8.338E-05	3.791E-05	4.547E-05	0.497
2.75	2.151E-05	1.907E-05	1.922E-05	8.027E-06	1.119E-05	0.657
3.50	3.284E-06	3.741E-06	3.604E-06	1.401E-06	2.203E-06	0.355
4.50	4.260E-07	5.269E-07	5.020E-07	1.818E-07	3.202E-07	0.240

00 – 10% Centrality :

p_T	QM2002	EE	Inclusive	Subtracted	Cocktail	Ratio
0.45	9.768E-01	9.357E-01	9.303E-01	7.210E-01	2.094E-01	0.622

0.55	4.997E-01	4.812E-01	4.780E-01	3.292E-01	1.488E-01	1.047
0.70	1.896E-01	1.781E-01	1.777E-01	1.250E-01	5.267E-02	0.735
0.90	5.693E-02	5.622E-02	5.560E-02	3.673E-02	1.888E-02	0.957
1.10	2.124E-02	2.036E-02	2.024E-02	1.213E-02	8.110E-03	1.000
1.30	8.438E-03	8.162E-03	8.099E-03	4.355E-03	3.744E-03	1.274
1.50	3.686E-03	3.401E-03	3.401E-03	1.700E-03	1.702E-03	0.654
1.80	1.235E-03	1.150E-03	1.150E-03	5.075E-04	6.421E-04	0.673
2.25	2.756E-04	2.626E-04	2.614E-04	9.643E-05	1.649E-04	0.478
2.75	4.172E-05	4.796E-05	4.613E-05	1.968E-05	2.646E-05	0.418
3.50	1.014E-05	1.083E-05	1.057E-05	3.488E-06	7.079E-06	0.306
4.50	3.554E-06	1.015E-06	1.219E-06	4.838E-07	7.356E-07	0.148

10 – 20% Centrality :

p_T	QM2002	EE	Inclusive	Subtracted	Cocktail	Ratio
0.45	6.712E-01	6.466E-01	6.423E-01	5.020E-01	1.403E-01	0.664
0.55	3.356E-01	3.300E-01	3.266E-01	2.322E-01	9.447E-02	1.059
0.70	1.258E-01	1.230E-01	1.218E-01	8.818E-02	3.366E-02	0.749
0.90	4.031E-02	3.848E-02	3.828E-02	2.572E-02	1.256E-02	1.016
1.10	1.547E-02	1.443E-02	1.441E-02	8.727E-03	5.685E-03	1.119
1.30	6.158E-03	5.534E-03	5.561E-03	3.228E-03	2.333E-03	1.267
1.50	2.672E-03	2.465E-03	2.467E-03	1.266E-03	1.201E-03	0.736

1.80	8.689E-04	8.233E-04	8.207E-04	3.998E-04	4.209E-04	0.705
2.25	1.846E-04	2.046E-04	1.983E-04	7.860E-05	1.197E-04	0.563
2.75	6.527E-05	4.946E-05	5.117E-05	1.632E-05	3.485E-05	0.892
3.50	8.722E-06	8.590E-06	8.506E-06	2.856E-06	5.650E-06	0.394
4.50	-8.270E-08	1.293E-06	1.026E-06	3.770E-07	6.486E-07	0.214

20 – 40% *Centrality* :

p_T	QM2002	EE	Inclusive	Subtracted	Cocktail	Ratio
0.45	3.507E-01	3.346E-01	3.329E-01	2.788E-01	5.412E-02	0.518
0.55	1.779E-01	1.712E-01	1.701E-01	1.285E-01	4.158E-02	0.942
0.70	6.599E-02	6.405E-02	6.354E-02	4.844E-02	1.510E-02	0.680
0.90	2.152E-02	1.992E-02	1.992E-02	1.431E-02	5.613E-03	0.918
1.10	7.754E-03	7.604E-03	7.531E-03	4.922E-03	2.608E-03	1.037
1.30	3.201E-03	3.032E-03	3.022E-03	1.872E-03	1.150E-03	1.261
1.50	1.435E-03	1.348E-03	1.345E-03	7.714E-04	5.734E-04	0.709
1.80	4.934E-04	4.497E-04	4.507E-04	2.469E-04	2.039E-04	0.689
2.25	1.083E-04	1.043E-04	1.035E-04	5.164E-05	5.188E-05	0.492
2.75	3.259E-05	2.408E-05	2.490E-05	1.102E-05	1.389E-05	0.707
3.50	3.984E-06	4.720E-06	4.524E-06	1.916E-06	2.608E-06	0.364
4.50	3.170E-07	6.941E-07	5.668E-07	2.381E-07	3.287E-07	0.214

40 – 60% Centrality :

p_T	QM2002	EE	Inclusive	Subtracted	Cocktail	Ratio
0.45	1.176E-01	1.158E-01	1.146E-01	1.008E-01	1.381E-02	0.432
0.55	5.902E-02	5.901E-02	5.825E-02	4.625E-02	1.200E-02	0.889
0.70	2.211E-02	2.142E-02	2.126E-02	1.739E-02	3.862E-03	0.569
0.90	6.954E-03	6.651E-03	6.616E-03	5.208E-03	1.408E-03	0.754
1.10	2.554E-03	2.529E-03	2.501E-03	1.777E-03	7.237E-04	0.942
1.30	1.128E-03	9.399E-04	9.558E-04	6.819E-04	2.739E-04	0.991
1.50	4.798E-04	4.628E-04	4.598E-04	2.832E-04	1.766E-04	0.716
1.80	1.598E-04	1.568E-04	1.553E-04	9.446E-05	6.081E-05	0.675
2.25	5.261E-05	3.520E-05	3.690E-05	2.055E-05	1.635E-05	0.510
2.75	8.423E-06	9.853E-06	9.440E-06	4.519E-06	4.921E-06	0.834
3.50	1.603E-06	2.088E-06	1.955E-06	8.103E-07	1.145E-06	0.532
4.50	0.000E+00	5.093E-07	2.507E-07	1.022E-07	1.485E-07	0.326

60 – 80% Centrality :

p_T	QM2002	EE	Inclusive	Subtracted	Cocktail	Ratio
0.45	2.656E-02	2.793E-02	2.732E-02	2.511E-02	2.210E-03	0.307
0.55	1.299E-02	1.304E-02	1.286E-02	1.131E-02	1.551E-03	0.509
0.70	4.971E-03	4.791E-03	4.760E-03	4.186E-03	5.739E-04	0.371

0.90	1.303E-03	1.468E-03	1.418E-03	1.211E-03	2.070E-04	0.483
1.10	4.407E-04	5.197E-04	4.970E-04	4.162E-04	8.080E-05	0.464
1.30	1.957E-04	1.991E-04	1.960E-04	1.601E-04	3.584E-05	0.569
1.50	7.215E-05	9.076E-05	8.592E-05	6.707E-05	1.885E-05	0.338
1.80	3.324E-05	3.391E-05	3.336E-05	2.249E-05	1.087E-05	0.544
2.25	8.997E-06	7.365E-06	7.457E-06	5.064E-06	2.392E-06	0.338
2.75	1.784E-06	3.340E-06	2.859E-06	1.172E-06	1.686E-06	1.290
3.50	0.000E+00	3.613E-07	1.778E-07	2.203E-07	-4.249E-08	-0.094
4.50	0.000E+00	0.000E+00	0.000E+00	2.890E-08	-2.890E-08	-0.296

DATA TABLES: errors

MinimumBias :

p_T	QM2002	EE	Inclusive	Subtracted	Cocktail	Ratio
0.45	2.157E-03	9.853E-04	8.845E-04	7.717E-04	1.174E-03	0.115
0.55	1.193E-03	5.452E-04	4.894E-04	3.906E-04	6.261E-04	0.285
0.70	4.257E-04	1.940E-04	1.743E-04	1.211E-04	2.122E-04	0.151
0.90	1.991E-04	9.033E-05	8.119E-05	4.016E-05	9.058E-05	0.348
1.10	1.077E-04	4.904E-05	4.405E-05	1.485E-05	4.649E-05	0.472
1.30	6.343E-05	2.830E-05	2.551E-05	5.970E-06	2.620E-05	0.626

1.50	3.834E-05	1.733E-05	1.559E-05	2.539E-06	1.579E-05	0.176
1.80	1.420E-05	6.520E-06	5.848E-06	6.377E-07	5.883E-06	0.130
2.25	5.559E-06	2.469E-06	2.227E-06	1.227E-07	2.230E-06	0.090
2.75	2.363E-06	1.057E-06	9.522E-07	2.573E-08	9.526E-07	0.234
3.50	5.869E-07	2.936E-07	2.593E-07	3.476E-09	2.593E-07	0.123
4.50	2.022E-07	9.616E-08	8.573E-08	3.997E-10	8.573E-08	0.152

00 – 10% *Centrality* :

p_T	QM2002	EE	Inclusive	Subtracted	Cocktail	Ratio
0.45	1.341E-02	6.089E-03	5.473E-03	2.366E-03	5.962E-03	0.143
0.55	7.415E-03	3.355E-03	3.017E-03	1.197E-03	3.246E-03	0.329
0.70	2.621E-03	1.182E-03	1.063E-03	3.743E-04	1.127E-03	0.178
0.90	1.199E-03	5.422E-04	4.876E-04	1.271E-04	5.039E-04	0.384
1.10	6.398E-04	2.903E-04	2.609E-04	4.682E-05	2.651E-04	0.483
1.30	3.796E-04	1.682E-04	1.518E-04	1.825E-05	1.529E-04	0.681
1.50	2.291E-04	1.011E-04	9.129E-05	7.594E-06	9.160E-05	0.176
1.80	8.330E-05	3.828E-05	3.433E-05	1.785E-06	3.438E-05	0.136
2.25	3.099E-05	1.414E-05	1.270E-05	3.172E-07	1.270E-05	0.091
2.75	1.096E-05	5.492E-06	4.849E-06	6.211E-08	4.849E-06	0.164
3.50	3.357E-06	1.643E-06	1.457E-06	8.138E-09	1.457E-06	0.118
4.50	1.590E-06	4.962E-07	4.669E-07	9.699E-10	4.669E-07	0.127

10 – 20% Centrality :

p_T	QM2002	EE	Inclusive	Subtracted	Cocktail	Ratio
0.45	1.008E-02	4.594E-03	4.126E-03	1.651E-03	4.444E-03	0.153
0.55	5.565E-03	2.541E-03	2.282E-03	8.454E-04	2.433E-03	0.333
0.70	1.974E-03	9.050E-04	8.120E-04	2.641E-04	8.539E-04	0.181
0.90	9.279E-04	4.211E-04	3.785E-04	8.748E-05	3.885E-04	0.408
1.10	5.133E-04	2.294E-04	2.067E-04	3.288E-05	2.093E-04	0.541
1.30	2.966E-04	1.320E-04	1.190E-04	1.311E-05	1.197E-04	0.679
1.50	1.773E-04	8.074E-05	7.252E-05	5.426E-06	7.272E-05	0.199
1.80	6.511E-05	3.057E-05	2.732E-05	1.361E-06	2.735E-05	0.145
2.25	2.424E-05	1.176E-05	1.045E-05	2.560E-07	1.045E-05	0.109
2.75	1.214E-05	5.173E-06	4.695E-06	5.197E-08	4.696E-06	0.332
3.50	2.766E-06	1.358E-06	1.204E-06	7.000E-09	1.204E-06	0.153
4.50	9.004E-07	4.322E-07	3.847E-07	8.106E-10	3.847E-07	0.177

20 – 40% Centrality :

p_T	QM2002	EE	Inclusive	Subtracted	Cocktail	Ratio
0.45	4.665E-03	2.131E-03	1.913E-03	9.273E-04	2.126E-03	0.120
0.55	2.581E-03	1.185E-03	1.063E-03	4.712E-04	1.162E-03	0.296

0.70	9.322E-04	4.271E-04	3.833E-04	1.438E-04	4.094E-04	0.165
0.90	4.485E-04	2.019E-04	1.817E-04	4.808E-05	1.879E-04	0.369
1.10	2.421E-04	1.112E-04	9.974E-05	1.800E-05	1.014E-04	0.501
1.30	1.402E-04	6.431E-05	5.770E-05	7.406E-06	5.817E-05	0.675
1.50	8.749E-05	3.988E-05	3.582E-05	3.227E-06	3.596E-05	0.192
1.80	3.313E-05	1.466E-05	1.323E-05	8.134E-07	1.326E-05	0.142
2.25	1.306E-05	5.655E-06	5.121E-06	1.651E-07	5.124E-06	0.098
2.75	6.160E-06	2.472E-06	2.263E-06	3.570E-08	2.263E-06	0.271
3.50	1.373E-06	6.616E-07	5.884E-07	4.894E-09	5.884E-07	0.144
4.50	3.170E-07	2.198E-07	1.787E-07	5.495E-10	1.787E-07	0.169

40 – 60% Centrality :

p_T	QM2002	EE	Inclusive	Subtracted	Cocktail	Ratio
0.45	2.433E-03	1.132E-03	1.013E-03	3.439E-04	1.070E-03	0.104
0.55	1.358E-03	6.358E-04	5.684E-04	1.722E-04	5.939E-04	0.282
0.70	4.963E-04	2.272E-04	2.039E-04	5.225E-05	2.105E-04	0.140
0.90	2.351E-04	1.080E-04	9.685E-05	1.741E-05	9.840E-05	0.306
1.10	1.280E-04	5.931E-05	5.312E-05	6.421E-06	5.351E-05	0.459
1.30	7.900E-05	3.389E-05	3.073E-05	2.634E-06	3.084E-05	0.540
1.50	4.616E-05	2.157E-05	1.929E-05	1.153E-06	1.933E-05	0.204
1.80	1.749E-05	8.225E-06	7.348E-06	3.046E-07	7.354E-06	0.155

2.25	8.066E-06	3.101E-06	2.855E-06	6.401E-08	2.856E-06	0.126
2.75	2.811E-06	1.439E-06	1.265E-06	1.444E-08	1.265E-06	0.360
3.50	8.017E-07	4.344E-07	3.773E-07	2.049E-09	3.773E-07	0.246
4.50	0.000E+00	1.802E-07	8.869E-08	2.431E-10	8.869E-08	0.270

60 – 80% *Centrality* :

p_T	QM2002	EE	Inclusive	Subtracted	Cocktail	Ratio
0.45	1.103E-03	5.264E-04	4.690E-04	8.931E-05	4.774E-04	0.097
0.55	6.137E-04	2.830E-04	2.537E-04	4.382E-05	2.574E-04	0.180
0.70	2.236E-04	1.034E-04	9.267E-05	1.295E-05	9.357E-05	0.108
0.90	9.802E-05	4.888E-05	4.319E-05	4.093E-06	4.339E-05	0.218
1.10	5.063E-05	2.618E-05	2.297E-05	1.514E-06	2.302E-05	0.260
1.30	3.251E-05	1.454E-05	1.310E-05	6.141E-07	1.311E-05	0.368
1.50	1.835E-05	9.295E-06	8.188E-06	2.705E-07	8.193E-06	0.172
1.80	7.641E-06	3.622E-06	3.231E-06	7.044E-08	3.232E-06	0.193
2.25	3.618E-06	1.347E-06	1.245E-06	1.530E-08	1.245E-06	0.186
2.75	1.264E-06	8.111E-07	6.751E-07	3.624E-09	6.751E-07	0.683
3.50	0.000E+00	1.621E-07	7.977E-08	5.435E-10	7.977E-08	-0.179
4.50	0.000E+00	0.000E+00	0.000E+00	6.790E-11	6.790E-11	-0.170

Table A.2: p + p Reference Spectrum

p_T	Invariant Cross-Section	σ_{stat}	σ_{sys}
0.45	0.0145311	0.00332241	0.0114039
0.55	0.00614202	0.00192325	0.00500628
0.7	0.00298603	0.000718324	0.00182898
0.9	0.000834114	0.000333968	0.000533937
1.1	0.000344139	0.000165882	0.000189519
1.3	0.000125097	6.67069e-05	7.21075e-05
1.5	0.000111905	2.95235e-05	3.73533e-05
1.8	3.87463e-05	7.5549e-06	1.23003e-05
2.25	1.37108e-05	2.37976e-06	3.42818e-06
2.75	2.58058e-06	8.94809e-07	7.13291e-07
3.5	8.40114e-07	2.73218e-07	1.77853e-07
4.5	1.89466e-07	1.08795e-07	3.53558e-08

Table A.3: Bin-shifted Non-Photonic Minimum Bias Spectrum

p_T	Invariant Multiplicity	σ_{stat}	σ_{sys}
0.45	0.0444554	0.00115322	0.0564365
0.55	0.0342759	0.000615778	0.0277879
0.7	0.0114459	0.000201617	0.0100541
0.9	0.00444378	8.73041e-05	0.00312181
1.1	0.00206581	4.49539e-05	0.00113304
1.3	0.00090079	2.5402e-05	0.000442899
1.5	0.000454508	1.54611e-05	0.000192378
1.8	0.000155673	5.4476e-06	6.05171e-05
2.25	4.18319e-05	2.05137e-06	1.37108e-05
2.75	1.04058e-05	8.85668e-07	3.15777e-06
3.5	1.83157e-06	2.15594e-07	5.25123e-07
4.5	2.79773e-07	7.49115e-08	7.62961e-08

Table A.4: Bin-Shifted Non-Photonic Statistical Spectrum 00-10% Centrality

P_t	Inv. Mult.	σ_{stat}	σ_{sys}
0.45	0.205546	0.0058526	0.185388
0.55	0.146235	0.00318991	0.0920094
0.7	0.0499387	0.00106855	0.0331901
0.9	0.0181673	0.000484905	0.0103639
1.1	0.00783214	0.000255974	0.00369667
1.3	0.00362627	0.000148053	0.00145059
1.5	0.00166453	8.95937e-05	0.000607228
1.8	0.000592801	3.17413e-05	0.000190096
2.25	0.000149063	1.14781e-05	4.14294e-05
2.75	2.45347e-05	4.49677e-06	7.62743e-06
3.5	5.84749e-06	1.20326e-06	1.51552e-06
4.5	6.39814e-07	4.06122e-07	1.87464e-07

Table A.5: Bin-Shifted Non-Photonic Spectrum 10 - 20 % Centrality

P_t	Inv. Mult.	σ_{stat}	σ_{sys}
0.45	0.137649	0.00436122	0.131485
0.55	0.0928235	0.00239071	0.0650925
0.7	0.031915	0.000809588	0.0235482
0.9	0.0120915	0.000374018	0.00736406
1.1	0.0054941	0.000202244	0.00271571
1.3	0.00226158	0.000116071	0.00104186
1.5	0.0011756	7.11817e-05	0.000456229
1.8	0.000389808	2.53345e-05	0.000142431
2.25	0.000110241	9.6219e-06	3.33272e-05
2.75	3.28408e-05	4.42487e-06	8.63289e-06
3.5	4.72278e-06	1.00636e-06	1.27804e-06
4.5	5.79016e-07	3.43372e-07	1.65841e-07

Table A.6: Non-photonic Spectrum 20 - 40 % Centrality

P_t	Inv. Mult.	σ_{stat}	σ_{sys}
0.45	0.0531837	0.00208944	0.0653908
0.55	0.0408955	0.00114344	0.0321896
0.7	0.0143546	0.000389106	0.0116564
0.9	0.00541103	0.000181163	0.00363161
1.1	0.00252238	9.80111e-05	0.00133843
1.3	0.00111483	5.64018e-05	0.000530609
1.5	0.00056126	3.52004e-05	0.000233875
1.8	0.000188658	1.22686e-05	7.33358e-05
2.25	4.7669e-05	4.70834e-06	1.64116e-05
2.75	1.28961e-05	2.10203e-06	3.90913e-06
3.5	2.161e-06	4.8749e-07	6.29453e-07
4.5	2.86367e-07	1.55699e-07	8.28291e-08

Table A.7: Non-photonic Spectrum 40 - 60 % Centrality

P_t	Inv. Mult.	σ_{stat}	σ_{sys}
0.45	0.01355588	0.00105045	0.0230523
0.55	0.0117967	0.000583942	0.0112755
0.7	0.00366887	0.000199981	0.00402077
0.9	0.00135784	9.48811e-05	0.00125204
1.1	0.00070036	5.1782e-05	0.000458776
1.3	0.000267865	3.01606e-05	0.000177408
1.5	0.000172962	1.89327e-05	8.19682e-05
1.8	5.65087e-05	6.83347e-06	2.61712e-05
2.25	1.51109e-05	2.63937e-06	6.05796e-06
2.75	4.64922e-06	1.19529e-06	1.53799e-06
3.5	9.64618e-07	3.17932e-07	2.7784e-07
4.5	1.33228e-07	7.95793e-08	3.78472e-08

Table A.8: Non-photonic Spectrum 60 - 80 % Centrality

P_t	Inv. Mult.	σ_{stat}	σ_{sys}
0.45	0.00218593	0.000472141	0.00556362
0.55	0.00153275	0.000254392	0.00256667
0.7	0.000542452	8.84431e-05	0.000908482
0.9	0.000197218	4.13358e-05	0.000269378
1.1	7.81946e-05	2.22749e-05	9.51692e-05
1.3	3.48502e-05	1.27487e-05	3.73389e-05
1.5	1.85098e-05	8.04373e-06	1.62453e-05
1.8	1.03263e-05	3.07061e-06	5.80937e-06
2.25	2.27259e-06	1.18304e-06	1.30154e-06
2.75	1.63086e-06	6.52872e-07	4.55652e-07
3.5	-3.87253e-08	7.27123e-08	3.90099e-08
4.5	-2.74598e-08	6.45085e-11	4.11897e-09

Appendix B

Parametrizations

B.1 depemc

The parameterization used for depemc(ecore, mom, sector) was determined by Y. Akiba and T. Hachiya for use in Run II data. I quote it here as a function since this is easiest and most the most accurate description possible.

```
float dep_emc(float energy, float p, int LG) {  
  
    float sig_e;  
    float ret_val;  
  
    if(LG==0) { // Lead Scintillator  
  
        sig_e = sqrt(8.5e-3 + 4.5e-3/p);  
        if ( sig_e < 0.10 ) sig_e=0.10;  
        ret_val = ((energy - p + 0.025)/p)/sig_e;  
    }  
}
```

```
    } else { // lead glass

        float dE;

        if      ( p < 0.3 ) dE=0.07;
        else if ( p < 0.4 ) dE=0.08;
        else if ( p < 0.6 ) dE=0.085;
        else                  dE=0.09;

        sig_e = sqrt(5.1e-3+6.6e-3/p);
        if ( sig_e < 0.10 ) sig_e = 0.10;
        ret_val = ( (energy - p + dE) / p ) / sig_e;
    }

    return ret_val;
}
```

Appendix C

Index

Index

- N_{coll} , 13
 V_2 , 12
 J/Ψ , 25, 26
x J/Ψ , 25
AGS, 25
astrophysics, 6
baryon chemical potential, 8
BEVALAC, 5, 28
Big Bang, 11
big bang, 10, 12
Big-Bang Nucleosynthesis, 10
binary scaling, 13
Boltzmann equation, 19
bound state, 22, 25, 26, 28, 30
bound states, 19
Bremsstrahlung, 16
Bulk properties, 19
bulk properties, 9, 16
canonical, 12
centrality, 10
Charm, 25
charm, 17, 24–26, 30, 64, 111, 157,
184
charm production, 14
charm production, 13, 28, 65
charm quark, 15, 16
charm quarks, 17
critical temperature, 10, 12
cross-sections, 25
CSC, 6, 8
D-mesons, 28
dead cone prediction, 16
deuteron, 21
diffusion models, 19
direct photons, 12
down, 16, 17
Drell-Yan, 26
Drell-Yan process, 25
electron-positron collisions, 24

elliptical flow, 12
energy density, 12, 21
Energy loss, 16
energy loss, 16, 17, 19, 23, 28, 55,
64, 158
Energy Loss Mechanisms, 16
energy-density, 21
energy-loss, 17
Equation of State, 5
equation of state, 28
equilibrium, 23
factorizations scales, 15
Fermi, 23
Feynman diagrams, 14
final state, 12, 23
fireball, 9, 10, 12, 19
first order transitions, 8
freeze-out, 10, 12
freezeout, 10
gluon distribution functions, 15
gluon emission, 18
gluon fusion, 13, 15
gluon radiation, 16, 17
grand canonical, 12
grand-canonical ensemble, 24
hadron phase, 12
hadronic matter, 6
Hadronization, 9
Hagedorn, 9
Hagedorn Resonance Gases, 23
hard probe, 12
hard probes, 12
hard process, 26
hard scattering, 12
heavy flavor, 12
heavy-flavor, 12
heavy-flavor decays, 12
impact parameter, 10
initial state effects, 12
jet correlations, 12
Jets, 12
jets, 12, 22
Leading order, 15
liquid-gas transition, 8
mass of the charm quark, 15
masses of the quarks, 15

medium, 16, 17, 19–24, 26, 58, 64, 158, 159
multi-fragmentation, 8
Multiplicity, 13
multiplicity, 13, 26, 41, 95, 98, 133, 135, 137, 161
Neutron stars, 6
neutron stars, 6
next-to-leading order, 15
nuclear medium, 12
nucleon, 10
open charm, 19, 20, 26, 28, 37
participant, 10
particle ratios, 24
particle yields, 23, 24
parton distribution functions, 15
phase diagram, 5, 6, 8, 28, 29
phase structure, 9
phase transition, 6
PHENIX, 13, 21, 22, 26, 31, 32, 35, 37–41, 43, 45, 46, 48, 50–53, 60, 66, 67, 73, 80, 82, 95, 98, 111, 113, 126, 130–132, 135, 161, 182, 184
pion, 22, 53, 78, 114–128, 130, 134–137, 142, 163, 164
Pions, 53
plasma frequency, 17
polarization, 17
Pomeranchuk, 23
predict ratios, 24
probes; hard and soft, 12
production, 27
pseudo-rapidity, 27
QCD, 5, 6, 8, 9, 13, 15, 18, 26, 28, 29
QGP, 6, 9, 23, 28, 30
Quark Matter, 23
quark matter, 6
quark-antiquark annihilation, 13
quark-gluon plasma, 6, 21, 28, 29
radial flow, 28
radiation, 13, 17, 19
radiative corrections, 14
renormalization, 6
renormalization scale, 15
RHIC, 4, 9, 10, 16, 19–23, 26–28, 30–37, 43, 44, 49, 66, 158,

semi-leptonic decays, 28
single electrons, 26
single-electron, 15, 26
single-electrons, 15, 28, 95
SIS, 25, 31
Soft probes, 12
Species, 20
spectator, 10
SPS, 25
Statistical models, 24
statistical models, 23, 24
strange stars, 6
strong force, 17
strong interaction, 16, 21

Ter-Mikayelian effect, 17
thermalization, 28
transition radiation, 19
transport coefficient, 17, 19

up, 16, 17